

**GPS BASED ATTITUDE DETERMINATION  
FOR SPINNING SATELLITES  
Final Technical Report**

to the Office of Naval Research

ONR Scientific Officer -

Douglas E. Lake

Principal Investigator -

Penina Axelrad

Report Written By -

Penina Axelrad

Charles P. Behre

Colorado Center for Astrodynamics Research

University of Colorado, CB 431

Boulder, CO 80309

December 10, 1997

Grant Number: N00014-94-1-1158

CCAR Report Number: PA-97-060

19980102 013

DTIC QUALITY INSPECTED 4

**DISTRIBUTION STATEMENT A**

Approved for public release;  
Distribution Unlimited

**GPS BASED ATTITUDE DETERMINATION  
FOR SPINNING SATELLITES  
Final Technical Report**

to the Office of Naval Research

ONR Scientific Officer - Douglas E. Lake

Principal Investigator - Penina Axelrad

Report Written By - Penina Axelrad  
Charles P. Behre

Colorado Center for Astrodynamics Research  
University of Colorado, CB 431  
Boulder, CO 80309

December 10, 1997

Grant Number: N00014-94-1-1158

CCAR Report Number: PA-97-060

## **Abstract**

This report describes the research performed by the Colorado Center for Astrodynamics Research (CCAR) under an AASERT Grant to study Global Positioning System based attitude determination for spinning satellites. Two key contributions are discussed - phase-based methods for estimation of the spin axis of a spinning satellite, and signal-to-noise ratio (SNR) based methods for estimation of one or more spacecraft axes. The latter method, which is very robust and widely applicable, is demonstrated on actual flight data from three NASA missions. It provides instantaneous pointing knowledge at the 3-10 deg level with a single GPS antenna and is useful for attitude initialization, verification, GPS phase ambiguity resolution, and a reliable backup attitude determination sensor.

## CONTENTS

### CHAPTER

1	INTRODUCTION .....	1
1.1	Research Motivation .....	1
1.2	Low-Cost Satellite Attitude Determination .....	2
1.3	Previous Work .....	3
1.4	Research Contribution .....	6
1.5	Research Overview .....	7
2	GPS BASED ATTITUDE BACKGROUND .....	9
2.1	Introduction .....	9
2.2	Phase Difference Measurements .....	9
2.3	Baseline Estimation from $\Delta\phi$ Measurements .....	12
2.4	Displacement Vector Estimation from $\delta\Delta\phi$ Measurements .....	14
2.5	Attitude Estimation from Vector Observations .....	16
2.6	Attitude Estimation from Phase Measurements .....	18
2.7	Single-Axis Attitude .....	20
2.8	Conclusions .....	21
3	GPS PHASE-BASED SPIN AXIS ESTIMATION .....	23
3.1	Introduction .....	23



3.2	Spinning Satellite Model. ....	24
3.2.1	Antenna Motion ....	26
3.2.2	Computer Simulation. ....	28
3.3	Ground Experiment. ....	28
3.3.1	Experimental Apparatus ....	28
3.3.2	Experimental Motion ....	30
3.3.3	Experimental Motion Frequencies ....	34
3.3.4	GPS Receiver ....	34
3.4	Frequency Estimation Techniques. ....	35
3.4.1	Displacement Vector Magnitude Algorithm ...	35
3.4.2	FFT Algorithm ....	36
3.4.3	AR Algorithm ....	37
3.4.4	Frequency Estimation Results. ....	39
3.5	Attitude Estimation Techniques ....	40
3.5.1	Cross Product Algorithm ....	41
3.5.2	Spinning Satellite Batch Processor. ....	41
3.5.3	Ground Experiment Batch Processor ....	43
3.5.4	Estimation Results. ....	44
3.6	Conclusions ....	45
4	SNR AND OFF-BORESIGHT ANGLE RELATIONSHIP...	47
4.1	Introduction. ....	47
4.2	SNR Measurements ....	48
4.3	Receiver Antenna Gain Pattern ....	48

4.4	Space Loss .....	51
4.5	Transmitting Power Gain Pattern Correction.....	54
4.6	Multipath Effects .....	57
4.7	Variations Due to Individual GPS Satellites.....	60
4.8	SNR to $\alpha$ Mapping Function.....	61
4.8.1	Calibration Based Mapping Function.....	61
4.8.2	Gain Pattern Based Mapping Function .....	65
4.8.3	Mapping Function Summary.....	68
4.9	Estimation of the Boresight Alignment .....	68
4.10	Conclusions .....	73
5	MAXIMUM LIKELIHOOD BASED ESTIMATION ALGORITHMS.....	75
5.1	Introduction.....	75
5.2	Estimation Geometry .....	76
5.3	Maximum Likelihood Estimates .....	81
5.4	Shuster's Method.....	82
5.4.1	Estimation Procedure.....	82
5.4.2	The Shuster Algorithm Applied to SNR Measure- ments.....	86
5.4.3	Estimation Error Covariance.....	87
5.5	Spinning Satellite SNR-Based Attitude Determination	88
5.5.1	Boresight Mounted Parallel to the Angular Momentum Axis .....	88
5.5.2	Boresight Mounted Perpendicular to Angular Mo- mentum Axis.....	90

	5.5.3 Boresight Mounted Acutely to the Angular Momentum Axis.....	92
	5.6 Three-Axis SNR-Based Attitude Determination.....	93
	5.7 Conclusions .....	95
6	SNR TEST DATA.....	97
	6.1 Introduction.....	97
	6.2 TANS Vector Receiver.....	97
	6.3 NovAtel 12 Channel Receiver.....	98
	6.4 GANE.....	99
	6.5 CRISTA-SPAS.....	100
	6.6 GPS/MET.....	101
	6.7 Ground TANS .....	103
	6.8 NovAtel Ground.....	104
	6.9 $\alpha$ vs. SNR for the Data Sets .....	105
	6.10 Normal Distribution Assumption.....	109
	6.10.1 Test Statistic.....	109
	6.11 Conclusions .....	114
7	SNR BASED SINGLE-AXIS ESTIMATION: MLE RESULTS.....	115
	7.1 Introduction.....	115
	7.2 Reference Results .....	116
	7.3 Results for Specific Mapping Function Sources ....	124
	7.4 CRISTA-SPAS Results using Individual Satellite Mapping Functions .....	127
	7.5 Performance Factors .....	127

7.6	Estimation Performance vs. Computed Error Bounds .....	132
7.7	Conclusions .....	136
8	SUMMARY.....	139
	BIBLIOGRAPHY .....	143



## FIGURES

### FIGURE

2.1	Relationship between an antenna phase difference and a baseline vector. ....	11
2.2	The displacement vector. ....	15
2.3	Relationship between antenna baselines and reference frames. ....	19
2.4	Single-axis attitude. ....	20
3.1	Kinematic model. ....	25
3.2	Equipment diagram. ....	29
3.3	Experimental setup. ....	30
3.4	Spinning and tipping motion. ....	33
3.5	Angular displacement. ....	36
3.6	The pole - frequency relationship for a noisy sampled signal. ....	39
4.1	GANE choke ring antenna gain pattern. (data from Susan F. Gomez at NASA JSC) ....	49
4.2	TANS patch antenna gain pattern. (data from R. Allshouse at Allied Signal Technical Services Corporation) ....	49
4.3	GPS/MET antenna gain pattern. (data from Charles Dunn at NASA JPL) ....	50
4.4	Ashtech choke ring antenna gain pattern. (data from UNAVCO) ....	50
4.5	SNR and Boresight Relationship. ....	51

4.6	Space Loss Effects on SNR. ....	54
4.7	GPS satellite antenna gain pattern. [Czopek and Shollenberger, 1993] ....	55
4.8	Angle in transmitting antenna pattern. ....	56
4.9	Example of SNR adjustments. ....	58
4.10	SNR adjustments vs. the angle between satellites. ....	58
4.11	The effect of multipath on SNR. ....	59
4.12	$\alpha$ versus SNR for PRN# 1. ....	62
4.13	$\alpha$ versus SNR for PRN# 6. ....	62
4.14	$\alpha$ versus SNR for PRN# 21. ....	63
4.15	$\alpha$ versus SNR for PRN# 26. ....	63
4.16	Scaling of measured gain pattern values to receiver output values. ....	66
4.17	Boresight alignment. ....	69
5.1	Single axis estimation from two angle measurements. ...	76
5.2	Estimation geometry. ....	78
5.3	Boresight Information from a Single GPS Satellite. ....	79
5.4	Multiple SNR and LOS vector geometry. ....	79
5.5	Geometry of GPS measurements. ....	80
5.6	Boresight angles. ....	84
5.7	Parallel mounting. ....	89
5.8	Perpendicular mounting. ....	91
5.9	Acute angle mounting. ....	93
5.10	Three axis estimation. ....	94

6.1	The Trimble TANS Vector. ....	98
6.2	The 12 Channel NovAtel. ....	99
6.3	The GANE experiment. [GANE Home Page] ....	100
6.4	The CRISTA-SPAS Satellite. [JSC Digital Image Collection Home] ....	102
6.5	Diagram of the GPS/MET satellite [GPS/Met Home Page]. ....	103
6.6	Ground experiment setup. ....	104
6.7	GANE $\alpha$ vs. SNR. ....	106
6.8	CRISTA-SPAS $\alpha$ vs. SNR. ....	106
6.9	GPS/MET $\alpha$ vs. SNR. ....	107
6.10	Ground TANS $\alpha$ vs. SNR. ....	107
6.11	NovAtel $\alpha$ vs. SNR (NovAtel antenna). ....	108
6.12	NovAtel $\alpha$ vs. SNR (choke ring antenna). ....	108
6.13	NovAtel $\alpha$ vs. SNR (TANS antenna). ....	109
6.14	Distribution test for GANE #1. ....	111
6.15	Distribution test for CRISTA-SPAS. ....	112
6.16	Distribution test for GPS/MET. ....	112
6.17	Distribution test for Ground TANS. ....	113
6.18	Distribution test for NovAtel #1. ....	113
7.1	GANE mapping function. ....	117
7.2	CRISTA-SPAS mapping function. ....	117
7.3	GPS/MET mapping function. ....	118
7.4	NovAtel mapping function (NovAtel antenna). ....	118



7.5	NovAtel mapping function (Ashtech antenna). . . . .	119
7.6	Ground TANS mapping function. . . . .	119
7.7	GANE #1 estimation error history. . . . .	121
7.8	CRISTA-SPAS estimation error history. . . . .	121
7.9	GPS/MET #1 estimation error history. . . . .	122
7.10	NovAtel #1 estimation error history. . . . .	122
7.11	GANE #1 and #2 PDOP dependence. . . . .	133
7.12	CRISTA-SPAS #1 and #2 PDOP dependence. . . . .	133
7.13	GPS/MET #1 and #3 PDOP dependence. . . . .	134
7.14	NovAtel #1 and #4 PDOP dependence. . . . .	134
7.15	SNR bin resolution dependence for GANE and CRISTA- SPAS #1. . . . .	135
7.16	SNR bin resolution dependence for NovAtel #1 and #2. . .	135

## TABLES

### TABLE

3.1	Performance of frequency methods on simulated data.....	40
3.2	Performance of frequency methods on experimental data. ....	40
3.3	Performance of attitude methods on simulated data. ....	45
3.4	Performance of attitude methods on experimental data. ....	45
6.1	$\tau$ for some standard distributions. [Hoaglin, et al., 1983] ...	110
7.1	Boresight Alignment.....	120
7.2	Estimation Results with Reference. ....	123
7.3	Estimation Results with Reference using . ....	125
7.4	Estimation Results with Various Mapping Functions. ....	126
7.5	Estimation Results with Individual Mapping Functions....	128
7.6	Quality of Data. ....	129
7.7	Visibility Dependence for GANE #1 and #2.....	130
7.8	Visibility Dependence for CRISTA-SPAS #1 .....	130
7.9	Visibility Dependence for GPS/MET #1 .....	131
7.10	Visibility Dependence for NovAtel #1.....	131
7.11	Comparison of Actual Errors to Predicted Errors .....	136



## CHAPTER 1

### INTRODUCTION

This report describes the research performed by the Colorado Center for Astrodynamics Research (CCAR) under an AASERT Grant to study Global Positioning System based attitude determination for spinning satellites. This research augments a series of parent grants from the Naval Research Laboratory on GPS-based attitude estimation. The subsequent chapters of this report are extracted from the doctoral dissertation of Charles Behre submitted to the Graduate School of the University of Colorado, Boulder, in December 1997, entitled "GPS Based Attitude Algorithms for Low Cost Satellite Missions."

#### **1.1 Research Motivation**

The original goal of this research was to develop algorithms for using GPS onboard spin stabilized satellites ranging from low-cost student projects such as the Student Nitric Oxide Explorer (SNOE) to highly maneuverable, advanced Navy satellites such as Living Plume Shield (LIPS) III. In the process of investigating traditional phase-based techniques we came across suggestions for the use of an alternate GPS observable, the signal-to-noise ratio for attitude estimation. Our research has fully developed this type of approach which has very broad applicability to

not only spacecraft attitude determination but for land vehicle orientation as well.

## **1.2 Satellite Attitude Determination**

The GPS system consists of a constellation of 24 Earth orbiting satellites that transmit ranging signals and a ground control facility. Reception of the signals provides a variety of information. Typically, receivers track quantities such as the ranges to the satellites in view, the carrier phases of the signals, and the signal-to-noise ratios (SNR) of the measurements. While GPS is most recognized as a tool for position estimation, it is also widely used for attitude estimation.

Many types of instruments are used for satellite attitude determination. They include star sensors, sun sensors, Earth horizon sensors, gyros, magnetometers, and GPS receivers. To minimize cost, the choice of attitude sensor has to be well matched with the mission requirements. Choosing a sensor with a much higher level of performance than is required wastes resources. Star sensors have accuracies of better than 0.1 deg, but they are heavier, more expensive, and require more power than other attitude sensors [Wertz, 1978]. For accuracies of under 1 deg, companies such as Ithaco and Barnes produce fine sun sensors and Earth horizon sensors. These instruments are priced in the range of fifty to over a hundred thousand dollars. Coarse magnetometers provide accuracies of approximately 3 to 10 degrees. The prices range from ten to twenty thousand dollars depending upon the desired accuracy and the number of axis to be sensed. Coarse sun sensors are usually the cheapest of the instruments. When

bought commercially, they cost about five thousand dollars, however, they must be used in conjunction with another sensor [Wertz and Larson, 1991].

Several student-built satellites, that have yet to be launch, utilize various combinations of lower cost instruments to provide attitude estimation of about 5 degrees. The spin stabilized SNOE satellite, built at the University of Colorado, uses two horizon crossing indicators and a three-axis magnetometer [Barth et al., 1994]. The three-axis stabilized CATSAT from the University of New Hampshire has a fiber optic gyro (FOG), a three-axis magnetometer, and a GPS receiver [CATSAT Home Page]. The gravity gradient stabilized ASUSAT satellite from the Arizona State University uses an array of student built Earth and Sun sensors [ASUSAT 1]. This last satellite is of particular interest to this research because it also has a GPS receiver on-board for navigation information.

### 1.3 Previous Work

The most common form of GPS-based attitude estimation involves the utilization of specially designed receivers that use carrier phase interferometry between several GPS antennas. Performance of 1 deg or better has been shown using GPS attitude receivers such as the Trimble Vector [Cohen, 1992], [Trimble, 1993] and the Ashtech 3DF [Lu, et al., 1993], as well a system of separate receiver modules [Lu, et al., 1993], [Cannon, et al., 1994].

The use of GPS for spacecraft attitude determination onboard an Earth-pointing spacecraft already has been demonstrated on the U.S. Air Force RADCAL (Radar Calibration) satellite [Lightsey et al., 1994], [Ward and Axelrad, 1995], on the Crista Spas mission [Ward, L.M., 1996], [Brock

et al., 1995], on the REXII satellite [Lightsey et al., 1996], and on the space shuttle GANE (GPS Attitude and Navigation Experiment) mission [Carpenter and Hain, 1997]. Each of these missions use a Trimble TANS Vector receiver. The Vector is capable of tracking up to six GPS satellites on four antennas and measuring carrier phase differences.

Martin-Niera and Lucas of the European Space Agency were the first to suggest the adaptation of GPS phase measurements specifically to spinning satellites [Martin-Niera and Lucas, 1992]. They describe a fast Fourier transform (FFT) based method for using a single GPS antenna baseline to determine spacecraft spin and nutation rates as well as nutation angles and orientation of the angular momentum vector. Their approach uses triple-differenced phase measurements as the basic observable. Their experimental results are based on data collected by a ground GPS receiver mounted on a spinning platform. The spin frequencies chosen for the simulation minimize the sampling errors inherent in the FFT technique.

The receivers that are able to measure differential phase tend to be more expensive than single antenna navigation receivers. However, attitude estimation from a single antenna is also possible by exploiting another measured quantity. The SNR measurement, that is commonly computed by all GPS receivers as they track incoming signals, is also dependent upon vehicle attitude. Due to the variations in the GPS antenna gain pattern, the SNR values are related to the orientation of the antenna with respect to the GPS satellites which are transmitting the particular signals being received. In this research, the nature of these variations is exploited to estimate the boresight of the antenna.

Single axis estimation using GPS SNR data was first suggested in a Motorola patent [Ghaem et al., 1992]. The inventors propose combining a directional antenna with a hemispherical antenna in a GPS receiver to determine heading. The GPS receiver indicates the direction to at least one GPS satellite. The directional antenna is then rotated until it receives a signal from the chosen satellite. The combination of the orientation of the directional antenna and the known coordinates of the GPS satellite establish a reference heading. The user's heading is computed from the angle between the directional antenna and the travel direction. No performance estimates are given in the patent.

In another patent, Flawn suggests using a multi-element antenna in conjunction with a GPS receiver [Flawn, 1996]. From a common GPS satellite, the various antenna elements have a different reception of the incoming signal. This difference is then utilized to determine the orientation of the antenna with respect to the GPS satellite and as a result, the users heading.

A proposal for using SNR measurements from a standard antenna for spacecraft attitude determination is made by Hashida and Unwin of the University of Surrey. They suggest using the SNR measurement from one antenna for directional information [Hashida and Unwin, 1993]. These readings compose one set of the observations in a Kalman filter. The filter estimates position and velocity from GPS data as well as attitude from the SNR data of a single antenna. Their approach is to model both the azimuth and elevation pattern of an antenna from ground data and then to apply this model in the filter. Accuracies of 3 deg in roll and pitch and 10 deg in yaw are shown only on simulated data.



Another European group uses the SNR readings from two canted antennas to estimate the body frame coordinates of the line-of-sight (LOS) vectors from the GPS antenna to the GPS satellites [Serrano, et al., 1995]. The relationship between the SNR and the boresight vector of the antenna is modeled in detail. Their results are demonstrated entirely with simulated data and depended greatly on the degree of SNR mismodeling.

Researchers at the Jet Propulsion Laboratory use the SNR measurements as weights in a LOS averaging method for coarse attitude estimation [Dunn, 1997]. They estimate the boresight vector of a GPS antenna by averaging all of the LOS vectors to the visible GPS satellites. The LOS vectors are weighted such that the ones corresponding to the largest SNR's are assigned the highest weights. The estimate is used on the GPS/MET satellite for the purpose of satellite acquisition.

#### **1.4 Research Contribution**

This research extends the work on GPS based attitude determination in two key areas. The first is the use of GPS phase data for spinning satellites. The second is a very robust and widely applicable technique based on SNR measurements made from a single antenna. The former algorithms are demonstrated for simulated data and a ground experiment conducted with the assistance of the Naval Research Laboratory. The latter algorithms are demonstrated using actual flight data from three NASA satellite missions as well as ground test data.

The phase-based approach includes several algorithms. For finding the angular rates, a simple averaging technique, FFT technique, and an auto-regressive (AR) method are studied. For determining the orientation

of the angular momentum vector, an averaging method and a batch filter are analyzed. Results are shown on a computer simulation of GPS phase measurements collected on a spinning satellite and on data collected from a ground test. The computer simulation models a perfectly symmetrical spinning satellite with two GPS antennas mounted along a diameter of the face. The ground experiment consists of a tipping and spinning platform that approximates the kinematics of a spinning satellite. Data is taken from a Trimble TANS Vector receiver.

The SNR-based approach uses a maximum likelihood estimation (MLE) of an antenna boresight vector given a set of estimated off-boresight angles. Results are shown on a variety of data sets. These sets include space based data and ground based data with different GPS receivers and antennas. Extension of the single axis based estimation to both spinning and three-axis stabilized satellites is also examined.

## 1.5 Research Overview

The second chapter of this report presents a background of GPS phase based measurements and their relationship to attitude. This is followed by a detailed description of the use of carrier phase measurements applied specifically to spinning satellites.

The remaining chapters deal specifically with the SNR-based estimation. Chapter 4 describes the relationship between the SNR measurement and the antenna boresight vector. The first part of Chapter 5 presents an estimation method for a single spacecraft axis using the maximum likelihood estimate (MLE) of an antenna boresight vector. The second part examines the use of this vector for various scenarios of attitude

determination. Chapter 6 details the various data sets that are used to analyze the performance of the MLE technique. Chapter 7 presents and examines the results of the MLE approach applied to these sets.

## CHAPTER 2

### GPS BASED ATTITUDE BACKGROUND

#### 2.1 Introduction

This chapter describes the phase measurement made by GPS receivers and how these measurements are used to compute vehicle attitude. The first part details the computation of single difference phase measurements made between two antennas and time differenced phase measurements. These quantities are related to the baseline vector between the antennas and to the displacement of the baseline vector between two epochs, respectively. The next section presents the equations and quantities necessary to estimate the baselines and the baseline displacements. Finally, the baselines are related to three-axis and single-axis vehicle attitude.

#### 2.2 Phase Difference Measurements

The GPS satellites transmit an encoded carrier signal at 1575.42 MHz corresponding to a wavelength of 19.03 cm. To track this incoming signal, a GPS receiver, using the code correlation technique, must generate a similarly encoded reference signal at the same frequency [Hoffman-Wellenhof, et. al., 1992]. In this method, the reference signal is shifted with respect to time so that the two signals optimally match. The fractional phase difference is computed by

$$\phi = -f\delta t, \quad (2.1)$$

where  $\phi$  is the difference between the carrier phases of the two signals,  $f$  is the carrier frequency, and  $\delta t$  is the time between signal transmission and reception. This is known as the carrier beat phase. The unknown number of cycle shifts needed for perfect cycle synchronization is called the integer ambiguity. As the GPS satellites and receiving antennas move, the required time or Doppler shift changes. To maintain lock on the signal the receiver must continuously adjust the phase shift of the reference signal. As long as the receiver remains locked, the change in phase is tracked over any number of additional complete cycles or reduction in complete cycles. This is known as the “integrated Doppler” or “accumulated delta phase” [Axelrad and Brown, 1996]. However, if the receiver momentarily loses lock on the signal, the full cycle count becomes invalid and therefore, tracking must be restarted at the current phase fraction. This loss of signal lock is referred to as a cycle slip.

By using two antennas, the difference between the phase of the arriving carrier signal between the two antennas can be measured, as denoted by a  $\Delta$  in this research. As before, the measured difference is only a fractional measurement. The number of complete cycles between the two antennas is unknown. If the antennas are operating under a common receiver clock, then the phase difference between the two antennas is related to the baseline vector connecting the antennas by

$$\Delta\phi = (\mathbf{r}^L)^T \hat{\mathbf{e}}^L - k + \beta + v \quad (2.2)$$

where  $\mathbf{r}$  is the baseline vector,  $\hat{\mathbf{e}}$  is the line of sight to the GPS satellite,  $k$  is the integer ambiguity,  $\beta$  is the antenna line bias in fractions of a cycle,

and  $v$  is additional random noise. The line bias represents the difference in the delays between the two antennas caused by cable and electronic differences. The superscript  $L$  refers to the local system in which the line-of-sight (LOS) vectors are computed. Figure 2.1 show this relationship graphically.

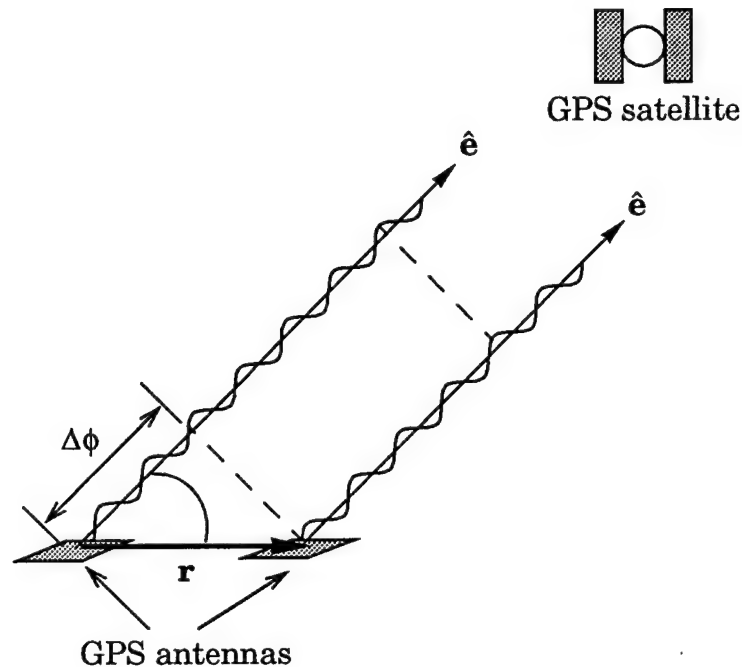


Figure 2.1. Relationship between an antenna phase difference and a baseline vector.

A third type of phase measurement used in this research is the time differenced measurement, denoted by a  $\delta$ . It is formed by differencing two  $\Delta\phi$  measurements taken with the same antenna pair at two distinct epochs. The time differenced phase measurement between epoch  $t_i$  and  $t_k$  is defined as

$$\delta\Delta\phi(t_i) \equiv \Delta\phi(t_{i+k}) - \Delta\phi(t_i). \quad (2.3)$$

Another type of phase difference that is not used in this research is between measurements from two different satellites. This is commonly denoted with the symbol  $\nabla$ .

### 2.3 Baseline Estimation from $\Delta\phi$ Measurements

Given two or more baseline vectors on a vehicle provided by three or more antennas, the attitude of the vehicle can be computed using GPS phase measurements. The baseline vectors are computed from a batch of  $\Delta\phi$  measurements taken from multiple GPS satellites. After neglecting the noise,  $M$  phase measurements from a GPS satellite  $i$  are related to the  $M$  baselines by

$$\Delta\phi_i = \hat{\mathbf{e}}_i^T \mathbf{B} + \mathbf{k}_i, \quad (2.4)$$

where

$$\Delta\phi_i = [\Delta\phi_{i1} \ \Delta\phi_{i2} \ \dots \ \Delta\phi_{iM}], \quad (2.5)$$

$$\mathbf{B} = [\mathbf{r}_1 \ \mathbf{r}_2 \ \dots \ \mathbf{r}_M], \quad (2.6)$$

and

$$\mathbf{k}_i = [(-k_{i1} + \beta_1) \ (-k_{i2} + \beta_2) \ \dots \ (-k_{iM} + \beta_M)]. \quad (2.7)$$

The integer ambiguities are found from the integer parts of the elements of  $\mathbf{k}$  and the line biases are found from the common fractional parts. Each GPS satellite and baseline pair has a unique integer ambiguity associated with it. However, the line bias are unique only to each baseline. If mea-

measurements from  $N$  GPS satellites are taken simultaneously, then an equation relating the phase differences to the baselines, LOS vectors, integers, and line biases is

$$\Delta\Phi = \mathbf{H} \begin{bmatrix} \mathbf{B} \\ \mathbf{K} \end{bmatrix}, \quad (2.8)$$

where

$$\Delta\Phi^T = \begin{bmatrix} \Delta\phi_1^T & \Delta\phi_2^T & \dots & \Delta\phi_N^T \end{bmatrix}, \quad (2.9)$$

$$\mathbf{H}^T = \begin{bmatrix} \hat{\mathbf{e}}_1 & \hat{\mathbf{e}}_2 & \dots & \hat{\mathbf{e}}_N \\ 1 & 0 & \dots & 0 \\ 0 & 1 & & \vdots \\ \vdots & & \ddots & 0 \\ 0 & \dots & 0 & 1 \end{bmatrix}, \quad (2.10)$$

and

$$\mathbf{K}^T = \begin{bmatrix} \mathbf{k}_1^T & \mathbf{k}_2^T & \dots & \mathbf{k}_N^T \end{bmatrix}. \quad (2.11)$$

The baselines, integers, and biases, are found by solving the normal equation in (2.8) for the matrices  $\mathbf{B}$  and  $\mathbf{K}$ .

In the matrix  $\mathbf{B}$  every baseline corresponds to three unknown vector components. Every GPS satellite creates one unknown integer ambiguity per baseline in the matrix  $\mathbf{K}$  and provides one phase measurement per baseline. This leaves more unknowns than equations. However, if the GPS receivers maintain a continuous track on the satellites, the integer ambiguities remain fixed over a number of measurements with only the baseline components changing. If there is a sufficient enough change in



the  $\mathbf{H}$  matrix, then this quickly leads to more measurements than unknowns, making Equation (2.8) overdetermined. For  $E$  measurement epochs,  $M$  baselines, and  $N$  GPS satellites, the requirement for Equation (2.8) to be overdetermined is

$$(3ME + MN) < MNE. \quad (2.12)$$

For the ratio of unknowns to measurements to be less than or equal to one the condition is

$$\frac{3E + N}{NE} < 1. \quad (2.13)$$

When  $N=1,2,3$  or  $E=1$  the ratio in Equation (2.13) is never smaller than one for any value of  $E$ . Therefore, a direct solution for both the baselines and integers requires a minimum of four satellites and two measurement epochs.

Much larger data sets are needed for reliable estimates. For example, to accurately determine the baselines with the TANS Vector, the user's manual recommends collecting data for a duration of at least 8 hours taken every 2 to 5 seconds [Trimble, 1993]. This is primarily to allow enough time for a sufficient change in the LOS vector components of the  $\mathbf{H}$  matrix. Furthermore, cycle slips and the inclusion of measurements from GPS satellites acquired in the middle of the data set create additional integer ambiguities that have to be computed.

## 2.4 Displacement Vector Estimation from $\delta\Delta\phi$ Measurements

Time differenced measurements can be used to estimate the displacement of a baseline between two measurement epochs, as illustrated in Figure 2.2. Given two  $\Delta\phi$  measurements at times  $t_i$  and  $t_k$ , the time dif-

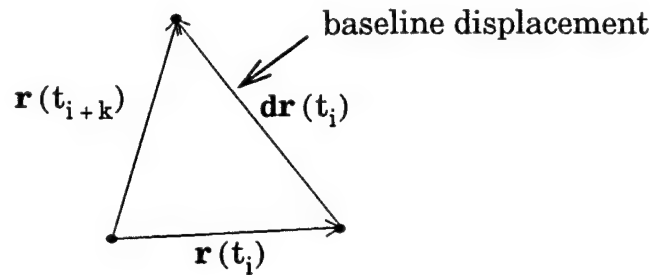


Figure 2.2. The displacement vector.

ferenced phase,  $\delta\Delta\phi(t_i)$ , can be computed using the definition presented in Equation (2.3). Substituting Equation (2.2) into Equation (2.3), assuming no cycle slips, and approximating the line of sight vector as constant over this interval, an equation involving the antenna displacement vector,  $\mathbf{dr}$ , can be formed as

$$\delta\Delta\phi(t_i) = \hat{\mathbf{e}}(t_i)^T \mathbf{dr}(t_i) + (\mathbf{k}_{i+k} - \mathbf{k}_i) + (\mathbf{v}_{i+k} - \mathbf{v}_i) . \quad (2.14)$$

When the receiver remains locked on to the satellite signal, the two integer ambiguities,  $\mathbf{k}_{i+k}$  and  $\mathbf{k}_i$ , are equal, resulting in

$$\delta\Delta\phi(t_i) = \hat{\mathbf{e}}(t_i)^T \mathbf{dr}(t_i) + (\mathbf{v}_{i+k} - \mathbf{v}_i) . \quad (2.15)$$

To solve Equation (2.15) for the three elements of  $\mathbf{dr}$ , measurements from at least three GPS satellites must be available. Assuming that the noise is uncorrelated, unbiased, and equi-variant, then the least squares solution is

$$\mathbf{dr}(t_i) = (\mathbf{G}^T \mathbf{G})^{-1} \mathbf{G}^T \begin{bmatrix} \delta\Delta\phi_1(t_i) \\ \delta\Delta\phi_2(t_i) \\ \vdots \\ \delta\Delta\phi_N(t_i) \end{bmatrix} \quad (2.16)$$

where

$$\mathbf{G} = [\hat{\mathbf{e}}_1 \ \hat{\mathbf{e}}_2 \ \dots \ \hat{\mathbf{e}}_N]^T, \quad (2.17)$$

the subscript refers to each satellite, and  $N$  is the number of satellites. If a cycle slip occurs between the measurement of  $\Delta\phi(t_i)$  and  $\Delta\phi(t_{i+k})$ , then the integer ambiguities at the two epochs are not equal and Equation (2.14) is not solvable. However, each cycle slip only affects the computation of a single displacement vector, making it a very robust observable.

In general, the use of this type of measurement usually does not produce high accuracy estimates because the measurement noise is higher and the geometry is weaker than the  $\Delta\phi$  or  $\nabla\Delta\phi$  observable. As a result, they are normally used for initialization such as in surveying to establish an initial estimate for long antenna baselines [Hoffman-Wellenhof, et. al., 1992] and in attitude determination as a means for initial ambiguity resolution [Cohen, 1996]. However, if there is a large and rapid movement of the baseline, then these two conditions are no longer a factor.

## 2.5 Attitude Estimation from Vector Observations

The attitude of the vehicle is defined as the matrix,  ${}^B\mathbf{C}^L$ , that relates a vector in a given local frame denoted by the superscript  $L$  to a

representation in a vehicle body fixed frame denoted by the superscript B. The representations of the vector,  $\mathbf{r}$ , in the two frames are related by

$$\mathbf{r}^B = {}^B\mathbf{C}^L \mathbf{r}^L, \quad (2.18)$$

where  ${}^B\mathbf{C}^L$  is the product of three Euler rotations computed by

$${}^B\mathbf{C}^L = \mathbf{R}_1(\theta) \mathbf{R}_2(\psi) \mathbf{R}_3(\lambda). \quad (2.19)$$

Given two non-parallel vectors,  $\mathbf{r}_1$  and  $\mathbf{r}_2$ , known in the vehicle fixed frame and measured in the local frame, an attitude matrix is determinable. Using the Gram-Schmidt process [Fraleigh and Beauregard, 1990] a set of orthonormal vectors,  $\mathbf{e}_1$ ,  $\mathbf{e}_2$ , and  $\mathbf{e}_3$  is computed by the equations

$$\begin{aligned} \mathbf{e}_1 &= \frac{\mathbf{r}_1^L}{\|\mathbf{r}_1^L\|}, \\ \mathbf{e}_2 &= \frac{\mathbf{r}_2^L - \left( \frac{\mathbf{r}_2^L \cdot \mathbf{e}_1}{\mathbf{e}_1 \cdot \mathbf{e}_1} \right) \mathbf{e}_1}{\left\| \mathbf{r}_2^L - \left( \frac{\mathbf{r}_2^L \cdot \mathbf{e}_1}{\mathbf{e}_1 \cdot \mathbf{e}_1} \right) \mathbf{e}_1 \right\|}, \end{aligned} \quad (2.20)$$

and

$$\mathbf{e}_3 = \|\mathbf{e}_1 \times \mathbf{e}_2\|.$$

The resulting local to body attitude matrix is

$${}^B\mathbf{C}^L = \begin{bmatrix} \mathbf{e}_1^T \\ \mathbf{e}_2^T \\ \mathbf{e}_3^T \end{bmatrix}. \quad (2.21)$$

For more than two observations, the noise in the measurements allow for multiple attitude matrices to be computed depending upon the choice of  $\mathbf{r}_1$  and  $\mathbf{r}_2$ . The best estimate of the attitude, minimizes the Wahba cost function

$$L({}^B\mathbf{C}^L) = \frac{1}{2} \sum_{k=1}^n a_k |\mathbf{r}^B - {}^B\mathbf{C}^L \mathbf{r}^L|, \quad (2.22)$$

where  $n$  is the number of non-parallel vector observations and  $a_k$  are the measurement weights. The solution to Equation (2.22) is the orthonormal matrix that best fits the measurements in a weighted least squares sense. Many solutions to Equation (2.22) have been previously offered [Markley, 1993], [Shuster, 1981], [Wahba, 1965].

## 2.6 Attitude Estimation from Phase Measurements

After collecting a batch of differential phase measurements over several epochs, the baselines in the local frame and the integer ambiguities are computed by solving Equation (2.8). Assuming the GPS receiver stays continuously locked on to the GPS satellite, the integer ambiguities only have to be determined once. New ambiguities are readily computed from the current information. After solving for the integers, the baselines are more easily estimated as they change. Rearrange Equation (2.8) to form

$$\Delta\Phi - \mathbf{K} = \mathbf{H}\mathbf{B} \quad (2.23)$$

where the  $\mathbf{H}$  matrix is simplified to

$$\mathbf{H}^T = [\hat{\mathbf{e}}_1 \ \hat{\mathbf{e}}_2 \ \dots \ \hat{\mathbf{e}}_n], \quad (2.24)$$

Solving for the baselines produces

$$\mathbf{B} = (\mathbf{H}^T \mathbf{H})^{-1} \mathbf{H}^T (\Delta\Phi - \mathbf{K}) . \quad (2.25)$$

In Equation (2.25) there are  $3M$  unknowns at every measurement epoch. Every GPS satellite gives  $M$  observations. Therefore, at least three satellites must be tracked to solve for the baselines explicitly at each epoch.

If at least two baselines are known in the body fixed frame, the results of Equation (2.25) are used to estimate the vehicle attitude. For two baselines, this attitude is computed by Equations (2.20) and (2.21). Multiple baselines require the minimization of Equation (2.22). Figure 2.3 shows an example representation of the antenna baselines in both the local and body frames. In this case the vehicle body  $y$ -axis is defined along one of the antenna baselines and the  $xy$ -body plane, the shaded region in the figure, is set as the plane containing both baselines.

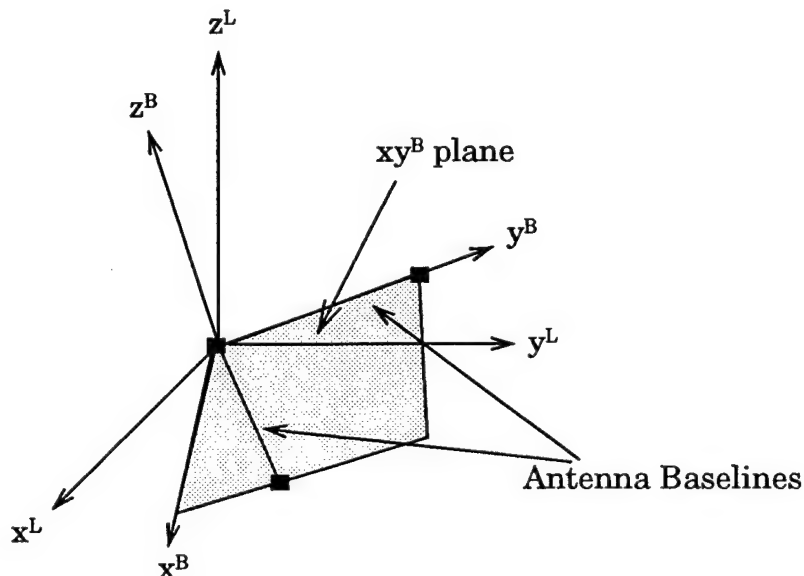


Figure 2.3. Relationship between antenna baselines and reference frames.

## 2.7 Single-Axis Attitude

As shown in Equation (2.19), three angles are required to completely define the vehicle attitude and thus, the three orthonormal axes. Single-axis attitude requires just two distinct angles. These two angles define the orientation of one of the body axes with respect to the reference frame as shown in Figure 2.4. The plane containing the other two axes is known to be perpendicular to the first axis. However, the orientation of the remaining two axes within the plane is not specified. Single-axis attitude is useful when the pointing direction of a single instrument is needed.

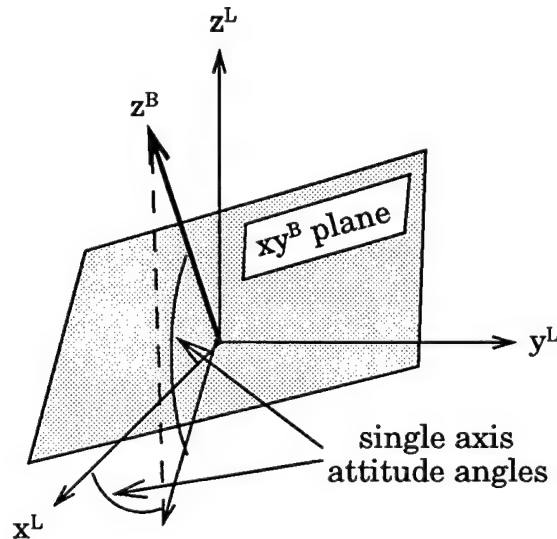


Figure 2.4. Single-axis attitude.

One example of a vehicle with the requirement for only single-axis attitude knowledge is a spinning satellite. As described in more detail in Chapter 3, a spinning satellite has only one inertially fixed axis. The other two are continuously rotating about this axis. The placement of GPS antennas on the plane containing these rotating axes creates a baseline

vector that undergoes both large and rapid displacement. As a result, the problems with using the displacement vector observable, as discussed at the end of section 2.4, are not a significant factor. This measurement is the basis for the attitude estimation techniques presented in the next chapter.

Another area where single-axis estimation is useful is for integer ambiguity resolution. As discussed in Sections 2.3 and 2.6, baseline and attitude estimation using phase measurements have an ambiguity that must be determined. This is accomplished when either a certain number of measurements are available or by using a search technique to evaluate all of the possible integer combinations. The performance of the latter method is improved if the search space is narrowed. The phase-based method described by Ward [Ward, L.M., 1996], requires a single axis to be known to within 20 degrees for a rapid determination of the attitude and integer ambiguities.

## 2.8 Conclusions

A variety of phase difference measurements can be computed from the GPS signal. The basic phase measurement,  $\phi$ , is formed by synchronizing the GPS receiver reference signal with the incoming satellite signal. The observable,  $\Delta\phi$ , is made by differencing the phase measurements between two antennas. Differencing this value between two epochs forms  $\delta\Delta\phi$ .

The complete vehicle attitude with respect to a local system is specified by determining the components of two or more body axes in this system. A GPS receiver may estimate the body axes in the local system through the use of  $\Delta\phi$  measurements. This process consists of first deter-



mining the integer ambiguities of the carrier phase between antennas, estimating the receiver line biases, and the baseline components. Afterwards, only the baseline components need to be computed.

Single-axis estimation has fewer unknowns to estimate at the cost of a less specific representation of attitude. The  $\delta\Delta\phi$  measurements are useful in determining attitude for this case. The next chapter explores a technique specifically for spinning satellites. The estimation process is shown to be simpler and have fewer requirements than for three-axis attitude. One significant advantage is that there is no need for ambiguity resolution.

## CHAPTER 3

### GPS PHASE-BASED SPIN AXIS ESTIMATION

#### 3.1 Introduction

In this chapter several methods are described that use the displacement vector observable, as presented in the previous chapter, to determine the angular rates and the spin axis of a rotating satellite. For angular rate estimation, two frequency domain and one time domain technique are presented. The first frequency domain method is based on the Fast Fourier Transform (FFT), the second is based on the Auto-Regressive (AR) system model. The time domain method involves an averaging of the displacement vectors. For spin axis estimation, an averaging technique using displacement vector cross products and a batch filter are presented. It is shown that the AR model is the best approach for estimating the satellite frequencies. The cross product method is the simplest technique for estimating the spin axis and it works as well as the batch filter algorithm. They both have estimation errors of under 0.1 deg after 400 measurements. The batch filter has the advantage of being able to estimate more parameters than the cross product method.

This chapter begins with a description of an ideal spinning satellite model and the simulated data generated from it. This is followed by a description of a ground-based, hardware simulation of the satellite motion. An actual GPS receiver is used to collect the experimental data. For this

work, both the computer and hardware simulations are based on a receiver that generates phase difference observations ( $\Delta\phi$ ) between two antennas and computes appropriate line-of-sight vectors ( $\hat{e}$ ) to the GPS satellites based on its current navigation solution. Note that the receiver is assumed to be operating in a steady state condition - that is, it has already acquired at least four satellites and is computing position solutions in real-time. The acquisition process typically takes up to 30 seconds for a receiver that has been initialized with an a priori estimate of the orbit, GPS ephemeris, and time, and up to 30 minutes for a receiver in "cold-start". The remaining sections of this chapter describe the frequency and attitude estimation algorithms and the corresponding results from using both the simulated and experimental data.

### 3.2 Spinning Satellite Model

Figure 3.1 illustrates the important quantities describing the kinematics of a spinning satellite. For simplicity, the vehicle is assumed to be axisymmetric about the  $z^B$ -axis. The master antenna is located at the center with the master-slave baseline perpendicular to the axis of symmetry. The satellite rotates about the  $z^B$ -axis at a rate of  $\omega_p$ . Simultaneously, the  $z^B$ -axis rotates about the angular momentum axis,  $\hat{H}$ , at the rate  $\omega_l$  at an angle of  $\theta$ . The satellite has a moment of inertia about the  $z^B$ -axis of  $I_s$  and moment of inertia about the  $x^B$  and  $y^B$ -axes of  $I_t$ .

The body  $x^B$ -axis is defined by the position of the slave antenna. The relationships between  $\omega$ ,  $\omega_p$ ,  $\omega_l$ ,  $\theta$ , and the inertias are

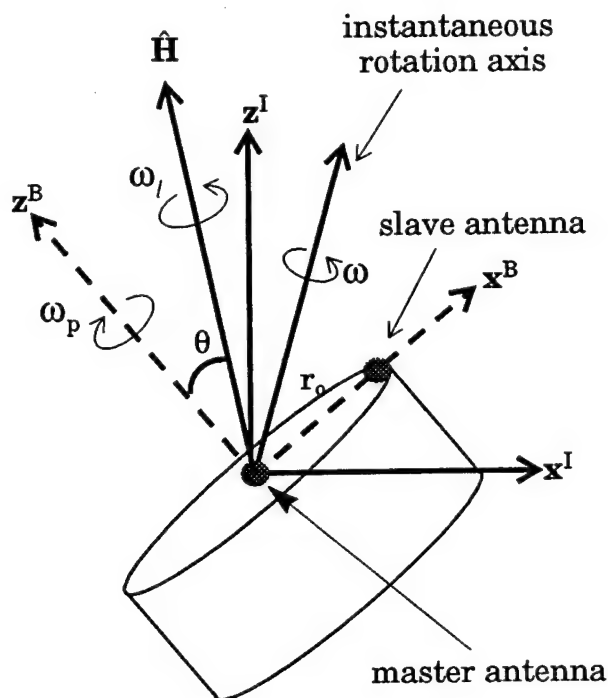


Figure 3.1. Kinematic model.

$$\omega_p = \frac{I_t - I_s}{I_s} \omega_I \cos \theta \quad (3.1)$$

and

$$\omega^2 = \omega_p^2 + \omega_I^2 + 2\omega_p \omega_I \cos \theta. \quad (3.2)$$

The body frame is fixed to the rotating satellite and is denoted with a superscript B. The angular momentum frame, denoted by the superscript H, is defined with the z-axis along the spacecraft angular momentum vector. The inertial frame is designated by the superscript I. The angular momentum vector unit vector,  $\hat{H}$ , in the inertial frame is

$$\hat{\mathbf{H}}^I = [\mathbf{h}_x \ \mathbf{h}_y \ \mathbf{h}_z]^T. \quad (3.3)$$

### 3.2.1 Antenna Motion

In the absence of external torques, a GPS antenna on the rim of a spinning satellite moves according to the model described in Equations (3.1) and (3.2). In the body fixed system, the antenna position remains constant. The position of the antenna with respect to the center of the spacecraft in the inertial system can be computed from the product of two separate rotation matrices given by

$$\mathbf{r}^I = {}^I\mathbf{C}^H {}^H\mathbf{C}^B \mathbf{r}^B, \quad (3.4)$$

where

$$\mathbf{r}^B = [\mathbf{r}_o \ 0 \ 0]^T \quad (3.5)$$

is the position of the antenna in the body frame. The first rotation,  ${}^H\mathbf{C}^B$ , takes  $\mathbf{r}$  from the body to the angular momentum frame. The angles  $\psi$  and  $\phi$  are defined as functions of the satellite rotation rates as follows:

$$\begin{aligned} \psi &= \omega_p t + \psi_o \\ \phi &= \omega_l t + \phi_o \end{aligned} \quad (3.6)$$

Then  ${}^H\mathbf{C}^B$  can be expressed as

$${}^H\mathbf{C}^B = \begin{bmatrix} c\psi c\phi - c\theta s\psi s\phi & -s\psi c\phi - c\theta c\psi s\phi & s\theta s\phi \\ c\psi s\phi + c\theta s\psi c\phi & -s\psi s\phi + c\theta c\psi c\phi & s\theta c\phi \\ s\theta s\psi & s\theta c\psi & c\theta \end{bmatrix} \quad (3.7)$$

The matrix  ${}^I\mathbf{C}^H$  rotates a vector from the angular momentum system to the inertial system. It is defined by the two angles  $\eta$  and  $\sigma$  which

are determined from the components of the angular momentum unit vector by

$$\eta = \cos^{-1} \left( \frac{h_x}{\sqrt{h_x^2 + h_y^2}} \right) \quad (3.8)$$

and

$$\sigma = \cos^{-1}(h_z). \quad (3.9)$$

This matrix is

$${}^I\mathbf{C}^H = \begin{bmatrix} c\eta c\sigma & -s\sigma & c\eta s\sigma \\ s\eta c\sigma & c\eta & s\eta s\sigma \\ -s\sigma & 0 & c\sigma \end{bmatrix}. \quad (3.10)$$

If Equation (3.4) is differenced in time, an expression relating the antenna displacement vectors to the satellite kinematics can be formulated. For a constant orientation of a satellite angular momentum vector, this relationship at time  $t_i$  is

$$\mathbf{dr}^I(t_i) = {}^I\mathbf{C}^H [ {}^H\mathbf{C}^B(t_{i+k}) - {}^H\mathbf{C}^B(t_i) ] \begin{bmatrix} \mathbf{r}_o \\ 0 \\ 0 \end{bmatrix}. \quad (3.11)$$

The displacement vectors in the local frame are computed from the GPS phase differences by Equation (2.16). Equation (3.11) describes how these components are related to the spacecraft attitude.

The frequencies observed in  $\mathbf{dr}^I$  are due to the products of the sines and cosines in Equation (3.7). The three frequencies are  $\omega_l \pm \omega_p$  and  $\omega_p$ .

### 3.2.2 Computer Simulation

A computer program was constructed to simulate the motion of a spinning satellite in low earth orbit. LOS measurements are generated from a simulated constellation of 24 GPS satellites using a typical set of orbital elements and taking into account satellite visibility limitations. Perfect phase difference values are formed from the line of sight and known antenna baseline vectors. Simulated  $\Delta\phi$  measurements are constructed by adding zero mean Gaussian noise with a standard deviation of 5 mm. Displacement vectors are computed from the noisy  $\Delta\phi$  values. Measurements are recorded at 2 Hz for 12 minutes. The spin rate is 5 rpm and the nutation angle is 5 deg.

In the remainder of this chapter the rotation matrices referring to the simulated LEO motion are denoted with a subscript "s". Thus, the expressions given in Equations (3.7) and (3.10) are for  ${}^H C_s^B$  and  ${}^I C_s^H$ , respectively.

## 3.3 Ground Experiment

In order to validate the results of the computer simulation, a series of ground tests was conducted. Data were taken from a GPS receiver mounted on a spin table located at a Naval Research Laboratory test facility. The matrices describing the experimental motion are denoted with the subscript "e".

### 3.3.1 Experimental Apparatus

The complete test apparatus consists of two pieces of equipment with a combined total of three rotational axes as diagramed in Figure 3.2. A photograph of the actual setup is shown in Figure 3.3. The TRT-7 two-

axis tilter is mounted on a support base. In the local level coordinate frame, the first axis is oriented along an east-west direction. The second axis is aligned perpendicular to the first and rotates around it. When the first rotation angle is zero, the second axis lies in the north-south direction. The maximum tilt angle about both axes is approximately  $\pm 45$  degrees. The second piece of equipment is the BDS-5 spinner. It provides a constant angular rate about a third axis. This axis rotates according to the tilt angles of the TRT-7. It is mounted so that when the first two rotation angles are zero its orientation is in the up-down direction. The GPS antennas are mounted on the top plane of the satellite structure perpendicular to this axis.

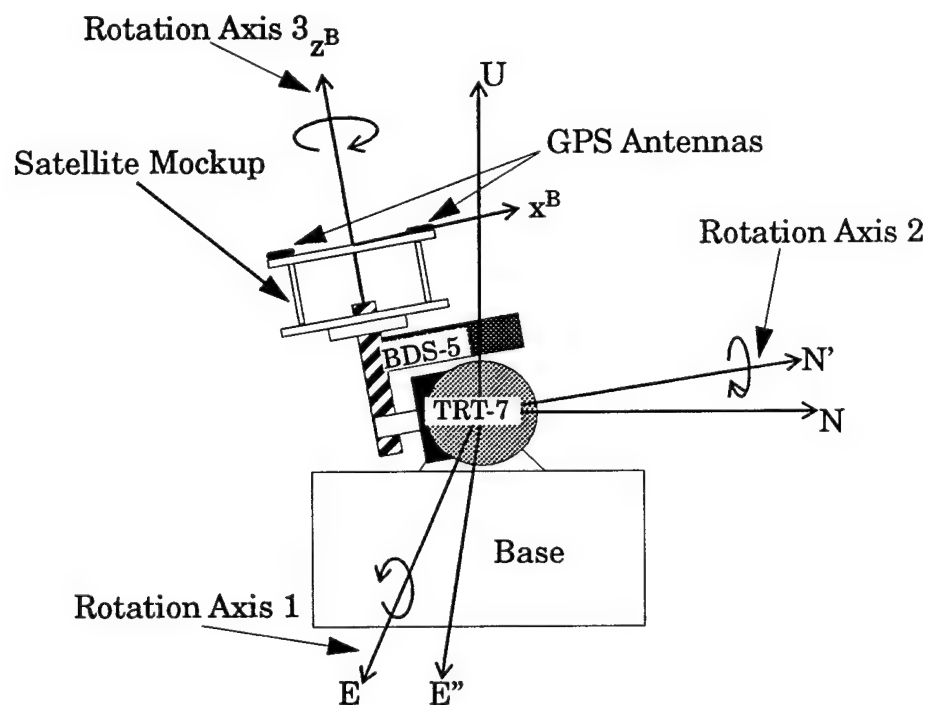


Figure 3.2. Equipment diagram.



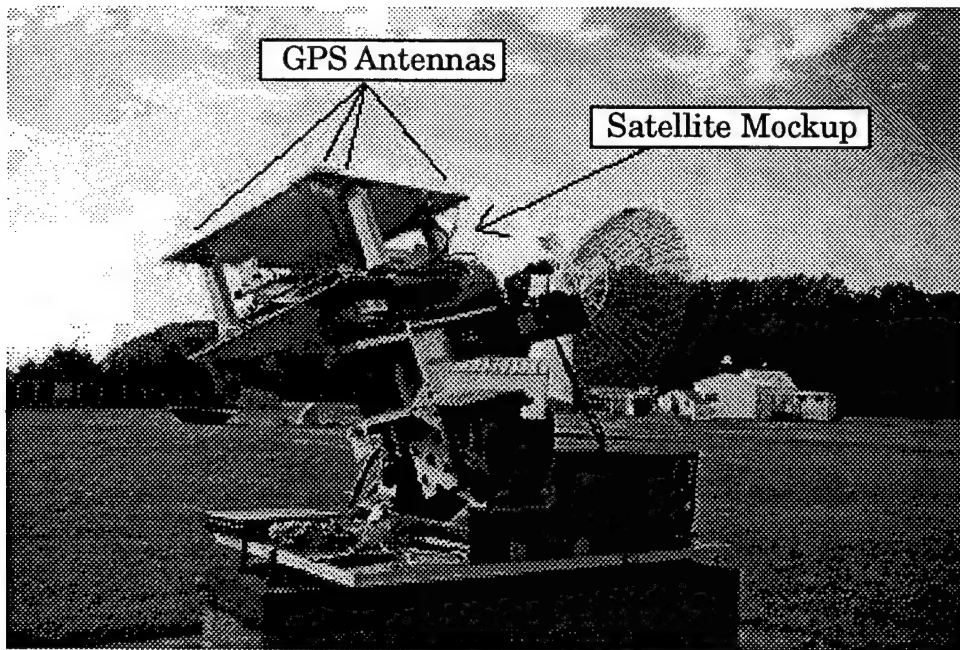


Figure 3.3. Experimental setup.

### 3.3.2 Experimental Motion

The matrix  ${}^H C_s^B$ , derived in Equation (3.7) is a 3-1-3 sequence of rotations computed from the Euler angles  $\psi$ ,  $\phi$ , and  $\theta$ . In order to properly simulate the motion of a spinning satellite, the structure in the experimental setup has to be moved according to the rotations defined by the TRT-7 and the BDS-5. For this case, the body frame is defined by the symmetry axis of the structure and the position of one of the GPS antennas as shown in Figure 3.2. In the body frame the position of the GPS antenna is always on the  $x^B$ -axis. The local system is defined by the orientation of the TRT-7's tilt axis when the plane of the structure is level to the ground. While there is no true angular momentum axis, an equivalent frame to the angular momentum frame is defined by the plane of the satellite structure when

there is only pure spin. For the purpose of comparison to the simulated data, this is referred to as the H frame.

If the east direction is called the 1-axis, the north direction the 2-axis, and the up direction the 3-axis, then the series of rotations used to move the GPS antenna is a 1-2-3 sequence. Defining the three rotation angles as  $\beta$ ,  $\alpha$ , and  $\gamma$ , respectively, the total rotation matrix is

$${}^B C_e^H(\beta, \alpha, \gamma) = R_3(\gamma) R_2(\alpha) R_1(\beta). \quad (3.12)$$

In order to simulate the correct movement of a GPS antenna on a spinning satellite governed by Equation (3.7), the angles  $\beta$ ,  $\alpha$ , and  $\gamma$ , must be varied in time as a function of  $\psi$ ,  $\phi$ , and  $\theta$ . These relations are computed by setting

$${}^B C_e^H(\beta, \alpha, \gamma) = {}^B C_s^H(\phi, \theta, \psi). \quad (3.13)$$

The resulting expressions for  $\alpha$ ,  $\beta$ , and  $\gamma$ , are a function of the sums and products of the sinusoids of  $\phi$ ,  $\theta$ , and  $\psi$ . These general equations are very involved; however, for small nutation angles they may be approximated by

$$\beta(t) \approx \theta \sin(\phi(t)), \quad (3.14)$$

$$\alpha(t) \approx \theta \cos(\phi(t)), \quad (3.15)$$

and

$$\gamma(t) \approx \phi(t) + \psi(t). \quad (3.16)$$

Due to limitations in the control and performance of the test equipment, two compromises are required. The first is to eliminate the motion

of  $\beta$  due to Equation (3.14). The second is to approximate the motion of  $\alpha$  in Equation (3.15) with a triangle wave. The equation for  $\alpha$  is

$$\alpha(t) \approx \theta \frac{8}{\pi^2} \left[ \sin(\lambda(t)) - \frac{1}{9} \sin(3\lambda(t)) + \frac{1}{25} \sin(5\lambda(t)) - \dots \right] \quad (3.17)$$

where

$$\lambda(t) = \omega_\alpha t + \lambda_0 \quad (3.18)$$

and

$$\omega_\alpha = \frac{2\theta}{\pi} \omega_l. \quad (3.19)$$

Combining the motion of  $\alpha$  about the 2-axis and the motion of  $\gamma$  about the 3-axis yields the rotation matrix from the body system to the angular momentum system:

$${}^H C_e^B = \begin{bmatrix} c\gamma c\alpha & -s\gamma c\alpha & s\alpha \\ s\gamma & c\gamma & 0 \\ -c\gamma s\alpha & s\gamma s\alpha & c\alpha \end{bmatrix} \quad (3.20)$$

The resulting motion described by Equation (3.20) and illustrated in Figure 3.4 is a combination of spinning and tipping.

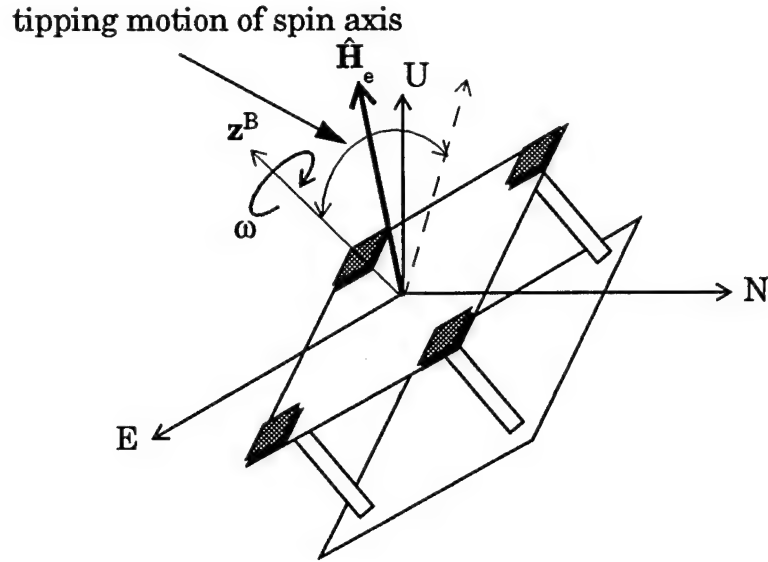


Figure 3.4. Spinning and tipping motion.

The tipping is contained in a single plane centered on the  $\hat{H}_e$  axis. The orientation of  $\hat{H}_e$  is fixed and described by the two angles  $\sigma$  and  $\eta$ . The angle  $\sigma$  is about the 1-axis and the angle  $\eta$  is about the 2-axis. The corresponding rotation matrix from the  $\hat{H}_e$  frame to the inertial system is

$${}^I C_e^H = \begin{bmatrix} c\eta & 0 & s\eta \\ s\eta s\sigma & c\sigma & -c\eta s\sigma \\ -s\eta c\sigma & s\sigma & c\eta c\sigma \end{bmatrix}. \quad (3.21)$$

The rotation matrices in Equations (3.20) and (3.21) are analogous to the matrices in Equations (3.7) and (3.10) for the true satellite rotations. One difference is that in the case of an actual spinning satellite, the spin axis rotates about the angular momentum axis; whereas for the experimental motion the spin axis tips about some central axis. Another difference is in the frequency modes of the ground experiments.

### 3.3.3 Experimental Motion Frequencies

For this case the two principle rates are  $\omega$  and  $\omega_\alpha$  and the observed frequencies are at  $\omega$  and  $\omega \pm k\omega_\alpha$ , where  $k$  is any integer. The frequencies contained in the experimental motion are similar to those of a spinning satellite. It is shown that the equations for satellite motion contain three frequencies derived from the two satellite rates of  $\omega_p$  and  $\omega_l$ . For the experiment, there is a frequency due to the rate about the spin axis and frequencies due to the combined rates of the spin axis and the tilting motion about a fixed vector. Because  $\alpha(t)$  is a triangle wave it also contains odd harmonics of  $\omega_\alpha$  as opposed to just a single frequency. Thus cosine  $\alpha$  contains even multiples while the sine  $\alpha$  contains odd ones. A Power Spectral Density (PSD) plot of the displacement vectors yields an infinite number of spikes corresponding to all possible values of  $k$ . However, only the first few multiples of  $\omega_\alpha$  have enough power to show above the noise floor.

The reference value for the ground test spin rate was  $0.0850 \text{ Hz} \pm 7 \times 10^{-4} \text{ Hz}$ . The platform was leveled to within 1 deg and the initial alignment error was determined to be  $\pm 0.01 \text{ deg}$ .

### 3.3.4 GPS Receiver

The experiments were conducted using a Trimble Navigation TANS Vector Attitude Receiver [Cohen, 1992], [Trimble, 1993]. This receiver has 6 parallel tracking channels which multiplex among four antennas to provide attitude estimates as well as a navigation solutions. One antenna is designated as the master and the other three are slaves. The receiver measures the relative carrier phase for each slave with respect to the master. For these experiments the raw differential phase data is recorded at a

rate of 2 Hz. Typical differential phase errors for the receiver are in the range of 2-5 mm 1- $\sigma$  depending on the signal environment [Axelrad and Chesley, 1993].

The next sections describe various algorithms for attitude and frequency estimation.

### 3.4 Frequency Estimation Techniques

In this section, three frequency estimation techniques are examined. The first method is a time domain technique, while the next two are frequency domain methods.

#### 3.4.1 Displacement Vector Magnitude Algorithm

For small nutation angles,  $\omega$  can be approximated by averaging the values of a quantity denoted by  $\omega^*$  that is computed from the displacement vectors. If accurate values of the satellite's inertia ratios are known, estimates of  $\omega_p$  and  $\omega_l$  can also be found. The simplest approximation for the angular velocity  $\omega$  given in Equation (3.2) can be computed from the magnitude of  $d\mathbf{r}$ . Every two successive positions of a rotating antenna creates an angular displacement centered at the spin axis. This angle shown in Figure 3.5 is computed by

$$\Theta = 2 \sin^{-1} \left( \frac{\frac{1}{2} |d\mathbf{r}|}{r_o} \right) \quad (3.22)$$

where  $r_o = |\mathbf{r}|$ . Defining  $\omega^*$  as the mean angular rate of  $\Theta$ , the magnitude of  $\omega^*$  varies with  $\omega_p$ , its minimum value is  $\left( \frac{I_t}{I_t - I_s} \right) \omega_p$  and its maximum value is  $\omega$ . For a nutation angle of zero,  $\omega = \omega^*$ .

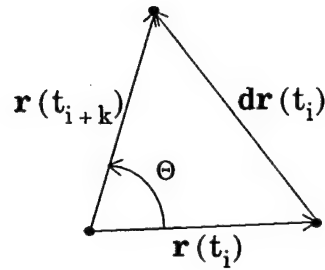


Figure 3.5. Angular displacement.

### 3.4.2 FFT Algorithm

To determine the modal frequencies and modal amplitudes of a signal, the following steps are applied: perform a discrete FFT on the sampled signal data; compute the power spectral density (PSD) of the transformed data; identify the peaks of the PSD; determine the frequency at which each peak occurs; and relate these frequencies back to a kinematic model.

Using only the PSD values, the frequencies are the most likely estimates of each signal mode. Ideally, they are the exact frequencies of the modes. However, the sampling properties of the signal can lead to errors.

The frequency resolution of the DFFT is equal to the sample frequency divided by the number of data points. Ideally, the signal should be sampled so that the modal frequencies are integer multiples of the frequency bin. In reality, however, the peaks of the PSD occur in the frequency bins that are closest to the correct modes. The signal power of each mode is spread over a range of frequency bins surrounding the correct frequency. In order to determine a better estimate, the frequency center of

the bins is computed by weighting them according to their power. However, the benefit of this approach may be limited by noise.

In the implementation of an FFT algorithm there are no assumptions about the structure of the signal. In other words, the FFT can be applied to any type of signal. There are other frequency estimation methods which can take advantage of the knowledge of the signal's structure. The next section discusses one of these parametric methods called the autoregressive or AR method.

### 3.4.3 AR Algorithm

In general, a discrete-time process can be well approximated by a time series or rational transfer function model [Kay, 1988]. In particular a system of order  $2p$ , can be represented by the recursive difference relation

$$x[n] = - \sum_{k=1}^{2p} a[k] x[n-k] + u[n] . \quad (3.23)$$

Taking the Z-transform of Equation (3.23) yields the transfer function

$$\frac{X(z)}{U(z)} = \frac{1}{P(z)} \quad (3.24)$$

where

$$z = e^{\sigma + j\theta} \quad (3.25)$$

and



$$P(z) = 1 + \sum_{k=1}^{2p} a[k] z^{-k}. \quad (3.26)$$

Given a sequence of sampled data  $x[n]$ , the coefficients,  $a[k]$ , can be estimated using the modified covariance method [Kay, 1988]. The roots of  $P(z)$  corresponding to sinusoids are described by

$$z_k^* = e^{\pm j\theta_k^*}. \quad (3.27)$$

They occur in complex conjugate pairs and lie on the unit circle (i.e.  $\sigma = 0$ ) at angles corresponding to the sinusoidal frequencies normalized by the sample frequency:

$$\theta_k^* = 2\pi\bar{f}_k, \quad \bar{f}_k = \frac{f_k}{f_s} \quad (3.28)$$

Note that this technique directly estimates the modal frequencies and therefore does not provide estimates which are quantized by discrete frequency bins as does the FFT method.

The poles corresponding to the signal modes lie closest to the unit circle, while the poles corresponding to the noise lie farther away. The angles of the signal mode poles are approximately equal to  $2\pi\bar{f}_k$ . This is illustrated in Figure 3.6. For the ideal case where there is no noise the signal is perfectly modeled by Equation (3.26), with exactly  $p$  sinusoids, and each pole of Equation (3.24) lies exactly on the unit circle at an angle of  $2\pi\bar{f}_k$ . For the more realistic case a higher order model than  $2p$  is used to account for the noise in the signal. As the model order is increased, there are more frequencies available for the noise. As a result, the poles for the signal modes get closer to the unit circle and the angles get closer to  $2\pi\bar{f}_k$ .

The model order is limited by the number of samples,  $N$ . A maximum order of  $N/2$  is recommended [Kay, 1988]. The model order used in this work is 70 for values of  $N$  that are 200 and greater.

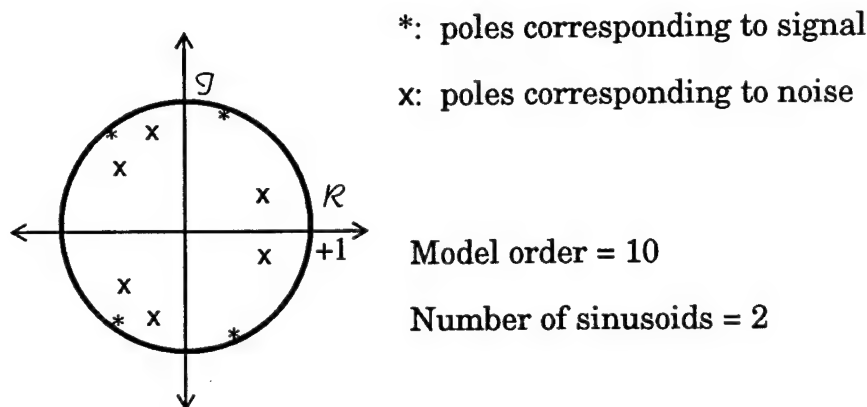


Figure 3.6. The pole - frequency relationship for a noisy sampled signal.

### 3.4.4 Frequency Estimation Results

The performance of the frequency estimation techniques are evaluated on both the simulated and experimental data. The AR and displacement vector magnitude methods produce frequency errors under 0.01 rad/s after 30 seconds of data. The FFT method can not resolve the frequencies with this small of a data set and still shows large errors after 100 seconds. For large batch sizes, the errors are below 0.001 rad/s for both the AR and FFT techniques. Averaging  $\omega^*$ , however, does not show improvement with larger amounts of data. Tables 3.1 and 3.2 compare the performance of the three frequency estimation techniques as a function of the data batch size. All of the data is sampled at 2 Hz. For the simulation data, the nutation angle is 5 deg. For the experimental data the maximum tip angle is 5.3 deg. In the experiment the programmed value for  $\omega_a$  is 0.628 rad/s. How-

ever, due to the limitations of the equipment as noted earlier, this number is believed to be significantly in error. Judging by the consistency of the methods over various batch sizes and by the simulation results, it is believed that the results from the frequency estimation algorithms more accurately represent the actual motion than the programmed values.

Table 3.1. Performance of frequency methods on simulated data.

Method	N = 100		N = 200		N = 800	
	$\omega_l$ (rad/s)	$\omega_p$ (rad/s)	$\omega_l$ (rad/s)	$\omega_p$ (rad/s)	$\omega_l$ (rad/s)	$\omega_p$ (rad/s)
True Value	0.6789	-0.1561	0.6789	-0.1561	0.6789	-0.1561
AR	0.6760	-0.1530	0.6779	-0.1550	0.6794	-0.1565
FFT	no sol.	no sol.	0.6473	-0.1226	0.6795	-0.1562
Average $\omega^*$	0.6780	-0.1565	0.6748	-0.1557	0.6759	-0.1560

Table 3.2. Performance of frequency methods on experimental data.

Method	N = 100		N = 200		N = 800	
	$\omega$ (rad/s)	$\omega_\alpha$ (rad/s)	$\omega$ (rad/s)	$\omega_\alpha$ (rad/s)	$\omega$ (rad/s)	$\omega_\alpha$ (rad/s)
Reference Value	0.5349	(1)	0.5349	(1)	0.5349	(1)
AR	0.5379	0.5807	0.5356	0.5959	0.5345	0.5973
FFT	no sol.	no sol.	0.5381	0.5947	0.5350	0.5971
Average $\omega^*$	0.5337	(2)	0.5350	(2)	0.5358	(2)

Note: (1) There is no adequate reference value for  $\omega_\alpha$ .

(2) The average  $\omega^*$  method does not produce estimates for  $\omega_\alpha$ .

### 3.5 Attitude Estimation Techniques

This section presents two methods for determining the orientation of the spacecraft angular momentum vector. The first technique uses the

average of the displacement vector cross products. The second uses a batch processor.

### 3.5.1 Cross Product Algorithm

In the absence of nutation, a GPS antenna located on one face of a rotating satellite travels in a plane perpendicular to the angular momentum axis. The displacement vector of the baseline formed by two moving antenna is also in this plane. Taking the cross product of two displacement vectors yields a vector with approximately the same orientation as the angular momentum axis. Furthermore, the components of  $\hat{\mathbf{H}}$  define the orientation of the satellite spin axis in the inertial frame. Because the GPS measurements are taken in the inertial frame, the displacement vector cross products are computed in the inertial frame, and therefore,  $\hat{\mathbf{H}}$  is also computed in the inertial frame.

When nutation is introduced, the cross product of two successive displacement vectors is not the true orientation of  $\hat{\mathbf{H}}$ . However, as the satellite's instantaneous spin axis rotates about  $\hat{\mathbf{H}}$ , the average of all the vectors formed from these cross products tends towards the actual orientation of  $\hat{\mathbf{H}}$ . This is computed by

$$\hat{\mathbf{H}} = \frac{1}{N} \sum_{i=1}^N \frac{\mathbf{dr}(t_i) \times \mathbf{dr}(t_{i+k})}{|\mathbf{dr}(t_i) \times \mathbf{dr}(t_{i+k})|} \quad (3.29)$$

where  $N$  is the number of measurements.

### 3.5.2 Spinning Satellite Batch Processor

A batch processing algorithm for estimation of the attitude is also examined. The state comprises the nutation angle  $\theta$ , the angular position

of the antenna about the body  $z^B$ -axis  $\psi$ , the angular position about  $\hat{H}_s$ ,  $\phi$ , and the two constant angles,  $\eta$  and  $\sigma$ , which relate the inertial to the angular momentum frame. The resulting state vector is

$$\mathbf{X} = [\theta \ \psi \ \phi \ \eta \ \sigma]^T. \quad (3.30)$$

For the torque free case considered here, the state estimate is propagated between measurement epochs as follows:

$$\hat{\mathbf{X}}(t_{i+1}) = \hat{\mathbf{X}}(t_i) + \begin{bmatrix} 0 \\ \omega_p \delta t \\ \omega_l \delta t \\ 0 \\ 0 \end{bmatrix} \quad (3.31)$$

where

$$\delta t = t_{i+1} - t_i. \quad (3.32)$$

The two frequencies are determined by one of the previously described frequency estimation techniques.

The measurement model which relates the displacement vectors to the states is inherently nonlinear as the states are embedded in the elements of the attitude matrix. The nonlinear measurement equation is given by

$$h(\mathbf{X}) = \frac{d\mathbf{r}^I(t_i)}{r_o} = {}^I\mathbf{C}^H [ {}^H\mathbf{C}^B(t_{i+k}) - {}^H\mathbf{C}^B(t_i) ]. \quad (3.33)$$

For the gain and covariance update calculations the linearized measurement connection or sensitivity matrix is

$$H \equiv \left. \frac{\delta h}{\delta \mathbf{X}} \right|_{\mathbf{x}_i} . \quad (3.34)$$

Simulated data is generated using a nutation angle of 5 deg, an inertia ratio of 1.3, and a sample frequency of 2 Hz. The two driving frequencies,  $\omega_p$  and  $\omega_n$ , are -0.1561 rad/s and 0.6789 rad/s, respectively.

### 3.5.3 Ground Experiment Batch Processor

The batch processing algorithm for the experimental data is very similar to the one employed for the computer simulation. The estimated values are the angular position of the antenna about the body  $z^B$ -axis,  $\gamma$ , the amplitude,  $\theta$ , of the tipping motion, the argument for the equation for  $\alpha(t)$ ,  $\lambda$ , and the two angles,  $\sigma$  and  $\eta$ . The resulting state vector is

$$\mathbf{X} = [\gamma \ \theta \ \lambda \ \eta \ \sigma]^T . \quad (3.35)$$

As described in section 3.3.2, the induced motion is designed to simulate torque free satellite motion. As a result, the  $\eta$  and  $\sigma$  stay fixed. The magnitude and rate of the tipping motion remain constant. The position angles,  $\gamma$  and  $\lambda$ , change according to the two driving rates,  $\omega$  and  $\omega_\alpha$ , respectively. The transition between measurement times is therefore

$$\hat{\mathbf{X}}(t_{i+1}) = \hat{\mathbf{X}}(t_i) + \begin{bmatrix} \omega \delta t \\ 0 \\ \omega_\alpha \delta t \\ 0 \\ 0 \end{bmatrix}. \quad (3.36)$$

The driving frequencies are estimated using the frequency analysis techniques. The observations equations are the same as shown in Equations (3.33) and (3.34).

The phase difference  $\Delta\phi$  and LOS measurements are collected at a sample rate of 2 Hz using a Trimble TANS Vector receiver. The spin and tipping rates,  $\omega$  and  $\omega_\alpha$ , are set at 0.535 rad/s and 0.597 rad/s, respectively. The tipping amplitude is 5.3 deg.

### 3.5.4 Estimation Results

The estimation errors for  $\eta$  and  $\sigma$  are approximately the same when using either the cross product or batch algorithms. When  $N$  is 400 or greater, the errors are under 0.1 deg. The batch processor allows for the estimation of additional parameters as well. For the largest batch sizes the simulation nutation angle and the experimental tip angle are both determined to within 0.1 deg. Estimation of the phase angles is the least accurate. The simulation angles,  $\psi$  and  $\phi$ , are determined to about 0.2 deg. However, the experimental angle,  $\gamma$ , is only estimated to within 2 deg. Tables 3.3 and 3.4 shows the performance of the attitude methods for various values of  $N$  for both the simulated and experimental cases. All of the data is taken at 2 Hz. For the simulation, the frequency is 5 RPM, and the nutation angle is 5 deg. For the experiment, the spin frequency is 5 RPM and the tipping rate is 2 deg/s.

Table 3.3. Performance of attitude methods on simulated data.

Method	Angle	True value (deg)	Estimated value (deg)		
			N = 200	N = 400	N = 800
<b>dr</b> Cross-Product	$\eta$	63.43	63.46	63.46	63.46
	$\sigma$	65.91	65.90	65.89	65.91
Batch Processor	$\eta$	63.43	63.47	63.45	63.45
	$\sigma$	65.91	65.93	65.92	65.91
	$\theta$	5.00	4.96	4.98	4.99
	$\psi$	90.00	91.82	90.34	89.83
	$\varphi$	90.00	88.23	89.59	90.18

Table 3.4. Performance of attitude methods on experimental data.

Method	Angle	Reference value (deg)	Estimated value (deg)		
			N = 200	N = 400	N = 800
<b>dr</b> Cross-Product	$\eta$	0.60	0.34	0.52	0.56
	$\sigma$	0.07	0.11	0.07	0.08
Batch Processor	$\eta$	0.60	0.51	0.52	0.59
	$\sigma$	0.07	0.10	0.07	0.10
	$\theta$	5.32	5.13	5.19	5.29
	$\gamma$	-47.38	-45.15	-44.74	-49.01
	$\alpha$	1.01	0.78	0.82	1.11

### 3.6 Conclusions

Several new algorithms for using GPS measurements to determine the attitude and angular rates of a spinning satellite are presented and demonstrated using both simulated orbital data and ground test data. The AR method is the best algorithm for determining spin rates. The **dr** cross-product method is the computationally simplest and fastest approach for



estimating the angular momentum axis. The batch processor, however, produces estimates of more vehicle parameters. For batch sizes of 200 samples, corresponding to 100 seconds of data for a vehicle spinning at 5 RPM, spin rates are determined to within 0.01 rpm, spin axis orientation is determined to within 0.25 deg, and phase to within 2 deg. Comparable performance could be expected for spacecraft in low earth orbit, thus satisfying the requirements of many small satellite missions.

## CHAPTER 4

### SNR AND OFF-BORESIGHT ANGLE RELATIONSHIP

#### 4.1 Introduction

This chapter explores the relationship between the signal-to-noise ratio (SNR) of a GPS measurement and the orientation of the antenna boresight vector. It begins by defining the SNR observable. This is followed by an analysis of several factors that affect this measurement. The most important is the gain pattern of the GPS receiver antenna. Other influences are the path loss, the transmitting antenna gain pattern, the transmission power, and multipath. Two methods are developed for quantifying the relationship between the SNR and the antenna boresight. The first technique uses a statistical analysis of actual data to create a mapping function between the SNR measurements and the angles between the boresight and the LOS vectors. These angles are called the off-boresight angles and are denoted by the symbol  $\alpha$ . The second creates a mapping function from an antenna gain pattern scaled to match the GPS receiver SNR values. The chapter concludes with a method for calibrating the initial alignment of the boresight vector based on SNR measurements and attitude information.

## 4.2 SNR Measurements

In addition to code and carrier phase measurements, all GPS receivers make some type of signal-to-noise ratio (SNR) measurement; primarily as a basis for checking signal integrity and maintaining signal tracking. Measurements with a very low SNR are considered unreliable and may not be used in a navigation solution. Many receivers provide the SNR or power measurement in terms of the carrier-to-noise spectral density ( $C/N_0$ ) measured in dB-Hz. In the Trimble TANS receivers it is represented in amplitude measurement units (AMU). The relationship between  $C/N_0$  and AMU's is given by [Cohen, 1992]

$$C/N_0 \text{ (dB-Hz)} = 10\log_{10} (BW \cdot \text{AMU}^2) \quad (4.1)$$

## 4.3 Receiver Antenna Gain Pattern

The relationship between the SNR of a measurement and the antenna boresight depends on the angle,  $\alpha$ , between the boresight vector and the line-of-sight to the GPS satellite, and the gain pattern of the GPS receiver antenna. Figures 4.1 through 4.4 show the gain patterns of four different GPS antennas used in this research. The plots represent the gain variations with respect to  $\alpha$  for a single azimuth angle defined as 0 deg. As demonstrated in these figures, typical GPS antennas have the highest gain along the boresight vector with decreasing gain down to 90 deg off-boresight. One exception, as shown in Figure 4.2, is for the TANS antenna which has a dip near 0 deg. As illustrated in Figure 4.5, the effect of the gain pattern causes the SNR to be highest for small  $\alpha$  angles and lowest for large angles. The azimuthal variations for all of these antennas are quite

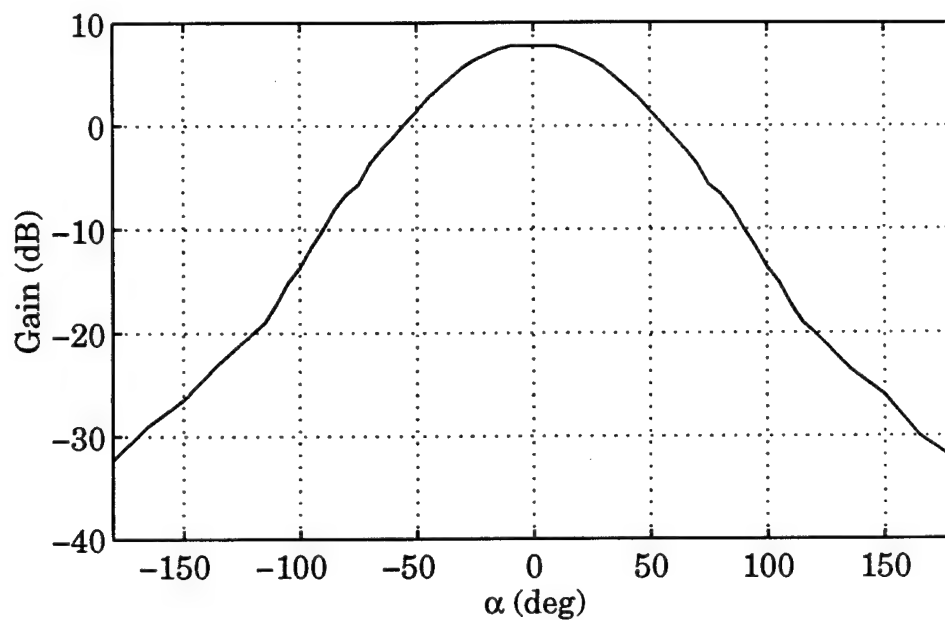


Figure 4.1. GANE choke ring antenna gain pattern. (data from Susan F. Gomez at NASA JSC)

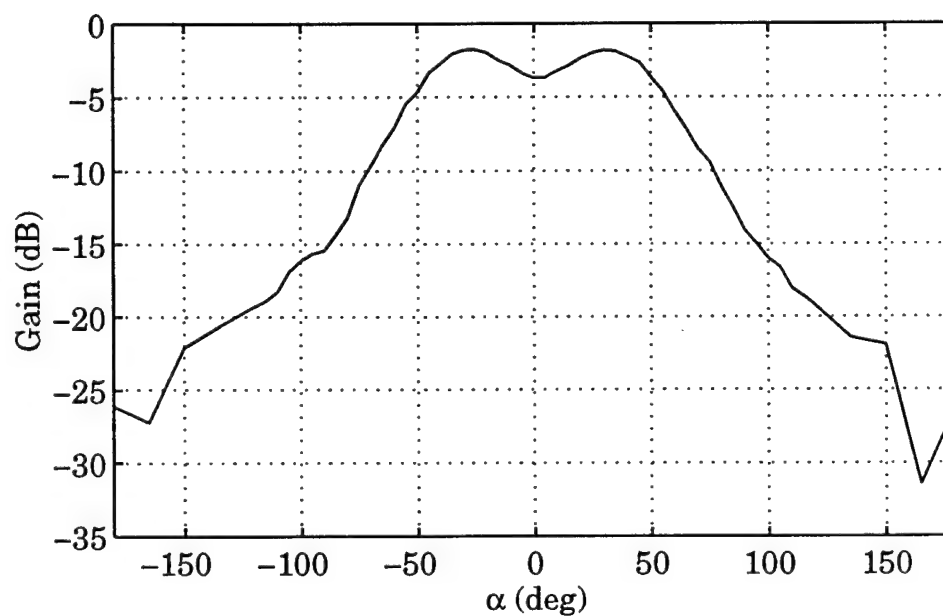


Figure 4.2. TANS patch antenna gain pattern. (data from R. Allshouse at Allied Signal Technical Services Corporation)

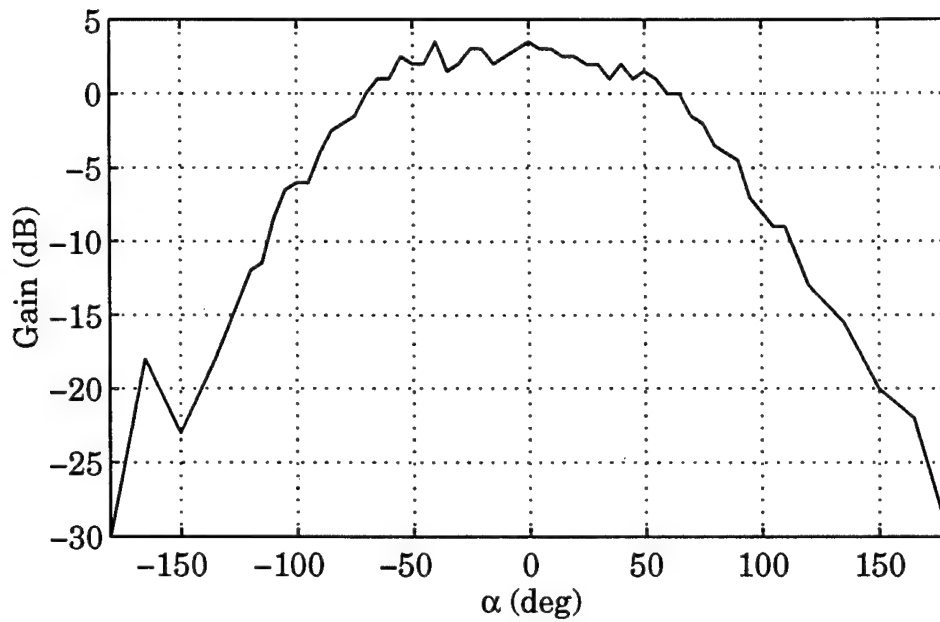


Figure 4.3. GPS/MET antenna gain pattern. (data from Charles Dunn at NASA JPL)

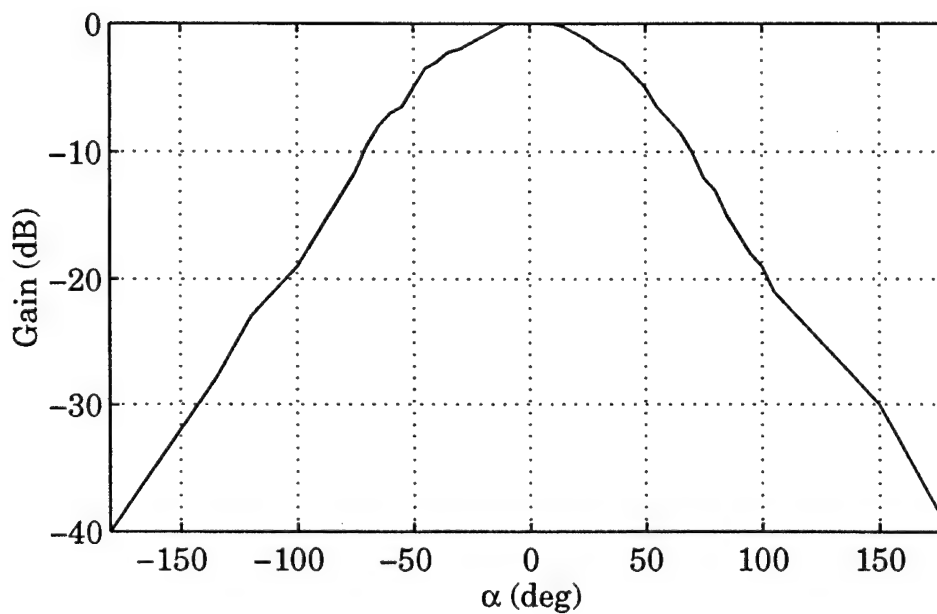


Figure 4.4. Ashtech choke ring antenna gain pattern. (data from UNAVCO)

small. For example, the TANS antenna varies less than 1 dB at small  $\alpha$ 's and less than 3 dB at  $\alpha$ 's near 90.

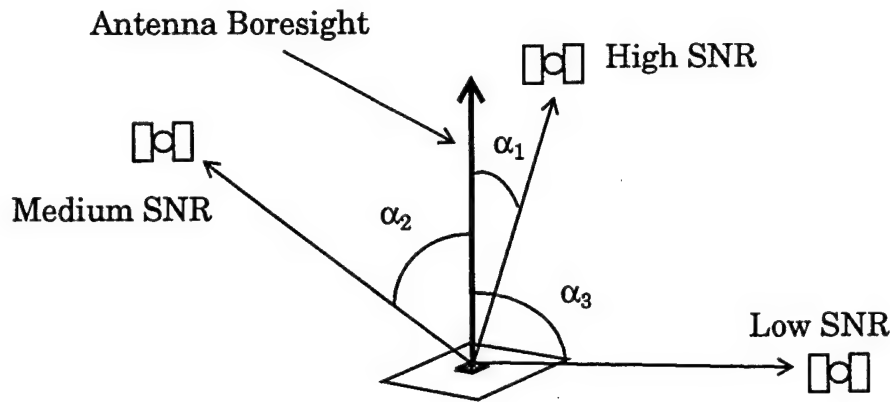


Figure 4.5. SNR and Boresight Relationship.

A method to estimate the boresight attitude, described in Chapter 5, is based upon the SNR measurement being dependent solely upon the value of  $\alpha$ . However, several other factors affect the SNR such as the GPS satellite transmit power, the antenna pattern of the GPS transmitter, space loss, atmospheric attenuation, multipath, and receiver tracking error. While a number of these are not predictable and must be treated as noise, adjustments can be made for two of the factors.

#### 4.4 Space Loss

Space loss is defined as the reduction in signal power due to propagation through free space. It is computed by

$$L_s \equiv \left( \frac{\lambda}{4\pi\rho} \right)^2, \quad (4.2)$$

where  $\lambda$  is the wavelength of the transmitted signal and  $\rho$  is the propagation distance. If a signal is transmitted with power,  $P$ , then the received power,  $P_r$  is

$$P_r = \frac{P}{L_s} = P \left( \frac{4\pi\rho}{\lambda} \right)^2. \quad (4.3)$$

In dB this equation is written as

$$P_r [\text{dBW}] = 10\log_{10} P [\text{W}] - L_s (\text{dB}), \quad (4.4)$$

where

$$L_s (\text{dB}) = 20\log_{10}\rho - 20\log_{10}\left(\frac{\lambda}{4\pi}\right). \quad (4.5)$$

The effect of space loss, as evident in Equation (4.3), is that the received power from the most distant GPS satellite is reduced more than those from the closer satellites. This is an SNR relationship that is independent of the antenna orientation. To remove this effect, the SNR values are adjusted so excessive space loss is added back into the measurement. The reference space loss is defined as the amount of signal power reduction at a reference distance,  $\rho_{\text{ref}}$ . For this research  $\rho_{\text{ref}}$  is set to 19,000 km. This value is chosen because it is approximately equal to the minimum distance between a low earth orbiting (LEO) spacecraft at an altitude of 1000 km and a GPS satellite at zenith. Using Equation (4.4) the power received,  $P_{\text{ref}}$ , at the reference distance is

$$P_{\text{ref}}[\text{dBW}] = 10\log_{10}P[\text{W}] + 20\log_{10}\left(\frac{\lambda}{4\pi}\right) - 20\log_{10}\rho_{\text{ref}}. \quad (4.6)$$

The space loss at the reference distance is 182 dB. Subtracting Equation (4.4) from (4.6) yields

$$P_{\text{ref}} - P_r = 20\log_{10}\rho_r - 20\log_{10}\rho_{\text{ref}}. \quad (4.7)$$

The resulting difference in Equation (4.7) is the adjustment that needs to be applied to each SNR measurement. If the LEO satellite is orbiting at the reference altitude or below, then every SNR adjustment increases the actual measurement. For satellites above the reference altitude, the SNR adjustment decreases the measurement for small zenith angles and increases it for large zenith ones.

The effect of the SNR adjustment is most evident when the boresight vector is pointing more towards the Earth's horizon. As illustrated in Figure 4.6, GPS satellite #2, near the horizon, is farther away than #1 which is closer to zenith. Satellite #1, however, is at a much larger  $\alpha$  with respect to the antenna boresight. While the SNR for satellite #2 should be much larger than from satellite #1 based upon the angular relationship, the greater level of space loss reduces this difference. However, knowing the transmission distances allows for the compensation of the space loss and thus, the preservation of the relationship between  $\alpha$  and SNR. When the boresight is pointing in the zenith direction, this effect is not as apparent. Measurements from GPS satellites at zenith have the highest SNR's



due to the  $\alpha$  relationship and they also have the smallest space loss. Conversely, signals from GPS satellites near the Earth's horizon have the smallest SNR's and they have the greatest space loss. As a result, the space loss effect actually strengthens the  $\alpha$  dependency.

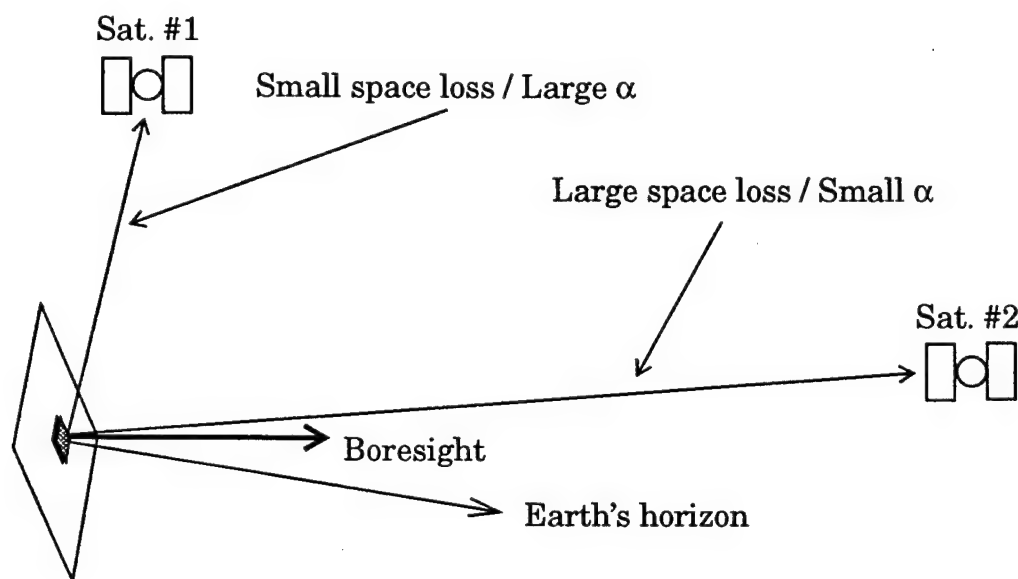


Figure 4.6. Space Loss Effects on SNR.

#### 4.5 Transmitting Power Gain Pattern Correction

The gain pattern of the transmitting antennas on the GPS satellites is designed to provide an approximately uniform signal power reaching all areas on the surface of the earth. As shown in Figure 4.7., the antenna gain is highest at the outer edge of the beam width to compensate for the greatest space loss on the ground and lower in the middle of the pattern where the space loss is lowest. The gain drops sharply beyond 15 deg off-boresight, where there are no users on the surface. For space based users, however, the space loss compensation requirements are different. As a result, the transmitting gain pattern does not exactly negate the effects of

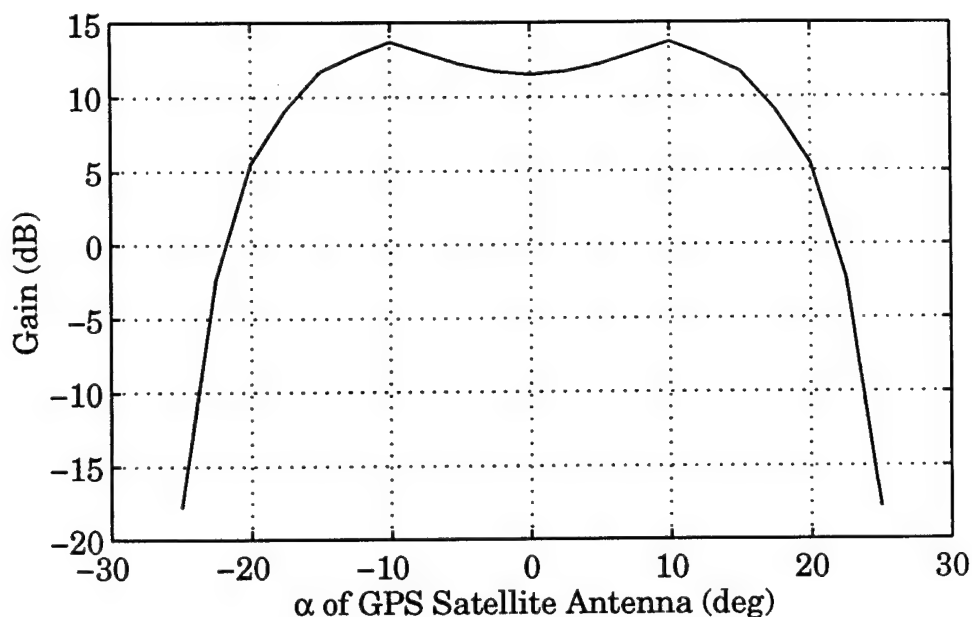


Figure 4.7. GPS satellite antenna gain pattern. [Czopek and Shollenberger, 1993]

space loss. As illustrated in Figure 4.8, the values of  $\alpha$  between the receiver antenna and the two GPS satellites are approximately equal. However, the signal from satellite #2 is transmitted at a larger angle in the GPS satellite gain pattern as compared with satellite #1. Thus, it is an additional source for the variation of received signal power that is independent of  $\alpha$ .

To find the signal variation due to the transmitting antenna gain pattern, the angle between the LOS vector,  $\hat{\mathbf{e}}$ , and the GPS satellite antenna boresight,  $\hat{\mathbf{b}}_{\text{GPS}}$ , must be computed as illustrated in Figure 4.8. The boresight of the GPS satellite antenna is approximately in the direction of the Earth's center and can be computed by

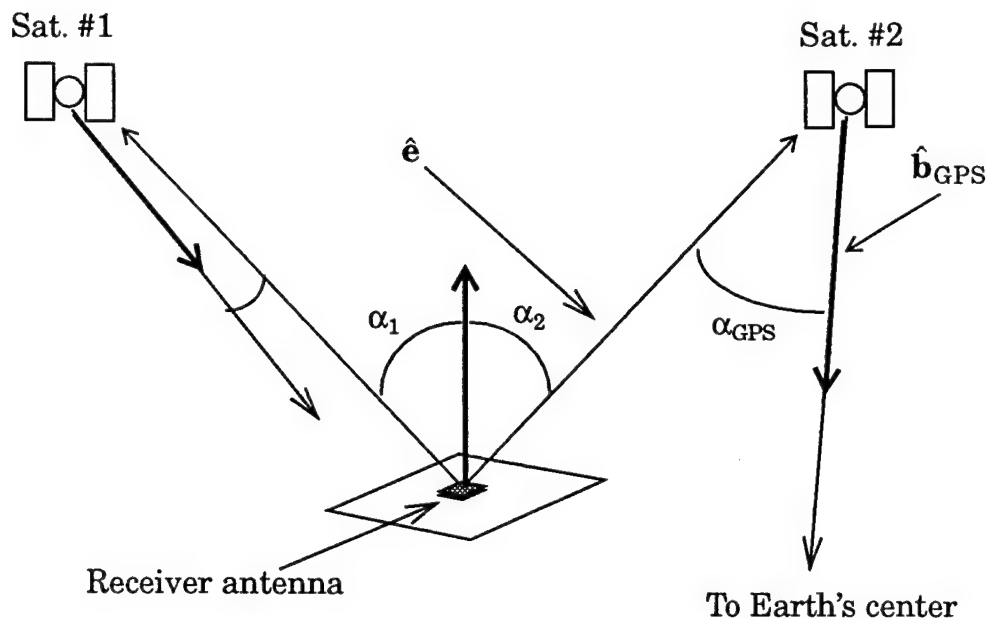


Figure 4.8. Angle in transmitting antenna pattern.

$$\hat{\mathbf{b}}_{\text{GPS}} = -\frac{\mathbf{R}_{\text{GPS}}}{|\mathbf{R}_{\text{GPS}}|}, \quad (4.8)$$

where  $\mathbf{R}_{\text{GPS}}$  is the position of the GPS satellite. The off-boresight angle of the receiver with respect to the GPS satellite boresight is

$$\alpha_{\text{GPS}} = \cos^{-1}(-\hat{\mathbf{e}} \cdot \hat{\mathbf{b}}_{\text{GPS}}). \quad (4.9)$$

Figure 4.9 shows an example of the power level adjustments made for a LEO satellite. The satellite is in a circular equatorial orbit at an altitude of 1000 km. GPS satellite #32 (PRN #1) is being tracked. The plot covers a period from when the GPS satellite first enters the field of view of the antenna to when it exits. At the start of the track, the LEO and GPS satellites are farthest apart. They approach each other until some minimum distance is reached and then grow steadily farther apart. The thin

line is for the SNR adjustment for the space loss. As is expected, the compensation is the highest at the beginning and end of the tracking. The dot and dash line is for the pattern correction adjustment. When the GPS satellite is the closest, the line-of-sight is near the center of the pattern. As a result, the adjustment is close to zero. At two points in the track, the angle between the LOS vector and the GPS satellite antenna boresight vector reaches about 10 deg. These points correspond to the greatest gains in Figure 4.7 and therefore, are the points where the SNR is adjusted downward the most. The thick line is the combined SNR adjustment. The maximum increase in SNR is around 2.5 AMU and the maximum decrease is about -2 AMU. These values are about 5 percent of a typical total SNR measurement. In Figure 4.10 the combined adjustment is shown as a function of the zenith angle between the LEO satellite and the GPS satellite. The greatest increases occur between 65 and 90 deg. The largest decreases are between 20 and 60 degrees.

#### 4.6 Multipath Effects

Multipath is the effect caused when an electromagnetic signal reaches an antenna by an indirect path through one or more reflections as well as through the direct path [Comp, 1996]. Multipath causes the SNR measurements to have periodic fluctuations. The frequencies of the fluctuations are dependent upon the distances between the antenna and the reflectors and the satellite motion. Figure 4.11 shows an example of how multipath influences the SNR measurement over time. The data is taken with a ground based antenna from a single GPS satellite. The elevation angle between the GPS satellite and the antenna is increasing over the

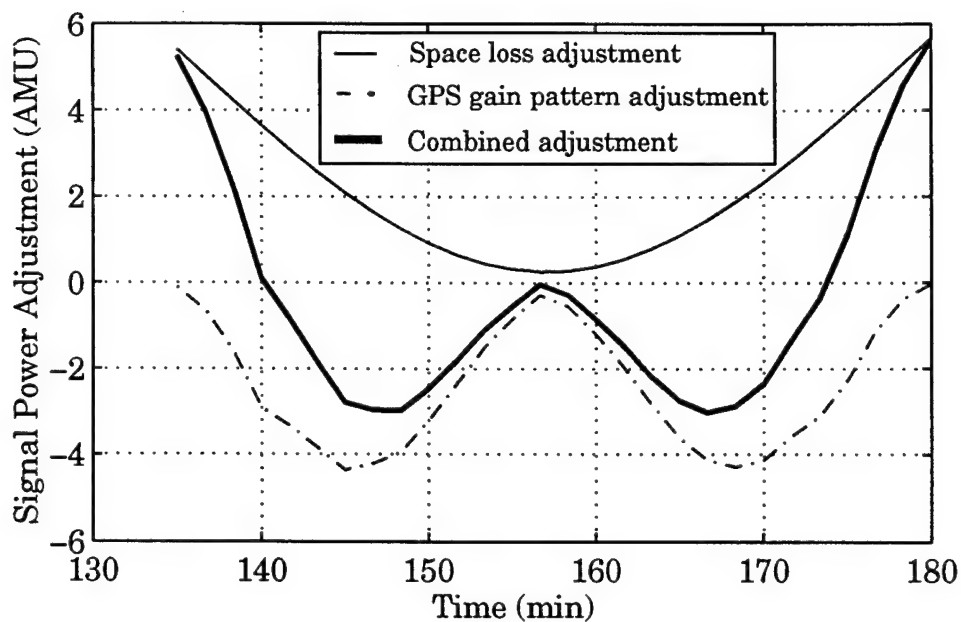


Figure 4.9. Example of SNR adjustments.

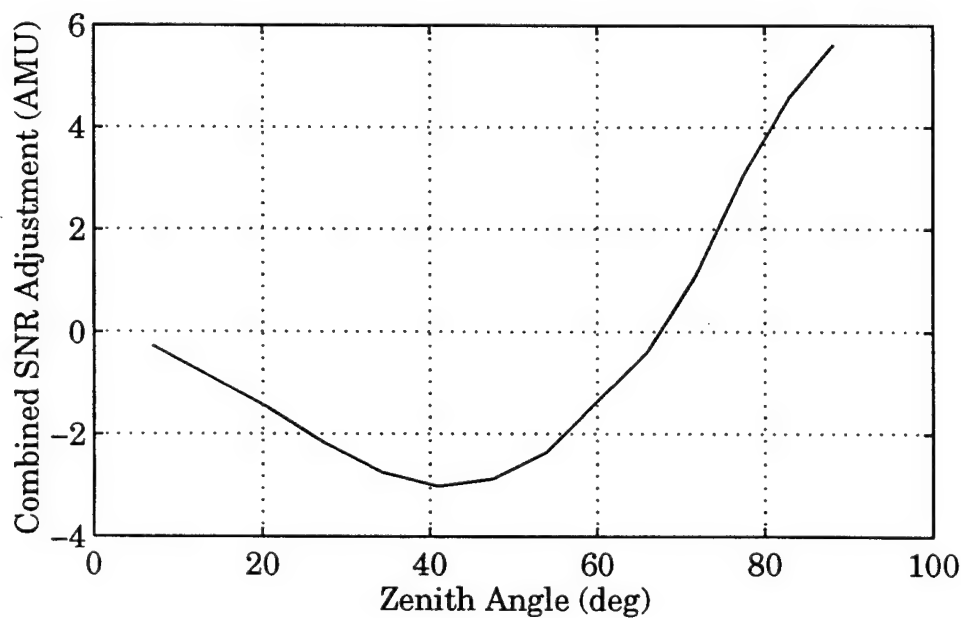


Figure 4.10. SNR adjustments vs. the angle between satellites.

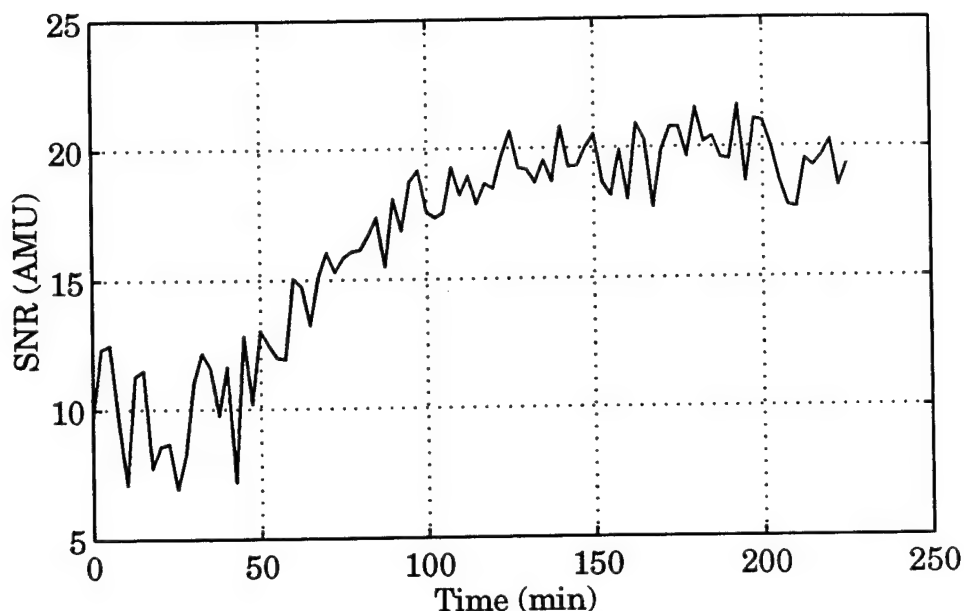


Figure 4.11. The effect of multipath on SNR.

span of the data. The SNR increases because of the decrease in  $\alpha$ . However, there are also rapid fluctuations due to multipath from distant objects. Comp [Comp, 1996] develops methods for estimating multipath contributions for the purpose of removing phase variations due to its effect [Axelrad et al., 1996]. The multipath effect tends to be a strong function of the LOS. While it is possible to construct a correction map based on extensive data sets, the technique is computationally intensive and is not necessary for the level of accuracy achievable in this work. As a result, multipath is not an effect on SNR that can be removed in the same manner as for the space loss and pattern correction. Instead, it is treated as measurement noise.

#### 4.7 Variations Due to Individual GPS Satellites

The GPS satellites are designed so that the received signal power on the surface of the Earth does not exceed -153.0 dBw. The signal power is generally highest when the satellite is new and drops off as the satellite approaches its end of life. Over the lifetime of a satellite, the power loss is expected to be less than 7.0 dB [Ward, P., 1996]. Several variables affect the power output when compared among satellites. Each satellite is in a different stage of their design lifetime. Each satellite receives a different level of solar flux and experiences different environmental conditions. There are also variations among the physical characteristics of each satellite. The most evident physical difference is caused by having three different satellite models currently in operation.

These power variations do not alter the  $\alpha$  versus SNR dependence like the space loss and transmitting gain pattern effects. They are independent of the receiver type, position, and orientation. Their influence is apparent on a satellite by satellite basis. For these variations to be significant, a plot of  $\alpha$  versus SNR for an individual satellite needs to show a bias when compared to a plot of  $\alpha$  versus SNR for the entire constellation. In other words, over the entire range of SNR values, the average  $\alpha$  measurement for each SNR is either consistently higher or consistently lower than the average for the entire constellation.

Data from the CRISTA-SPAS satellite, discussed more thoroughly in Chapter 6, does not demonstrate a significant bias. This set is chosen because there is sufficient data covering almost every GPS satellite. Figures 4.12 through 4.15 show four examples of  $\alpha$  versus SNR covering both block II and IIA GPS satellites and a range of satellite lifetimes. While it

is evident that the average  $\alpha$  values from the individual satellite are different than the constellation average, the differences are not biased towards either higher or lower values. The individual averages fluctuate about the constellation average, remaining within the  $1\sigma$  bounds.

## 4.8 SNR to $\alpha$ Mapping Function

The key to a reliable attitude solution is a valid mapping of SNR to  $\alpha$ . As is discussed in Chapter 6 for some actual GPS data, the true relationship between SNR and  $\alpha$ , is far from one-to-one. The ideal relationship presented in section 4.3 does not accurately reflect the variations shown in real data. An adequate mapping function, however, can still be established. In this section two basic approaches to create this function are investigated- the first creates a mapping based on a calibration data set and the second uses measured antenna gain patterns. The latter is similar to suggestions in [Hashida and Unwin, 1993] and [Serrano, et al., 1995].

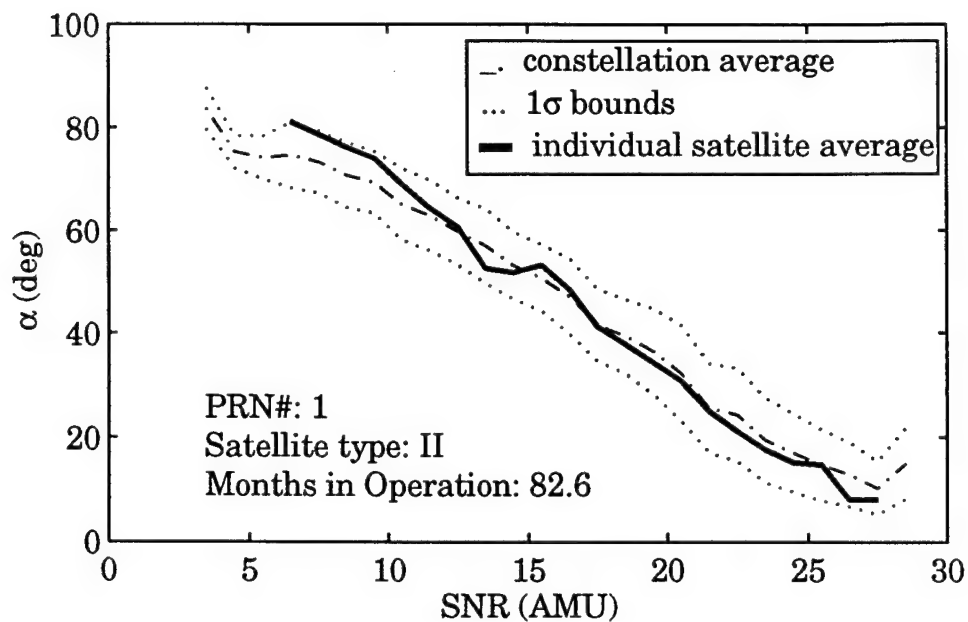
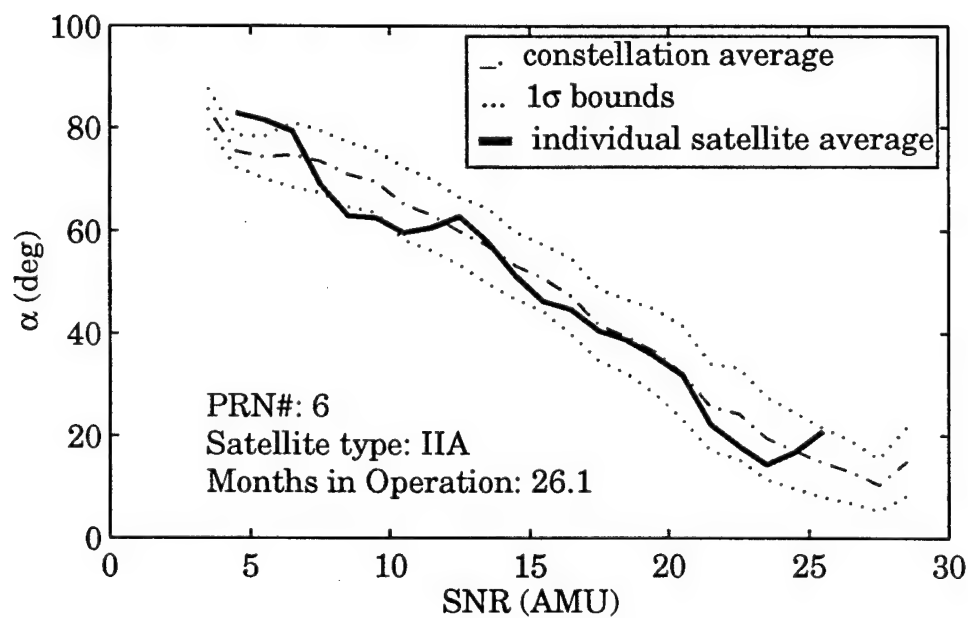
### 4.8.1 Calibration Based Mapping Function

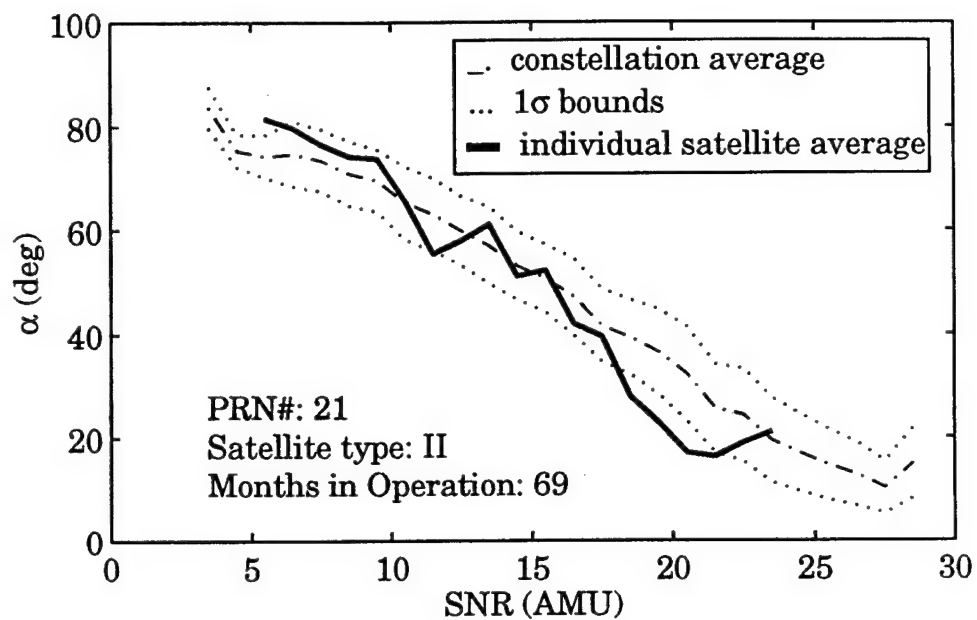
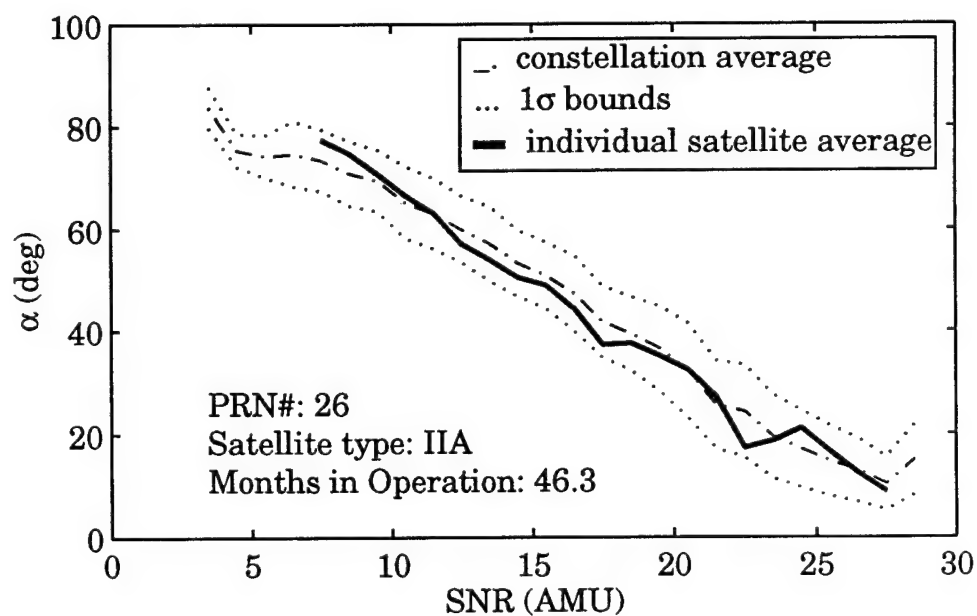
A calibration data set consists of a large set of LOS vectors, measured SNR's, and accurately measured  $\alpha$ 's. A sufficiently large set is one that includes the full range of possible viewing angles to each GPS satellite. It requires the antenna to be in a known orientation for accurate computation of  $\alpha$ . It should be stressed that since the SNR to  $\alpha$  relationship is not one-to-one, each SNR has a range of corresponding  $\alpha$  values associated with it.

Given an appropriate calibration data set, the mapping function is generated as follows:

- 1) divide the SNR values into discrete bins;



Figure 4.12.  $\alpha$  versus SNR for PRN# 1.Figure 4.13.  $\alpha$  versus SNR for PRN# 6.

Figure 4.14.  $\alpha$  versus SNR for PRN# 21.Figure 4.15.  $\alpha$  versus SNR for PRN# 26.

- 2) collect the accurate  $\alpha$ 's corresponding to the SNR values in each bin;
- 3) compute the mean  $\alpha$  and standard deviation for each bin.

In applying the mapping to subsequent data, the mean  $\alpha$  is the best estimate for the bin. In other words, it is the value of  $\alpha$  for all SNR's in the bin. The standard deviation of the  $\alpha$ 's determines the appropriate weighting. To quantify the overall quality of the mapping function the value  $\Delta\rho$  is computed. It is defined as the mean of the residuals between the data points and a 5th order polynomial fit to the points.

Calibration data sets may be established on the ground or in orbit. In this research, calibration from the actual data being processed for estimation is used to quantify the best possible performance. This is called the reference result.

The best practical calibration source is from actual orbit data from the on-board GPS receiver. During times when the attitude is known from an external reference, the  $\alpha$ 's are computed and SNR data are recorded. Using this information, a mapping function is created. This method has the advantage that the mapping function is based on data taken under the same conditions as the present data. The same antenna is used, the noise in the receiver is similar, the line biases are identical, and the multipath environment is the same. Ideally, the calibration data include measurements taken from all visible GPS satellites throughout the orbits. The major disadvantage is that SNR-based attitude estimation is not available immediately. One scenario where this might be useful is if the nominal attitude reference sensor fails, a GPS receiver used for positioning information could then be employed for attitude determination. It might also

be used for faster integer ambiguity resolution in a GPS phase-based attitude algorithm.

The second calibration source is from data collected prior to the launch of the satellite. This is obtained from either ground tests or from a previous satellite mission. A major advantage of this method is that the mapping function is available for immediate estimation. Unlike on orbit calibration, however, several factors could be significantly different between the calibration data and the actual measurements. If data is used from a previous satellite mission, the multipath and noise environment could be significantly different. Also, the visibility conditions might not be the same. On the ground, data collection would most likely occur on a spacecraft mock-up. Multipath from the ground or other surroundings would be added resulting in a different SNR behavior. The ground receiver would see a different set of GPS satellites and it would be moving much slower in relation to them. Finally, the environmental conditions of actual receiver operation would be different.

The SNR to  $\alpha$  mapping can be readily updated whenever SNR data and an external reference are available. This could be important for a satellite that uses a number of distinct orientations over its mission lifetime.

#### **4.8.2 Gain Pattern Based Mapping Function**

An alternative method for generating a mapping function, which does not depend upon a calibration data set, involves using a gain pattern of the antenna. Such patterns are routinely measured in an anechoic chamber. The gain pattern values must be scaled by the nominal received power in order to match the actual output values of the GPS receiver. For

example, the top graph in Figure 4.16 shows the measured gain pattern in dB of a patch antenna. The bottom graph shows the measured gain pattern scaled to match the SNR in AMU's of a TANS Vector receiver. The conversion equation is

$$\text{AMU} = G_{\text{antenna}} \sqrt{P_0}, \quad (4.10)$$

where  $P_0$  is the arriving signal strength.

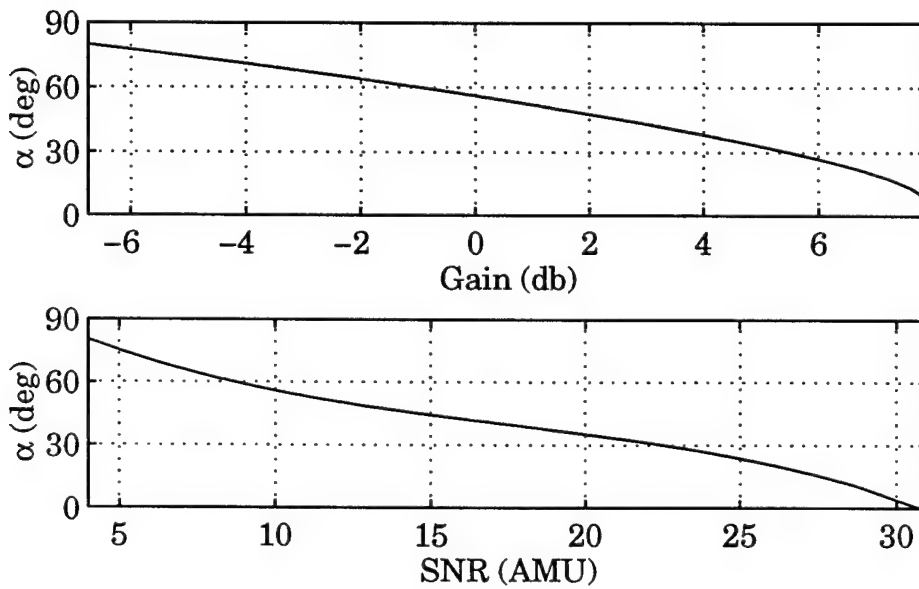


Figure 4.16. Scaling of measured gain pattern values to receiver output values.

The scaling factors may be derived by monitoring the SNR output of the receiver. It is assumed that over a 20 minute period one or more of the GPS satellites has a maximum  $\alpha$  of 80 to 90 deg. These should correspond to the lowest measured SNR's. Similarly, one or more GPS satellites should be within 5 deg of the boresight corresponding to the highest SNR's. For example, in the GANE data set, discussed thoroughly in Chapter 6, the

highest  $\alpha$  in a typical 20 minutes segment of data is 80 deg. This measurement has a SNR of 4.5 AMU. For the entire data set, about 1% of the SNR values are below 4.5. The smallest  $\alpha$  is 4 deg. This measurement has an SNR of 29 AMU. About 1% of the SNR values are above this number. Assuming that these extreme values from the sample 20 minutes of data are good representatives of any block of data, they are used to create scaling factors for the gain pattern.

The scaling factors,  $\kappa$ , are computed from the ratio

$$\kappa = \frac{\kappa_g}{\kappa_r}, \quad (4.11)$$

where  $\kappa_r$  is the SNR in AMU's from the receiver at one of the extreme angles and  $\kappa_g$  is the corresponding pattern gain in dB at this angle.  $\kappa_r$  is computed from the mean of the expected range of SNR's for this angle. For example, in the GANE data the  $1\sigma$  variation in the SNR's corresponding to 80 deg cover the lowest 2% of the recorded SNR measurements. As a result,  $\kappa_r$  is computed from the mean of this range. As shown in Figure 4.16, the lower gain pattern values, plotted in the top graph, are scaled by the value of  $\kappa$  for the lowest SNR's, while the higher gain pattern values are scaled by  $\kappa$  for the highest SNR's. The mid range values are scaled by an average of these two factors.

The greatest advantage to this method is that the mapping function is easy to generate and is available for immediate use on orbit. However, the environment under which the SNR mapping is generated is the most different, does not include multipath, and can not account for GPS satellite variations. It also may not work well for satellites in certain orientations

for which the entire  $\alpha$  range is not covered in a short time period. The scaling factors, in this case, can be easily adjusted as more data becomes available.

### 4.8.3 Mapping Function Summary

Of all the methods to generate a mapping function, on-orbit calibration is the best choice in terms of accuracy. The conditions under which the function is computed remain consistent throughout the mission. Therefore, the mapping function data will correspond very closely to the behavior of the measurements used for the actual axis estimation.

After generating this function by either the data calibration or gain pattern methods, attitude estimation can occur. During each estimation epoch, one SNR value is measured for each GPS satellite in view. Each of the corresponding bin numbers are found. In those bins the associated  $\alpha$  and weight are located. Chapter 5 describes the process by which the angles, measurement weights, and LOS vectors are used. The result is an instantaneous estimate of the antenna boresight direction.

## 4.9 Estimation of the Boresight Alignment

To further refine the mapping function, an auxiliary calibration step is required to determine the offset between the nominal body orientation of the boresight vector and its true orientation. The nominal boresight vector in the body frame can be defined from a priori knowledge of how the antenna is mounted on the spacecraft structure. For example, suppose the spacecraft body frame is defined so that one face is called the  $x^B y^B$ -plane. If a GPS patch antenna is mounted with its plane parallel to the  $x^B y^B$ -plane, then the boresight vector is along the  $z^B$ -axis. If the patch antenna is not

perfectly parallel to this plane, then there is some constant misalignment as shown in Figure 4.17. Another possibility is if the gain pattern of the antenna is not maximum along the nominal boresight axis. The offset must be determined from a collection of GPS data and a knowledge of the true attitude.

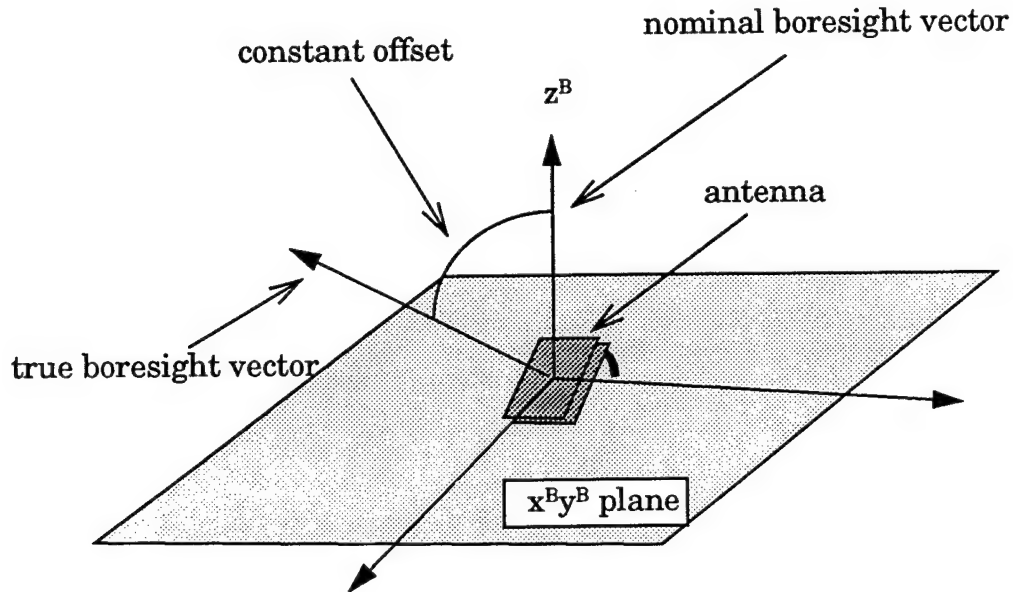


Figure 4.17. Boresight alignment.

As discussed in section 4.8.1, construction of a calibration data based mapping function requires knowledge of the true orientation of the antenna boresight vector and the LOS vectors. By knowing the true attitude of the spacecraft with respect to some local system, the LOS vectors in the spacecraft frame are computed by using the rotation

$$\hat{\mathbf{e}}_i^B = {}^B C^L \hat{\mathbf{e}}_i^L. \quad (4.12)$$

Each  $\alpha_i$  in the calibration set is then determined from the relationship



$$(\hat{\mathbf{e}}_i^B)^T \hat{\mathbf{n}}^B = \cos \alpha_i. \quad (4.13)$$

The batch of  $\alpha_i$  values is used to estimate the calibration function,  $F$ , such that

$$F(\text{SNR}_i) \approx \cos \alpha_i. \quad (4.14)$$

However, if the true orientation of the antenna in the body frame,  $\hat{\mathbf{n}}^B$ , is not available due to some unknown misalignment, then the true values of  $\alpha$  cannot be determined and thus,  $F$ , cannot be estimated.

While  $F$  is unknown, other information is available based on the assumption that Equation (4.14) is valid. Every LOS vector satisfying the conditions that

$$\hat{\mathbf{e}}_i \neq \hat{\mathbf{e}}_j \quad (4.15)$$

and

$$\text{SNR}_i \approx \text{SNR}_j, \quad (4.16)$$

implies that

$$\alpha_i \approx \alpha_j \quad (4.17)$$

This leads to the relationship that

$$F(\text{SNR}_i) \approx F(\text{SNR}_j). \quad (4.18)$$

Combining Equations (4.13), (4.14), and (4.18), an equation for  $\hat{\mathbf{n}}^B$ , involving the difference of two LOS vectors associated with approximately equal SNR measurements is

$$\left[ (\hat{\mathbf{e}}_i^B) - (\hat{\mathbf{e}}_j^B)^T \right]^T \hat{\mathbf{n}}^B \approx 0. \quad (4.19)$$

For any pair of LOS vectors, there are an infinite number of possible solutions for  $\hat{\mathbf{n}}^B$ . However, the actual solution must simultaneously satisfy Equation (4.19) for all pairs of LOS vectors meeting the conditions set in Equations (4.14) and (4.15). This leads to a procedure to estimate  $\hat{\mathbf{n}}^B$ .

The steps are as follows:

- 1) group all of the SNR measurements into discrete bins;
- 2) group the LOS vectors according to the bins of their corresponding SNR measurements;
- 3) for each bin,  $k$ , form the matrix

$$\mathbf{G}_k = \begin{bmatrix} (\hat{\mathbf{e}}_2^B)^T - (\hat{\mathbf{e}}_1^B)^T \\ (\hat{\mathbf{e}}_3^B)^T - (\hat{\mathbf{e}}_1^B)^T \\ \vdots \\ (\hat{\mathbf{e}}_N^B)^T - (\hat{\mathbf{e}}_1^B)^T \end{bmatrix}, \quad (4.20)$$

where  $N$  is the number of measurements in the bin;

- 4) combine Equations (4.19) and (4.20) to yield

$$\begin{bmatrix} \mathbf{G}_1 \\ \mathbf{G}_2 \\ \vdots \\ \mathbf{G}_M \end{bmatrix} \hat{\mathbf{n}}^B = \mathcal{G} \hat{\mathbf{n}}^B \approx 0, \quad (4.21)$$

where  $M$  is the number of SNR bins;

- 5) compute  $\hat{\mathbf{n}}^B$ .

In the ideal case,  $\hat{\mathbf{n}}^B$  spans the null space of  $\mathcal{G}$ , however, for real data it is the vector that produces the smallest norm when  $\mathcal{G}$  is multiplied by it [Press, et al., 1992].  $\hat{\mathbf{n}}^B$  can be computed by first performing a singular value decomposition on  $\mathcal{G}$  to express this matrix as a product of a column-orthogonal matrix,  $\mathbf{U}$ , a diagonal matrix,  $\mathbf{S}$ , and an orthogonal matrix,  $\mathbf{V}$ , such that

$$\mathcal{G} = \mathbf{U}\mathbf{S}\mathbf{V}^T. \quad (4.22)$$

The diagonals of  $\mathbf{S}$  are the singular values and are equal to the norms of the columns of  $\mathcal{G}\mathbf{V}$ . If  $\mathcal{G}$  is truly singular, then one of the singular values is exactly zero and  $\hat{\mathbf{n}}^B$  is the corresponding column of  $\mathbf{V}$ . Because of the approximations involved in generating  $\mathcal{G}$ , there is no singular value equal to zero. Therefore,  $\hat{\mathbf{n}}^B$  is approximated by the column of  $\mathbf{V}$  associated with the smallest one. To reliably estimate  $\hat{\mathbf{n}}^B$  a sufficiently large set of SNR and LOS measurements is required as well as an accurate estimate of the vehicle attitude over the duration of the data. For this research, the entire span of data is used for each set. Further work is necessary to determine the set size requirements for a given level of accuracy.

It is interesting to note that in the case of a constant attitude vehicle, the solution to Equation (4.21) is an estimation of the boresight vector in the local frame. By defining the body frame to be aligned with the local frame, the boresight vector alignment in the body frame is also its orientation with respect to the known local system. However, multiple LOS vectors for each SNR bin are required for Equation (4.21) to be solvable. This is highly unlikely for any single measurement epoch. Therefore, Equation (4.21) can only be solved over a batch of measurement times. When the

vehicle attitude is not constant, the solution for Equation (4.21) can only be used to estimate the boresight vector in the local system at any single time. As previously stated, one measurement time is not sufficient for this computation. Over a batch of measurement epochs, the attitude is changing and as a result, the alignment of the vehicle body with respect to the local system is changing. However, the alignment between the boresight vector in the body system and any other axis in the body frame is constant. Therefore, as shown in the procedure outlined in the last paragraph, the solution for Equation (4.21) can always be used to estimate this offset.

If truth attitude is not available and the mapping function is created from the antenna gain pattern, then a mechanical drawing of the antenna mounted on the spacecraft is necessary. An estimate of the boresight vector is possible without the drawing. However, the relationship between the antenna orientation and the orientation of any instrument on the vehicle remains unknown.

#### 4.10 Conclusions

The relationship between the SNR measurement from a GPS receiver and the orientation of the antenna boresight vector is based primarily on the gain pattern of the antenna. LOS vectors to GPS satellites that are at small angles with respect to the antenna boresight correspond to the highest SNR measurements. LOS vectors that make large angles with the boresight vector correspond to the lowest SNR measurements. Other factors, such as space loss and the transmitting antenna gain pattern contribute to this relationship in a manner that must be compensated.

Power fluctuations from individual GPS satellites are not significant from the current constellation. Multipath is treated as measurement noise.

Because this relationship for actual data is unknown and not one-to-one, a mapping function is created. The technique used in this research is based upon using either a calibration data set or an antenna gain pattern. The calibration data set requires SNR data from an antenna in a known orientation. The gain pattern approach requires just SNR data. Before creating this mapping function, the true boresight alignment in the body system has to be computed through an initial calibration step. After this is accomplished, the estimation of the boresight vector can proceed.

In the next chapter, a method is presented that uses the mapping functions to estimate the boresight vector of an antenna. GPS data from several sources are examined in Chapter 6. The data are processed to generate mapping functions. Chapter 7 presents the actual estimation results.

## CHAPTER 5

### MAXIMUM LIKELIHOOD BASED ESTIMATION ALGORITHMS

#### 5.1 Introduction

The previous chapter details the relationship between the SNR measurements and  $\alpha$ , defined to be the angle between the GPS LOS vectors and the orientation of the antenna boresight vector. Procedures are established to create a mapping function between them. In the first part of this chapter a method is formulated that uses  $\alpha$  and SNR as observables in a maximum likelihood estimate (MLE) of the boresight vector. First the geometry of the problem is detailed. Next, the mathematical basis of the technique and its application to the SNR measurements are presented. This is followed by a derivation of the estimation error covariance.

The second part of this chapter outlines the application of this single axis approach to specific attitude estimation problems. Knowledge of a single boresight vector is adequate when only one axis is required, such as for the spinning satellite case in which the orientation of the angular momentum axis is needed. For this case, the necessary computations under various antenna mounting positions are investigated. In the case of a three-axis stabilized satellite a minimum of two non-colinear axis are required. Unfortunately, there is no actual satellite data available for either of these two cases. Performance is only estimated for the single-axis results.

## 5.2 Estimation Geometry

A standard method for estimating the orientation of a single spacecraft axis in a given reference frame involves two angle measurements between the unknown axis,  $\hat{\mathbf{n}}$ , and two known vectors,  $\hat{\mathbf{e}}_1$  and  $\hat{\mathbf{e}}_2$ , referred to in this research as the reference vectors. As shown in Figure 5.1, each angle measurement constrains the solution to a circle on the surface of a unit sphere, centered about the known reference vector. The radius of the circle is a function of the angle measurement. The intersections of the circles determine the only possible values for  $\hat{\mathbf{n}}$ . With perfect instruments, the addition of a third measurement removes the ambiguity. Any additional measurements also provide intersections at the same solution point. This is provided that the additional reference vectors are not parallel to the others.

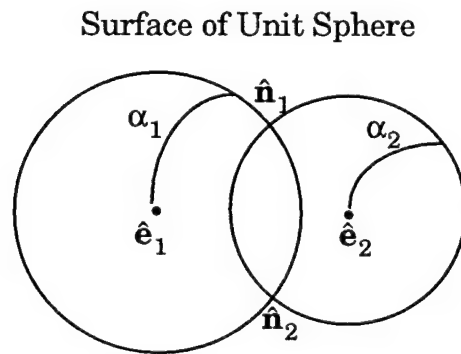


Figure 5.1. Single axis estimation from two angle measurements.

In many small satellite missions, the reference vectors and angle measurements are taken from an Earth horizon sensor and sun sensors. The Earth lines are determined from the position of the spacecraft in an Earth centered frame. Because the Earth is very close to the spacecraft,

light reflected off the planet is not considered to be from a point source. Instead, a horizon sensor is used. The field-of-view (FOV) for this sensor sweeps through space to detect two rapid changes in light intensity between space and the Earth, one change occurring when the FOV enters the atmosphere and the other when it leaves. Knowing the scanning speed of the instrument, the time between horizon detections, and the size of the Earth, the angle between the Earth line and the plane of the sensors is computed. The sun lines are accurately determined from the known position of the spacecraft with respect to the center of the Earth and from the known position of the Earth with respect to the sun. Because the sun is far away from the spacecraft, the solar rays reaching the sensor are considered to be parallel to the sun line. The sun sensor measures the angle of these incoming light rays with respect to the sensor plane.

GPS also may be used in the same manner by mapping SNR measurements to the angle  $\alpha$  formed between the antenna boresight and each GPS LOS vector,  $\hat{e}$ . In this case, the antenna boresight is the unknown axis to be determined and the LOS vectors provide the reference vectors in an appropriate reference frame. This is diagramed in Figure 5.2. LOS vectors are determined based upon the known positions of the GPS satellites and the user spacecraft carrying a GPS receiver and antenna. Like the sun and Earth lines, the LOS vectors are assumed to be highly accurate. The position computations, however, do not need to be very accurate; in fact LEO position errors of up to 350 km only contribute as much as 1 deg error in the LOS computation.

Assuming a perfect relationship between SNR and  $\alpha$ , a single SNR measurement from one satellite gives the angle between the unknown



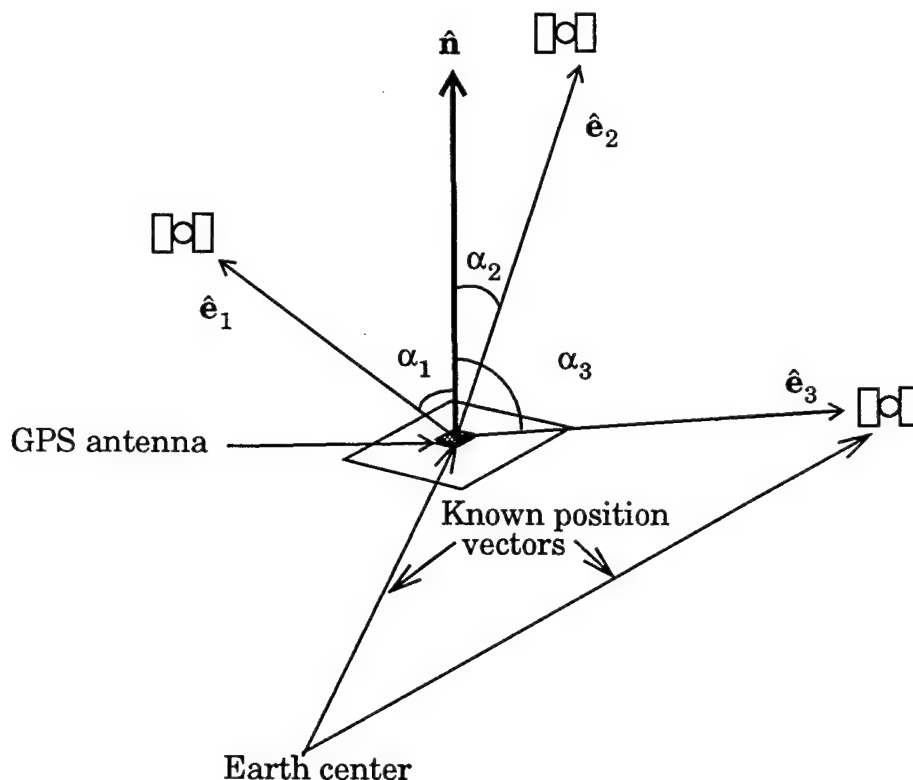


Figure 5.2. Estimation geometry.

boresight vector and the LOS vector. In three dimensional space, this is a cone of possible boresight vectors centered on the LOS vector. On the unit sphere, unit vectors are represented by their x, y, and z components plotted on the surface. For the case of one LOS vector and one SNR measurement, the LOS vector is a single point on the surface of the sphere while the possible boresight vectors, corresponding to the value  $\alpha$  from the SNR mapping function, lie in a circle about this point. The radius of the circle is a function of  $\alpha$ . Figure 5.3 illustrates both the three dimensional view and the unit sphere projection.

An additional SNR measurement from a second satellite narrows the possible locations of the boresight vector to two positions. As previ-

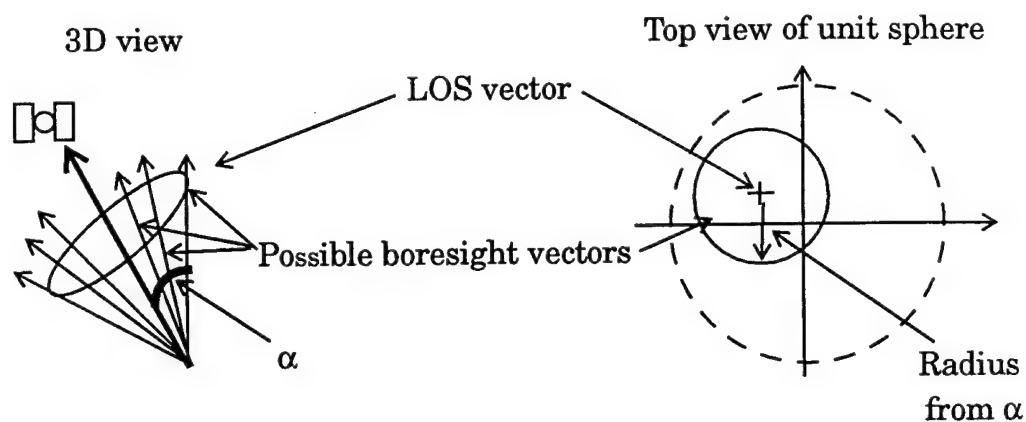


Figure 5.3. Boresight Information from a Single GPS Satellite.

ously stated, the individual  $\alpha$  values mapped from each of the SNR measurements restrict the boresight location to circles about the LOS vectors. The true boresight location must lie on both of these circles. This condition occurs at the intersections between the two LOS centered circles or in the 3-D representation, between the two LOS centered cones, as shown in Figure 5.4.

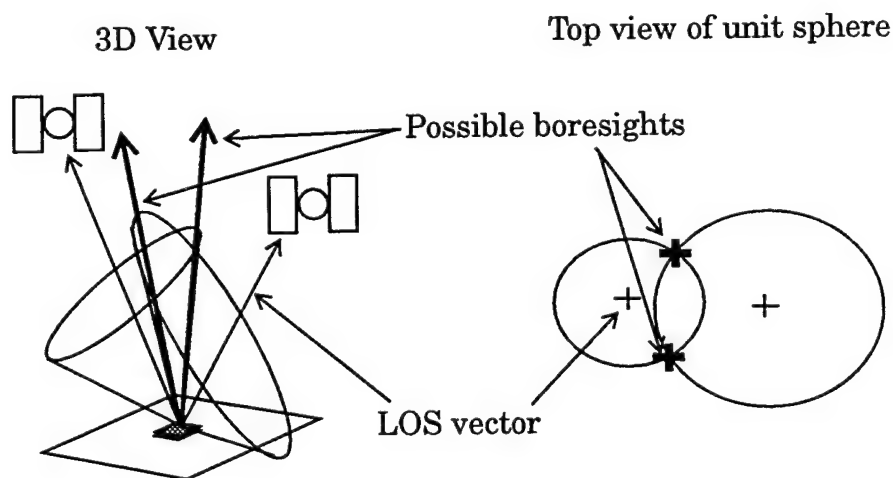


Figure 5.4. Multiple SNR and LOS vector geometry.

Because of the large uncertainties involved in the actual mapping functions, the GPS case is better illustrated using rings instead of circles. The intersection of two rings limits the possible boresight locations to two large areas. One advantage of GPS is that there are typically as many as five or more GPS satellites in view at a time. Each GPS satellite provides another measurement and thus, another ring of possible locations for  $\hat{\mathbf{n}}$  on the unit sphere. As shown in Figure 5.5, the addition of more rings begins to reduce the large uncertainty regions. With three or more measurements an optimal estimate of  $\hat{\mathbf{n}}$  can be determined based upon all the information available. The optimal choice is found using a maximum likelihood estimate (MLE).

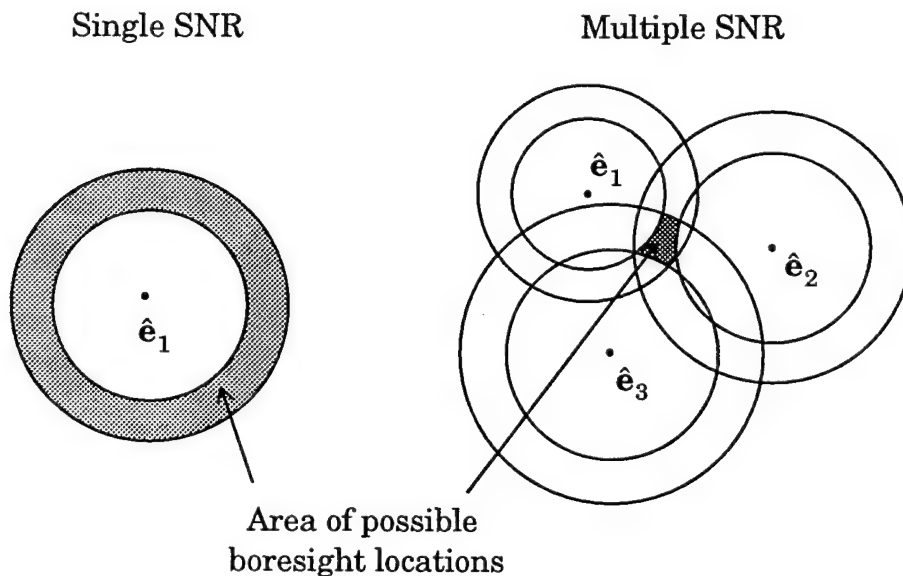


Figure 5.5. Geometry of GPS measurements.

### 5.3 Maximum Likelihood Estimates

For given a set of observed values  $x_1, x_2, \dots, x_n$  taken from a set of random variables,  $X_1, X_2, \dots, X_n$  and a set of unknown parameters  $\beta_1, \beta_2, \dots, \beta_m$ , the maximum likelihood estimates for the parameters are the values that maximize the joint probability density function [Devore, 1990]

$$f(x_1, x_2, \dots, x_n; \beta_1, \beta_2, \dots, \beta_m). \quad (5.1)$$

The MLE is desirable because it is consistent, asymptotically unbiased, asymptotically normally distributed and asymptotically efficient. In addition, it is the minimum variance unbiased linear estimate [Maybeck, 1994]. For the GPS-based single axis estimation case, the observed values are the cosines of  $\alpha$  and the parameter is the boresight vector. Therefore, the problem is to find the unit vector that maximizes

$$f(\cos\alpha_1, \cos\alpha_2, \dots, \cos\alpha_n; \hat{\mathbf{n}}). \quad (5.2)$$

The weighted least squares solution is one unbiased and minimum variance estimator that is a potential MLE for (5.2). The boresight vector is the solution that minimizes the cost function

$$J(\hat{\mathbf{n}}) = \frac{1}{2} \sum_{k=1}^N a_k |\cos\alpha_k - (\hat{\mathbf{e}}_k)^T \hat{\mathbf{n}}|^2, \quad (5.3)$$

where  $a_k$  are the measurement weights. Shuster [Shuster, 1989],[Shuster, 1994] shows that the minimization of (5.3) is the MLE for  $\hat{\mathbf{n}}$  if the probability density function for the measurements,  $\cos\alpha_k$ , are axially symmetric about the  $\hat{\mathbf{n}}$  and if the weights are chosen correctly. The correct weights are determined to be

$$a_k = \frac{1}{\sigma_k^2}, \quad (5.4)$$

where  $\sigma_k^2$  are the variances of the density functions.

#### 5.4 Shuster's Method

In this research the axially symmetric distribution assumption is accurate for the data used as will be proven in Chapter 6. Therefore, the cost function to be minimized is given by

$$J(\hat{\mathbf{n}}) = \frac{1}{2} \sum_{k=1}^N \frac{1}{\sigma_k^2} \left| \cos \alpha_k - (\hat{\mathbf{e}}_k)^T \hat{\mathbf{n}} \right|^2, \quad (5.5)$$

where the optimal solution for  $\hat{\mathbf{n}}$  must also satisfy the unit vector constraint. The form of Equation (5.5) is expressed for any reference frame. The representation of the reference vector establishes the coordinate frame in which the estimate for  $\hat{\mathbf{n}}$  is resolved. For the GPS case, the most convenient and useful solution is expressed in the local level reference frame.

##### 5.4.1 Estimation Procedure

The first step in the estimation of  $\hat{\mathbf{n}}$  is to compute an initial approximation,  $\mathbf{n}_o$ , that minimizes Equation (5.5) without the unit vector constraint. This solution is simply the weighted least squares result given by

$$\mathbf{n}_o = (\mathbf{H}^T \mathbf{W} \mathbf{H})^{-1} \mathbf{H}^T \mathbf{W} \mathbf{c}, \quad (5.6)$$

where

$$\mathbf{H}^T = [\hat{\mathbf{e}}_1 \ \hat{\mathbf{e}}_2 \ \dots \ \hat{\mathbf{e}}_N], \quad (5.7)$$

$$\mathbf{W} = \begin{bmatrix} \frac{1}{\sigma_1^2} & 0 & \dots & 0 \\ 0 & \frac{1}{\sigma_2^2} & & 0 \\ \vdots & & \ddots & \vdots \\ 0 & 0 & \dots & 0 & \frac{1}{\sigma_N^2} \end{bmatrix}, \quad (5.8)$$

and

$$\mathbf{c}^T = [\cos \alpha_1 \ \cos \alpha_2 \ \dots \ \cos \alpha_N]. \quad (5.9)$$

The result is then normalized to produce the first unit vector estimate

$$\hat{\mathbf{n}}_o = \frac{\mathbf{n}_o}{|\mathbf{n}_o|}. \quad (5.10)$$

Because  $\mathbf{n}_o$  is the vector that minimizes Equation (5.5) in the most general case, the value of the cost function with additional constraints on the solution can never be lower. As a result the value of Equation (5.5) at  $\mathbf{n}_o$  represents a lower bound for the actual unit vector minimization.

To determine the optimal estimate, the solution vector is first expressed in the terms of two spherical angles, as illustrated in Figure 5.6, such that,

$$\hat{\mathbf{n}}^L = \begin{bmatrix} \sin \phi \cos \theta \\ \sin \phi \sin \theta \\ \cos \phi \end{bmatrix}. \quad (5.11)$$

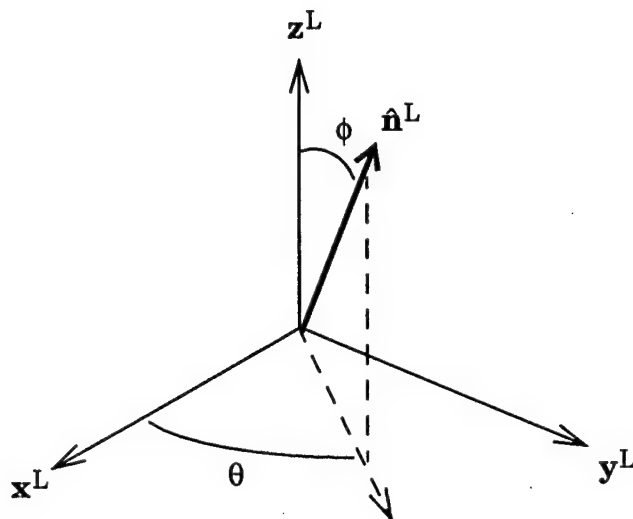


Figure 5.6. Boresight angles.

Minimizing the cost function in terms of these two angles is equivalent to minimizing it subject to the normal constraint, because all values of  $\theta$  and  $\phi$  produce a unit vector in Equation (5.11). The choice of the angles in Figure 5.6 is arbitrary. The angle  $\phi$  can be defined between the boresight vector and any one of the primary axes. However, when the boresight is parallel to the primary axis from which  $\phi$  is defined,  $\phi$  is zero and  $\theta$  is non-unique. As is evident in Equation (5.11), the  $x$  and  $y$  components of  $\hat{\mathbf{n}}$  are zero for any value of  $\theta$  when  $\phi$  is zero. Therefore, a definition of  $\phi$  should be chosen that is not close to zero.

A gradient search is performed on the two angles to find the true minimum. Making the definitions that  $\theta_i$  and  $\phi_i$  are the estimates for  $\theta$  and  $\phi$  at iteration  $i$  and,

$$\boldsymbol{\eta}_i \equiv \begin{bmatrix} \theta_i \\ \phi_i \end{bmatrix} \text{ and } \delta \boldsymbol{\eta}_i \equiv \begin{bmatrix} \delta \theta_i \\ \delta \phi_i \end{bmatrix}, \quad (5.12)$$

the cost function written in terms of these variables and expanded in a Taylor series is

$$\begin{aligned} J(\boldsymbol{\eta}_i) = J(\boldsymbol{\eta}_{i-1}) &+ \left[ \frac{\delta J}{\delta \boldsymbol{\eta}^T}(\boldsymbol{\eta}_{i-1}) \right] \delta \boldsymbol{\eta}_i + \\ &\frac{1}{2} \delta \boldsymbol{\eta}_i^T \left[ \frac{\delta^2 J}{\delta \boldsymbol{\eta} \delta \boldsymbol{\eta}^T}(\boldsymbol{\eta}_{i-1}) \right] \delta \boldsymbol{\eta}_i + \dots \end{aligned} \quad (5.13)$$

Keeping only the terms up to those quadratic in  $\delta \boldsymbol{\eta}$ , yields the solution for the correction term

$$\delta \boldsymbol{\eta}_i = \left[ \frac{\delta^2 J}{\delta \boldsymbol{\eta} \delta \boldsymbol{\eta}^T}(\boldsymbol{\eta}_{i-1}) \right]^{-1} \left[ \frac{\delta J}{\delta \boldsymbol{\eta}^T}(\boldsymbol{\eta}_{i-1}) \right]. \quad (5.14)$$

Defining the derivative of  $\hat{\mathbf{n}}$  with respect to the two angles,  $\phi$  and  $\theta$ , as the matrix

$$\frac{\delta \hat{\mathbf{n}}}{\delta \boldsymbol{\eta}^T} \equiv \begin{bmatrix} \frac{\delta \hat{\mathbf{n}}}{\delta \theta} & \frac{\delta \hat{\mathbf{n}}}{\delta \phi} \end{bmatrix}, \quad (5.15)$$

the first derivative of  $J$  with respect to  $\boldsymbol{\eta}$  is found to be

$$\frac{\delta J}{\delta \boldsymbol{\eta}}(\boldsymbol{\eta}) = - \left( \frac{\delta \hat{\mathbf{n}}}{\delta \boldsymbol{\eta}^T} \right)^T [\mathbf{H}^T \mathbf{W} \mathbf{c} - (\mathbf{H}^T \mathbf{W} \mathbf{H}) \hat{\mathbf{n}}], \quad (5.16)$$

where  $\mathbf{H}$ ,  $\mathbf{W}$ , and  $\mathbf{c}$  are the matrices defined in Equations (5.7) through (5.9), respectively. The second derivative of  $J$  is



$$\begin{aligned} \frac{\delta^2 J}{\delta \boldsymbol{\eta} \delta \boldsymbol{\eta}^T}(\boldsymbol{\eta}) = & \left( \frac{\delta \hat{\mathbf{n}}}{\delta \boldsymbol{\eta}^T} \right)^T (\mathbf{H}^T \mathbf{W} \mathbf{H}) \left( \frac{\delta \hat{\mathbf{n}}}{\delta \boldsymbol{\eta}^T} \right) - \\ & \left( \frac{\delta^2 \hat{\mathbf{n}}}{\delta \boldsymbol{\eta} \delta \boldsymbol{\eta}^T} \right) [\mathbf{H}^T \mathbf{W} \mathbf{c} - (\mathbf{H}^T \mathbf{W} \mathbf{H}) \hat{\mathbf{n}}] \end{aligned} \quad (5.17)$$

The second term in Equation (5.17) is much smaller than the first term; therefore, the second derivative is approximated as

$$\frac{\delta^2 J}{\delta \boldsymbol{\eta} \delta \boldsymbol{\eta}^T}(\boldsymbol{\eta}) \approx \left( \frac{\delta \hat{\mathbf{n}}}{\delta \boldsymbol{\eta}^T} \right)^T (\mathbf{H}^T \mathbf{W} \mathbf{H}) \left( \frac{\delta \hat{\mathbf{n}}}{\delta \boldsymbol{\eta}^T} \right). \quad (5.18)$$

The initial estimates for  $\theta$  and  $\phi$  are determined from the evaluation of  $\hat{\mathbf{n}}_0$  and Equation (5.11). The correction term for these values is then computed from Equation (5.14). Updated estimates are computed from the equation

$$\begin{bmatrix} \theta_{i+1} \\ \phi_{i+1} \end{bmatrix} = \begin{bmatrix} \theta_i \\ \phi_i \end{bmatrix} + \begin{bmatrix} \delta \theta_i \\ \delta \phi_i \end{bmatrix}. \quad (5.19)$$

#### 5.4.2 The Shuster Algorithm Applied to SNR Measurements

For the GPS case, the angles,  $\alpha_k$ , are the off-boresight angles derived from the SNR measurements, the reference vectors,  $\hat{\mathbf{e}}_k$ , are the LOS vectors, and the vector to be estimated,  $\hat{\mathbf{n}}$ , is the antenna boresight. The computation of the measurement weights is taken from the calibration function as described in Section 4.8.1.

To perform instantaneous attitude estimation, the observations are taken simultaneously; thus, the number of angles is limited by the tracking capabilities of the GPS receiver. In other words, the value of  $N$  in Equation (5.5) is equal to the number of satellites tracked. It is interesting

to note that the unconstrained measurement gradient, computed by Equation (5.7), for this type of solution is merely the GPS LOS vector. This means that an indication of the contribution of satellite geometry to the attitude is described by the position dilution of precision (PDOP) generally used to quantify navigation performance. This is computed by

$$\text{PDOP} = \sqrt{\text{trace}((\mathbf{H}^T \mathbf{H})^{-1})}. \quad (5.20)$$

Simpler methods for computing boresight direction based upon the angles measurements and LOS vectors may also be considered for computational reasons. Two techniques evaluated for comparison to Shuster's optimal solution are a simple average of LOS vectors for all tracked satellites, and the  $\hat{\mathbf{n}}_0$  computed from normalized result of Equation (5.6) used to initialize the search in the MLE solution.

### 5.4.3 Estimation Error Covariance

Given the true boresight axis and assuming the prediction errors are normally distributed with zero mean, the theoretical error covariance matrix based on the MLE solution can be predicted for the two angles in the estimation procedure [Shuster, 1983]. The inverse of the covariance matrix is

$$\mathbf{P}_{\delta\eta\delta\eta}^{-1} = \left( \frac{\delta\hat{\mathbf{n}}}{\delta\eta^T} \right)^T (\mathbf{H}^T \mathbf{W} \mathbf{H}) \left( \frac{\delta\hat{\mathbf{n}}}{\delta\eta^T} \right). \quad (5.21)$$

Equation (5.21) gives a convenient way to evaluate the expected performance of the boresight estimation procedure on the test data. If the true attitude is known, then  $\mathbf{P}_{\delta\eta\delta\eta}$  can be evaluated from the values of  $\hat{\mathbf{n}}$ ,  $\mathbf{H}$ , and  $\mathbf{W}$ . When expanded, the covariance matrix is

$$\mathbf{P}_{\delta\eta\delta\eta} = \begin{bmatrix} E(\delta\theta^2) & E(\delta\theta\delta\phi) \\ E(\delta\theta\delta\phi) & E(\delta\phi^2) \end{bmatrix}. \quad (5.22)$$

Therefore, the expected values of  $\delta\theta$  and  $\delta\phi$  are simply the square roots of the diagonals. The errors computed from the actual results should agree with these expected errors to a level of certainty of  $1\sigma$ .

## 5.5 Spinning Satellite SNR-Based Attitude Determination

There are three distinct ways a GPS antenna might be mounted on a spinning satellite. The preferred orientation is with the plane of the antenna lying flat on one of the satellite's faces so that the boresight vector is parallel to the angular momentum axis. The second is with the plane of the antenna mounted on the side of the satellite so that the boresight vector is perpendicular to the angular momentum axis. The other orientation is with the boresight mounted between these two extremes at an acute angle to the angular momentum axis.

### 5.5.1 Boresight Mounted Parallel to the Angular Momentum Axis

In this mounting scheme, the orientation of the boresight vector is equal to the orientation of the angular momentum vector as illustrated in Figure 5.7. As a result, estimation of the boresight vector using the single-axis SNR approach directly estimates the angular momentum axis.

This is the preferred mounting scheme, because every boresight calculation can be used as the current attitude estimate. Averaging is desirable, but not required. No assumptions about the stability are needed. Estimates can be continuously made throughout torquing maneuvers that alter the position of the angular momentum axis.

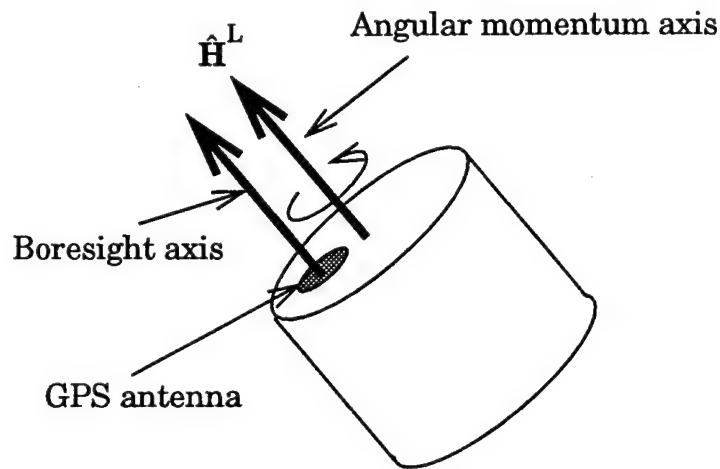


Figure 5.7. Parallel mounting.

One likely scenario is that the angular momentum axis is relatively constant over a short time period. This situation occurs between torquing maneuvers. Averaging or filtering of the instantaneous estimates can be employed to improve the accuracy. Furthermore, since the angular momentum axis is constant in the local system, its orientation can be thought of in terms of the antenna alignment problem as describe in section 4.9. In this case, the body system can be temporarily defined to coincide with the local system during the time of constant orientation. A batch of SNR and LOS measurements from this period, can be used in Equation (4.21) to solve for the elements of the boresight vector in the body frame,  $\hat{\mathbf{n}}^B$ , where we set

$$\hat{\mathbf{H}}^L = \hat{\mathbf{n}}^B.$$

The biggest disadvantage to this mounting scheme is that the GPS antenna has to be placed in an area of the satellite that may be the most desirable for other instruments. The face of the satellite remains in an ori-

entation that is relatively constant compared to the sides. Scientific instruments or communications antennas, which are generally the primary mission payload, may require a fixed pointing direction and thus, need to be mounted here. A lack of room for a GPS antenna or too much signal blockage from the other devices might be the result.

### 5.5.2 Boresight Mounted Perpendicular to Angular Momentum Axis

In this mounting scheme, the orientation of the boresight vector significantly changes with each measurement as it rotates about the angular momentum axis. If the satellite is assumed to be in a stable spinning orientation, the boresight vector always remains perpendicular to the angular momentum vector as shown in Figure 5.8. Averaging of the instantaneous boresight estimates is not applicable because there is no component of the vectors, excluding the errors in the estimates, that lie along the angular momentum axis. For example, suppose local system is defined such that

$$(\hat{\mathbf{H}}^L)^T = [0 \ 0 \ 1]. \quad (5.23)$$

The boresight vector in the local frame,  $\hat{\mathbf{n}}^L$ , is going to be of the form

$$(\hat{\mathbf{n}}_i^L)^T = [\cos \omega t_i \ \sin \omega t_i \ 0],$$

where  $\omega$  is the spin rate. For perfect and equally spaced estimates, averaging of the  $\hat{\mathbf{n}}_i^L$  values results in the null vector. For non-perfect estimates, the average still tends to zero if the estimation errors are symmetric about the true boresight. Instead, if we take the unit vector of the cross product of any two estimates we compute

$$(\hat{\mathbf{H}}^L)^T = \frac{(\hat{\mathbf{n}}_i^L)^T \times (\hat{\mathbf{n}}_j^L)^T}{|(\hat{\mathbf{n}}_i^L)^T \times (\hat{\mathbf{n}}_j^L)^T|} = \frac{\begin{bmatrix} 0 & 0 & \cos\omega t_i \sin\omega t_j - \cos\omega t_j \sin\omega t_i \end{bmatrix}}{\begin{bmatrix} 0 & 0 & \cos\omega t_i \sin\omega t_j - \cos\omega t_j \sin\omega t_i \end{bmatrix}} \quad (5.24)$$

or

$$(\hat{\mathbf{H}}^L)^T = \begin{bmatrix} 0 & 0 & 1 \end{bmatrix}. \quad (5.25)$$

For noisy estimates, we must take the average over a batch of cross product results.

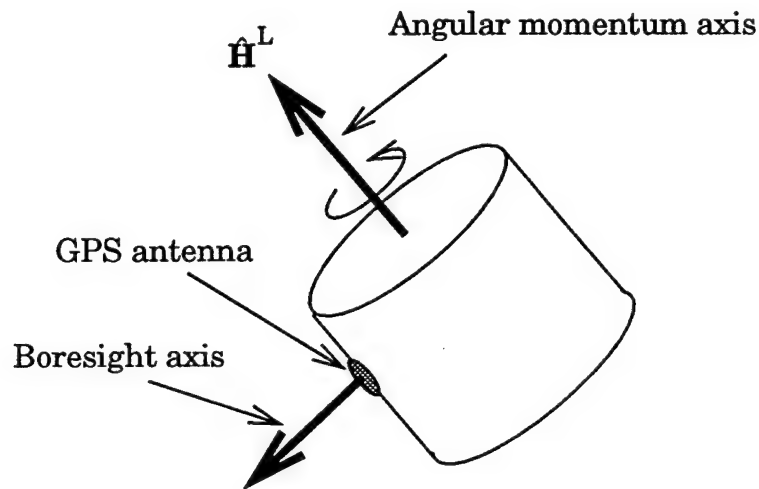


Figure 5.8. Perpendicular mounting.

This mounting scheme has several disadvantages. The first one is that batch processing of the instantaneous estimates is a necessity. The angular momentum axis, therefore, must remain approximately constant over the time span of the data collection batch. This condition might not be met during maneuvers. Other problems might occur if there is too much GPS satellite blockage as the antenna rotates and faces the direction of the Earth. This might be mitigated by weighting the boresight estimates

according to their satellite visibility conditions. Estimates made with the most satellites would be weighted the highest. One possible approach is

$$(\hat{\mathbf{H}}^L)^T = \left| \sum_{i=1}^n \frac{F(s_i, s_{i+k})}{n} (\hat{\mathbf{h}}_i)^T \right|, \quad (5.26)$$

where

$$(\hat{\mathbf{h}}_i)^T = \left| (\hat{\mathbf{n}}_i^L)^T \times (\hat{\mathbf{n}}_{i+k}^L)^T \right|, \quad (5.27)$$

$(\hat{\mathbf{n}}_i^L)^T$  and  $(\hat{\mathbf{n}}_{i+k}^L)^T$  are the antenna boresight estimates at epoch  $i$  and at an epoch  $k$  measurements later, and  $F(s_i, s_{i+k})$  is some empirically determined function of the number of satellites in view at the two epochs.

In late 1997, the SNOE satellite, described earlier, is expected to be launched aboard a Pegasus XL launch vehicle. It has a GPS antenna mounted on the side of the satellite which may provide data to analyze this estimation scenario.

### 5.5.3 Boresight Mounted Acutely to the Angular Momentum Axis

In this mounting scheme, the angle between the boresight vector and the angular momentum vector is acute as shown in Figure 5.9. Since the SNR based method gives only single axis information, knowing the orientation of the antenna boresight in the body frame is not sufficient. Averaging or some type of batch filtering must be used. As the antenna boresight rotates about the angular momentum axis, it maintains a constant angle. The components of each instantaneous estimate that lie in the plane perpendicular to the angular momentum axis average out to zero as the boresight cones about it. The components that lie parallel to the angular momentum axis average to a constant vector, which is the final axis

estimate. While in this situation the boresight orientation in the local system is not constant, the average of equally spaced orientations over one revolution is. As a result, the boresight alignment technique may be applicable.

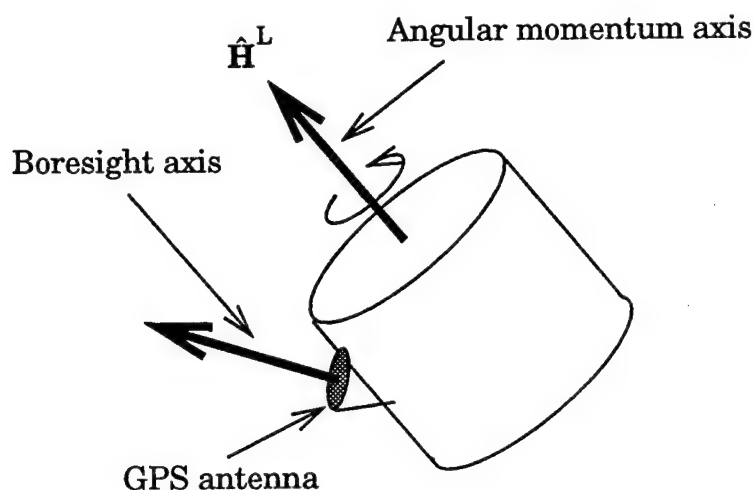


Figure 5.9. Acute angle mounting.

### 5.6 Three-Axis SNR-Based Attitude Determination

The major additional requirement for the three-axis case is the need for either another antenna or measurable azimuthal variations in the antenna gain patterns. Because azimuthal variations are very difficult to measure, especially at the level of accuracy of the SNR measurements, this case is not examined. The addition of a second non-parallel antenna adds the estimation of another axis as shown in Figure 5.10.

Computation of the local-to-body attitude matrix,  ${}^L C^B$ , is performed in two steps. The first involves the estimation of a rotation matrix,  ${}^S C^B$ , between a reference frame, denoted by the superscript S, defined by the two boresight axes,  $\hat{b}_1$  and  $\hat{b}_2$ , and the body frame, denoted with the



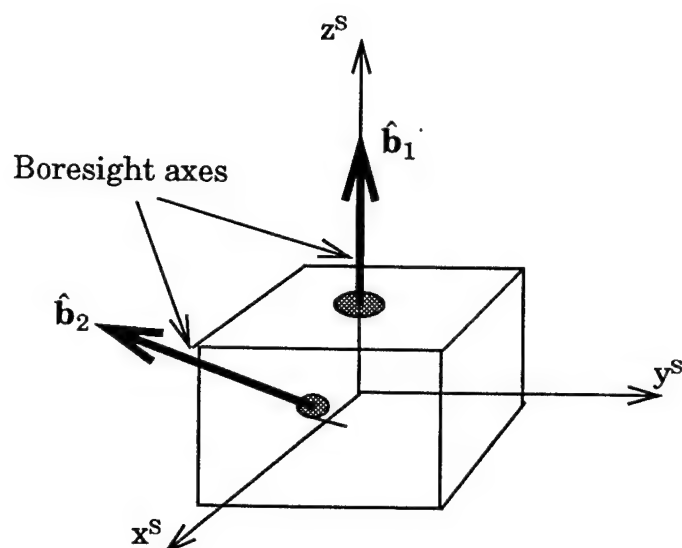


Figure 5.10. Three axis estimation.

superscript B. This matrix is constant, assuming the spacecraft is rigid and the body position of the antennas do not change. Using the alignment calibration procedure from section 4.9, the two boresight vectors are estimated in the body frame. An orthonormal set of axis are formed to arrive at  ${}^S\mathbf{C}^B$  as described in section 2.5. This matrix only has to be computed once.

It is important to note that the computation for  ${}^S\mathbf{C}^B$  depends on one of three conditions being satisfied. Two of the conditions are direct requirements of the alignment calibration procedure. As in the single-axis case, they are either that the attitude is constant or that a truth attitude reference is available during the calibration period. Both of these conditions are readily met if a ground calibration is performed. If the mapping function generated from the antenna gain pattern, then the third condition is that the precise antenna alignment is known from accurate mechanical drawings.

The second step involves computing the transformation between the local system and the boresight system,  ${}^L C^S$ . The single-axis SNR-based estimation computes the boresight vectors in the local frame. As with the first transformation, knowing two non-colinear boresight vectors in the local frame allows us to compute an orthonormal set of axes to form  ${}^L C^S$ . Combining the two rotation matrices yields  ${}^L C^B$ . If the vehicle attitude is constant over the data collection interval, the two steps can be combined to directly estimate  ${}^L C^B$  using one of the techniques to solve for the minimization of the Wahba cost function given in Equation (2.22).

## 5.7 Conclusions

The SNR-based single-axis estimation technique is applicable to both the estimation of the angular momentum axis of a spinning satellite and three-axis estimation. For the spinning satellite case, if the antenna boresight is parallel to the angular momentum axis, the SNR method directly estimates it. Assuming the axis is constant allows either the averaging of the instantaneous estimates or the application of the alignment calibration. For a side mounted antenna, the cross products of pairs of the instantaneous estimates have to be averaged. Variable visibility conditions could impose the need for weighting of the estimates. Three-axis estimation requires an additional antenna. The constant transformation matrix between the system defined by the antenna boresights and body has to be determined from either a calibration set or from mechanical drawings of the antenna orientations. Each pair of estimates of the two antenna boresights are used to estimate the transformation matrix between the local system and the antenna system.



## CHAPTER 6

### SNR TEST DATA

#### 6.1 Introduction

The data used in this research for SNR-based single-axis estimates are derived from a variety of receiver and antenna combinations. Each data set has a corresponding source of truth attitude information used for performance assessment of the algorithms.

Data are taken from five different sources. Three of the sources are space based GPS receivers and two are ground receivers. Three of the data sources, two space and one ground, use the six channel Trimble TANS Vector. One space source uses the eight channel Allen Osborne Associates TurboStar receiver. The other ground source uses a 12 channel NovAtel receiver. A detailed description of the receivers and data sets follows.

#### 6.2 TANS Vector Receiver

The TANS Vector has six parallel tracking channels and a multiplexed front end allowing it to track satellites on four antennas [Trimble, 1993]. Normally with four antennas in operation, it measures phase differences between one antenna designated as the master and the three other antennas. This information, taken from the "E4" data packets, along with the GPS LOS vectors, taken from the "EC" data packets, are used to esti-

mate attitude. In this paper, measurements from only one antenna are required. A picture of the TANS Vector is shown in Figure 6.1.

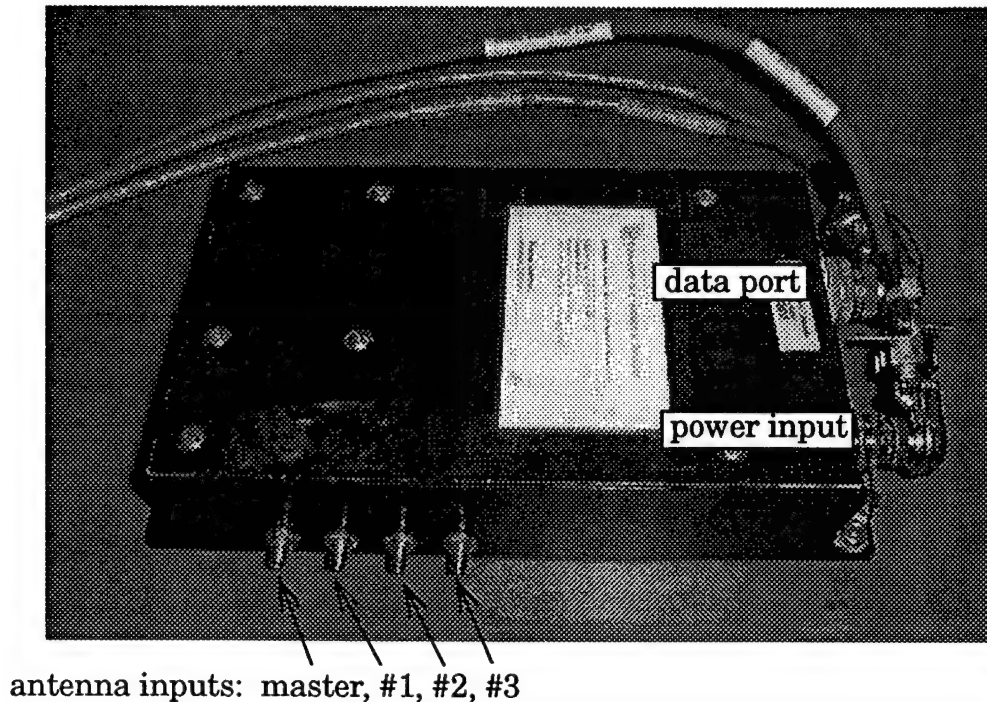


Figure 6.1. The Trimble TANS Vector.

### 6.3 NovAtel 12 Channel Receiver

The NovAtel receiver is based on the NovAtel GPSCard OEM Series receiver model number 3151R [NovAtel, 1993]. The GPSCard Series are multi-channel parallel tracking, C/A code receivers. Model 3151R has the capability of simultaneously tracking up to 12 GPS satellites. The antenna used for the data collection in this research is a microstrip patch antenna with a built-in low noise amplifier (LNA) and bandpass filter. Data are collected using a PC through a serial port connection. For this research, the "rnga" data packets containing the SNR measurements in dB and the "sata" data packets containing the azimuth and elevation to the GPS satel-

lites in degrees are recorded. A picture of the NovAtel receiver and antenna is shown in Figure 6.2.

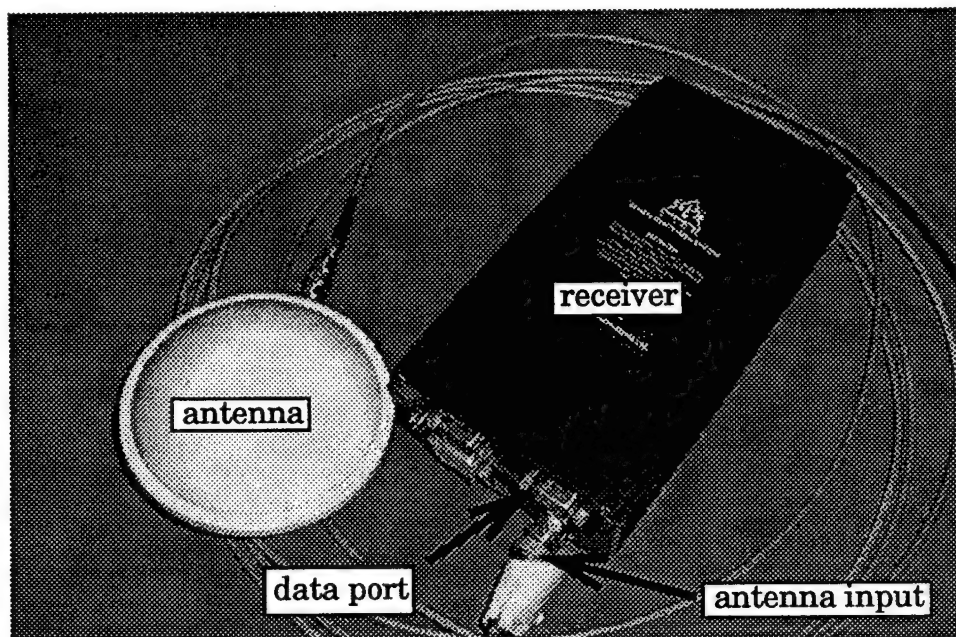


Figure 6.2. The 12 Channel NovAtel.

#### 6.4 GANE

The GANE data are taken from the GPS Attitude and Navigation Experiment (GANE), flown on the space shuttle Endeavour during May 1996 [Carpenter and Hain, 1997]. The measurements are from a TANS Vector receiver and four patch antennas mounted on a structure in the shuttle payload bay. The antennas are mounted in a rectangle with their boresights pointing out of the payload bay. Each antenna is surrounded by a choke ring. An Inertial Reference Unit (IRU) provides an external attitude reference. A photograph of GANE prior to its placement in the shuttle bay is shown in Figure 6.3.

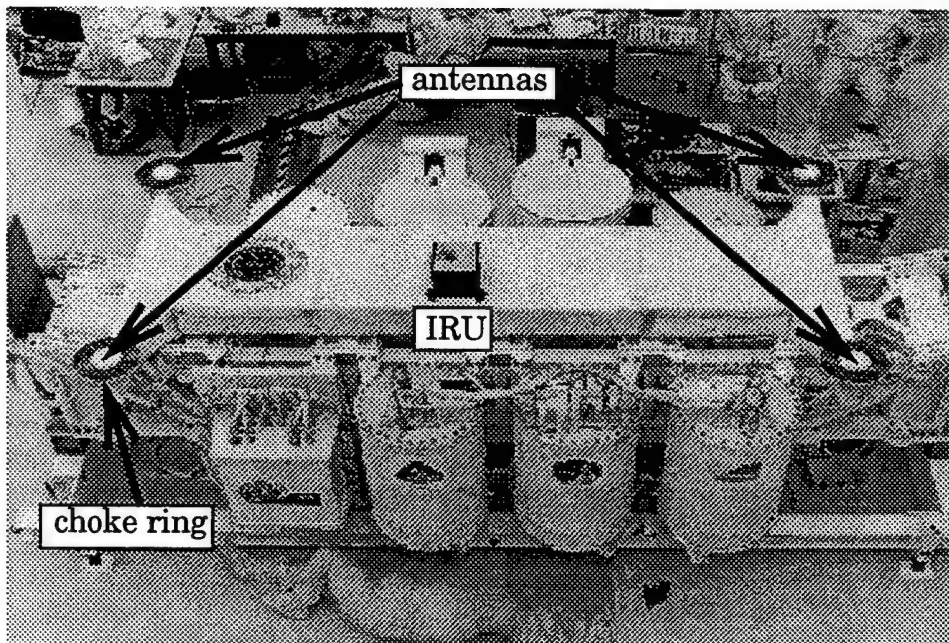


Figure 6.3. The GANE experiment. [GANE Home Page]

Data are from two different orientations. In the first (GANE #1), the GANE antennas are oriented away from the Earth with the boresights in the zenith direction and with the shuttle approximately tangent to its orbit. In the second (GANE #2), the shuttle's nose is pitched about the orbit normal. The GPS antennas are oriented approximately 41 deg off zenith.

Both data sets analyzed in this research are 4 hours long with SNR measurements taken approximately every 5 seconds. Each set contains about a 2 hour segment when a reliable truth reference is available.

## 6.5 CRISTA-SPAS

The CRISTA-SPAS satellite, built by Daimler-Benz Aerospace, was released by the Space Shuttle Atlantis in November, 1994, later retrieved, and returned to Earth. The primary mission was to explore the middle

atmosphere, and a secondary experiment tested GPS-based attitude determination. While in free flight, the spacecraft was in a circular orbit at an inclination of 57 deg. The orbit altitude was about 300 km. The satellite was 3-axis controlled. Primary attitude determination was provided by a star tracker and gyro inertial measurement unit (IRU) accurate to 0.05 deg [Brock et al., 1995].

In the secondary experiment, a GPS receiver provided by Space Systems/Loral was used to independently produce attitude data. This receiver was a TANS Vector modified by Stanford University for attitude determination in space [Lightsey et al., 1994]. Four GPS patch antennas were mounted on the zenith face of the spacecraft [Ward, L.M., 1996].

The total data set from CRISTA-SPAS spans a period of over 30 hours. Measurements are at intervals of 3 to 10 seconds. These measurements are coordinated with the IRU attitude and with precise GPS ephemerides computed by the Jet Propulsion Laboratory [Zumberge and Bertiger, 1996]. For analysis, the IRU data is used as a truth reference. A picture of the satellite attached to the space shuttle robot arm is shown in Figure 6.4.

## 6.6 GPS/MET

The GPS-based meteorology (GPS/MET) project consists of an orbital experiment on the Orbital Sciences MicroLab-1 spacecraft. The project is sponsored by the University Corporation for Atmospheric Research (UCAR) and the National Science Foundation (NSF). Launched on April 3, 1995, the 63 kg satellite operates in a 70 deg inclined orbit and an altitude of approximately 740 km. Its attitude is stabilized by a gravity



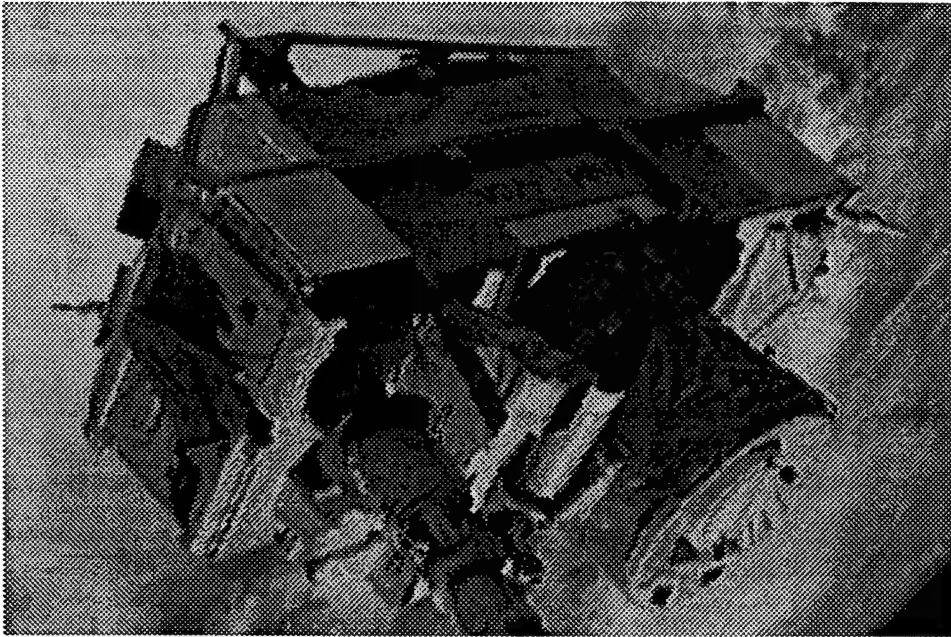


Figure 6.4. The CRISTA-SPAS Satellite. [JSC Digital Image Collection Home]

gradient boom and is controlled by torque rods. Attitude estimates are computed from the filtering of data from Earth sensors and a magnetometer. These are used as the truth reference. Accuracy is expected to be between 5-10 deg in pitch and roll and 10-15 deg in yaw [Krebs, 1997].

On board is a dual frequency TurboStar GPS receiver developed by JPL and the Allen Osborne Associates (AOA). Its primary objective is to take high frequency measurements of signals from GPS satellites near the Earth's horizon to sound the atmosphere. Additionally, 1 Hz measurements are taken from all the GPS satellites in view. A diagram of the satellite is shown in Figure 6.5.

For this work, both L1 and L2 SNR data are analyzed. Three data sets collected in 1997, the first from February 2 (GPS/MET #1), the second from February 20 (GPS/MET #2), and the third from February 26 (GPS/

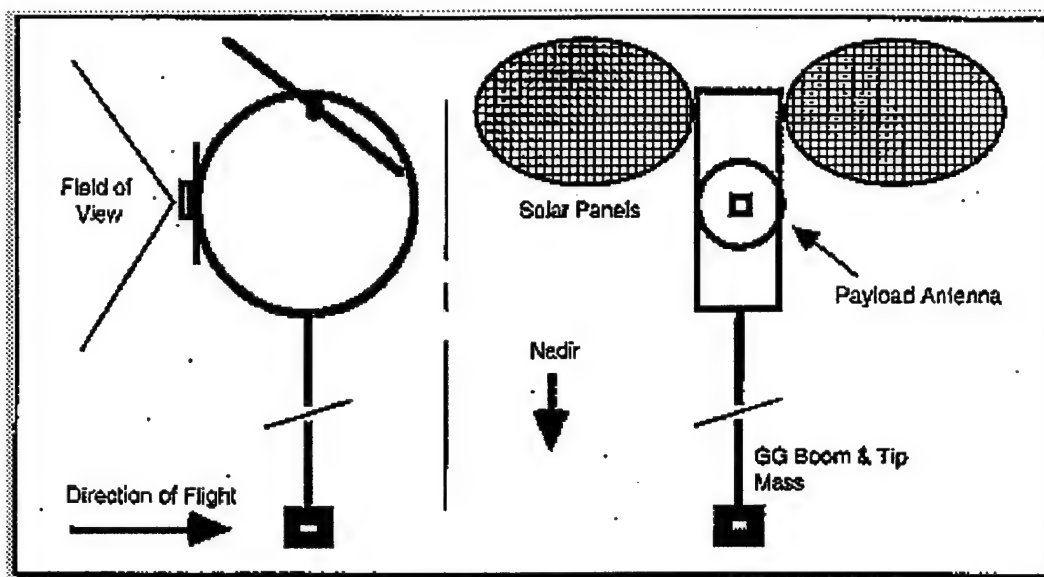


Figure 6.5. Diagram of the GPS/MET satellite [GPS/Met Home Page].

MET #3), are examined. Each set is approximately 16 hours in duration. In GPS/MET #1 the antenna boresight vector is approximately in the satellite velocity vector. In GPS/MET #2 the satellite is in its nominal attitude with the antenna boresight facing opposite the velocity vector. In GPS/MET #3, the antenna boresight is in the orbit normal direction.

## 6.7 Ground TANS

A TANS Vector receiver was set up on the roof of the University of Colorado Engineering Center as shown in Figure 6.6. It was attached to four antennas mounted on a rectangular wooden board. The orientation of the board remained constant throughout the collection period. Data was recorded between May and August, 1997.

For this research, data sets with a duration of at least 20 hours are analyzed. Measurements are at intervals of 2.5 minutes. The SNR data is from the upper right antenna which is designated as the master. The

phase-based attitude solution from all four antennas is used as the truth reference. Results are presented from a set referred to as Ground TANS.

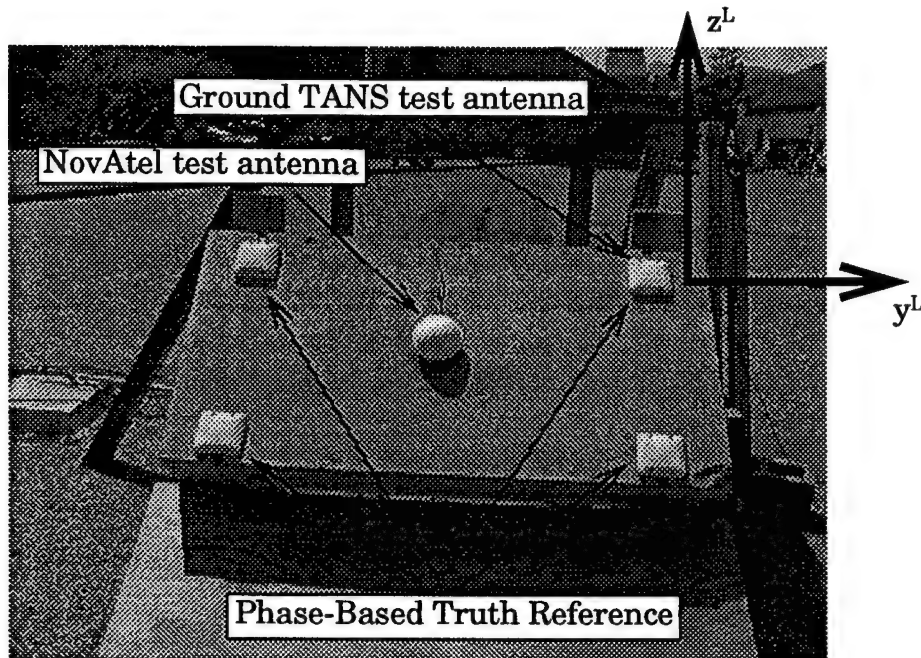


Figure 6.6. Ground experiment setup.

## 6.8 NovAtel Ground

A 12 channel NovAtel receiver was set up on the roof of the University of Colorado Engineering Center. It was attached to the center of a wooden structure as shown in Figure 6.6. As with the Ground TANS sets, the orientation of the antenna boresight vector was constant. Data was collected between May and August, 1997.

Data sets of over 24 hours in duration taken at intervals of 2.5 minutes are examined in this research. Data from three different antennas, a NovAtel patch, a Trimble patch, and an Ashtech patch with a choke ring, are used for the various data collections. Four primary data sets are ana-

lyzed. The first, called NovAtel #1, comes from data taken with the NovAtel patch antenna in May. The second, called NovAtel #2, comes from the Ashtech antenna. NovAtel #3 comes from the Trimble antenna. The last set, NovAtel #4, also comes from the NovAtel antenna, but is from August. A TANS Vector in normal attitude mode is used for the reference attitude.

### 6.9 $\alpha$ vs. SNR for the Data Sets

Figures 6.7 through 6.13 show the  $\alpha$  versus SNR relationship for the various data sets. For the purposes of a comparison between all of the data sets, the NovAtel and GPS/MET SNR output are converted into AMU's using Equation (4.1). To get the Novatel  $C/N_0$  to the same range as the Vector AMU's, a bandwidth of 333 Hz is assumed.

To quantify the overall quality of the relationship between off-bore-sight angle and SNR, the value of  $\Delta p$  in degrees is computed. It is defined as the mean of the absolute value of the residuals between the data points and a 5th order polynomial fit to the points.

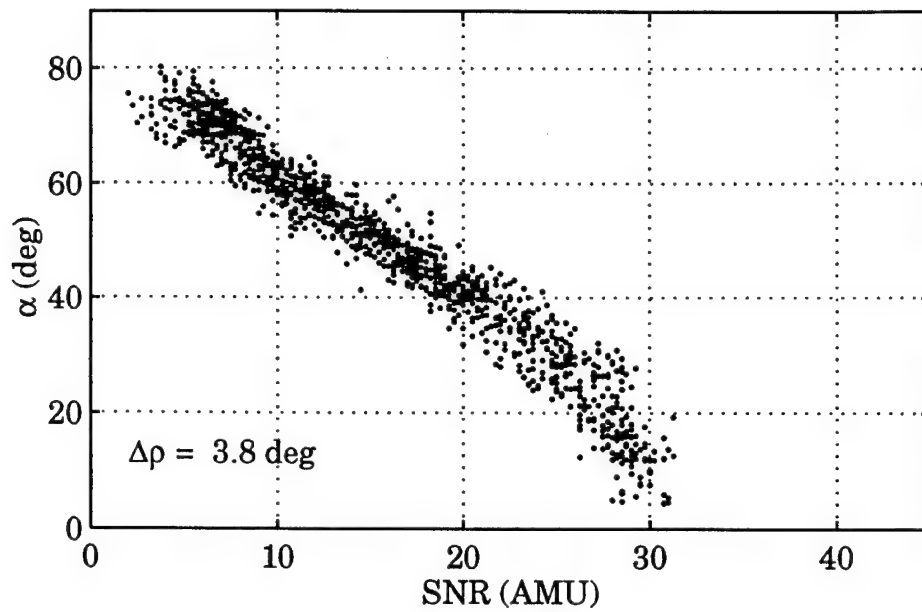


Figure 6.7. GANE  $\alpha$  vs. SNR.

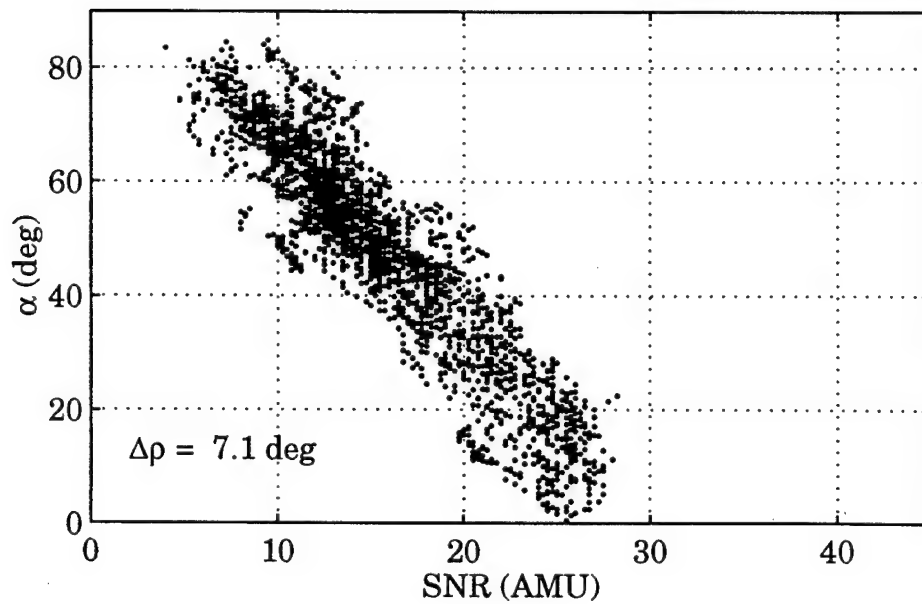


Figure 6.8. CRISTA-SPAS  $\alpha$  vs. SNR.

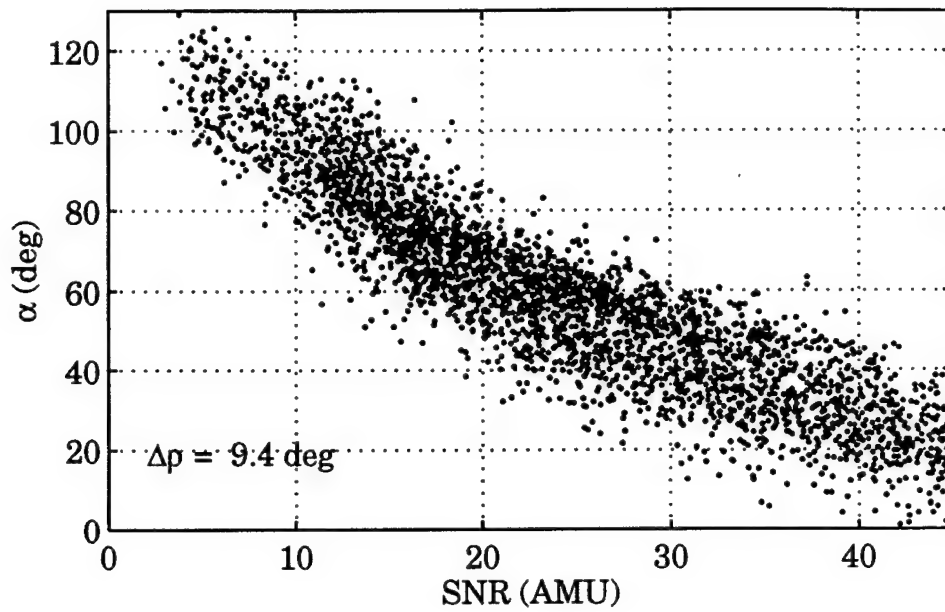


Figure 6.9. GPS/MET  $\alpha$  vs. SNR.

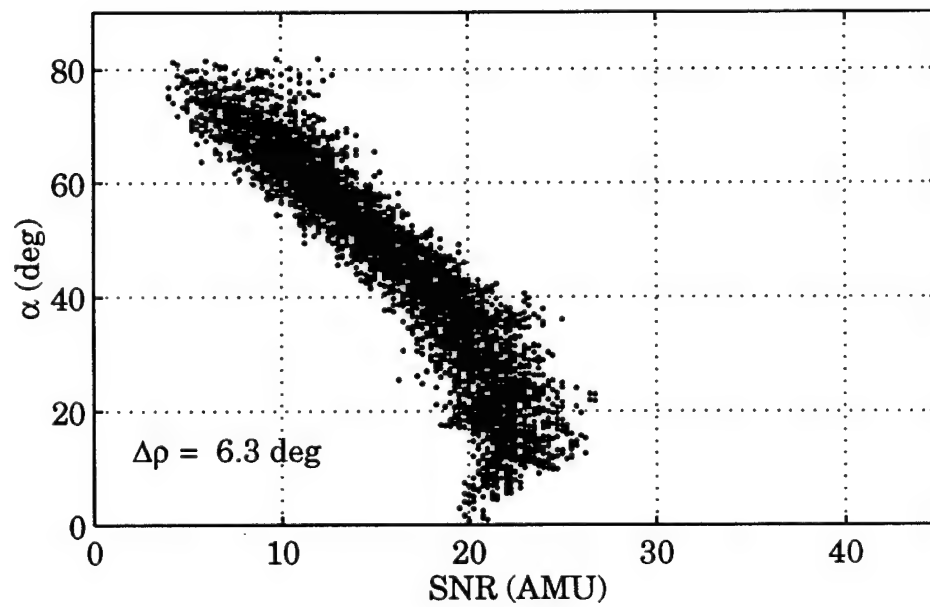


Figure 6.10. Ground TANS  $\alpha$  vs. SNR.

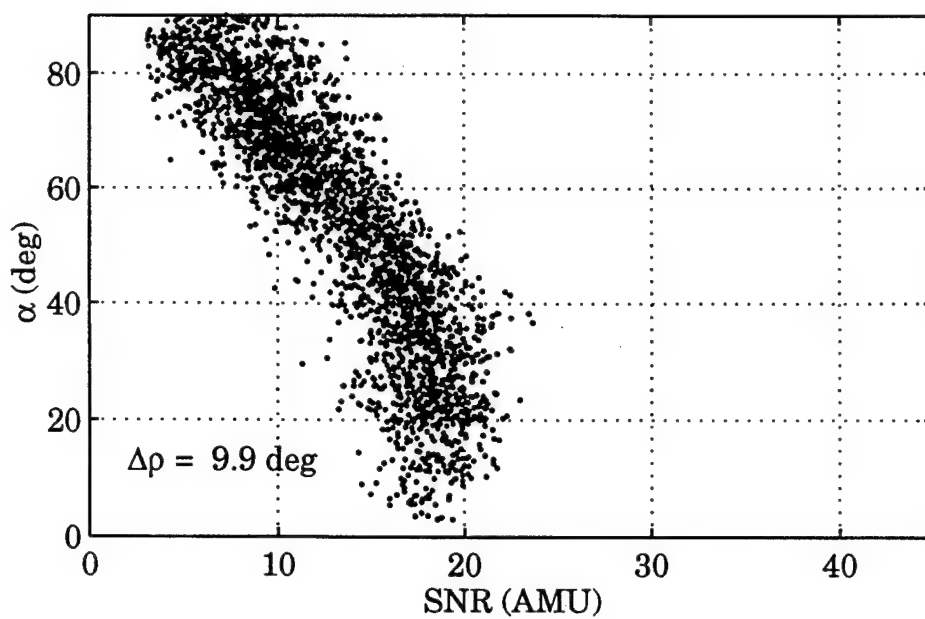


Figure 6.11. NovAtel  $\alpha$  vs. SNR (NovAtel antenna).

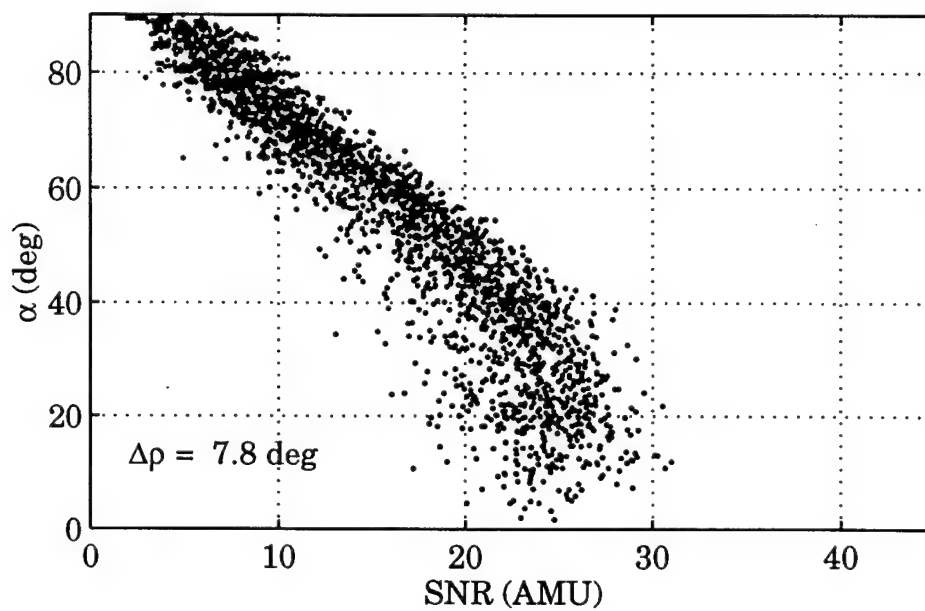


Figure 6.12. NovAtel  $\alpha$  vs. SNR (choke ring antenna).

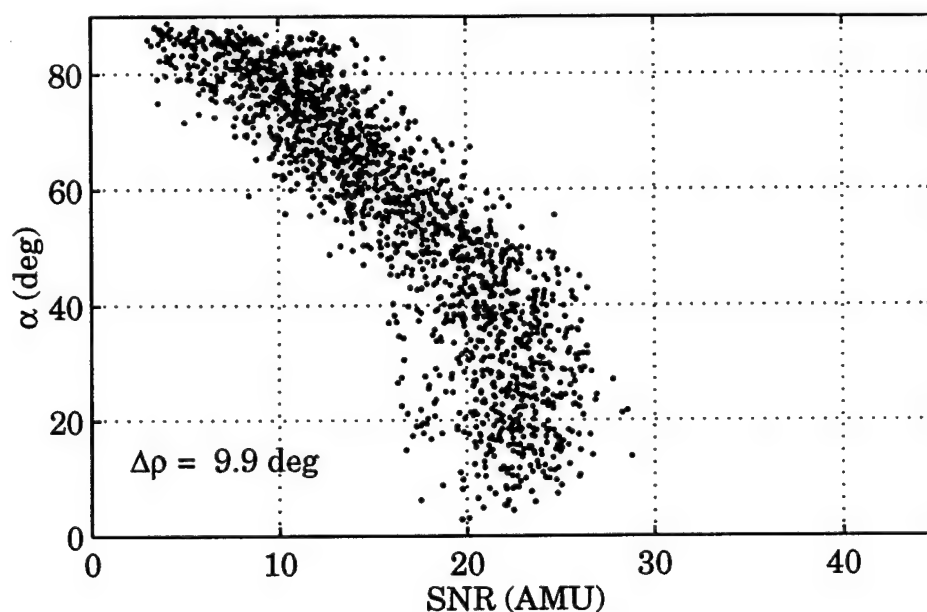


Figure 6.13. NovAtel  $\alpha$  vs. SNR (TANS antenna).

### 6.10 Normal Distribution Assumption

Analysis of the data sets shows that the distribution of the  $\alpha$ 's is symmetrically distributed in each SNR bin. The distributions vary for each data set and for each SNR bin. Statistical tests indicate that the distributions range from approximately uniform in nature to Gaussian or in some cases a contaminated Gaussian (a Gaussian with a specific mean and variance mixed with a Gaussian having a different mean and variance).

#### 6.10.1 Test Statistic

The statistic used to test the normal distribution assumption is based on the tail weights of the cumulative distribution function (cdf) [Hoaglin, et al., 1983]. The analysis shows how extreme portions of the distribution are spread out in relation to the width of the center. The test



statistic,  $\tau$ , is defined as the ratio of the width of the cdf between the median and the 99th percentile to the width between the median and the 75th percentile. This ratio is then normalized by the ratio for a true normal distribution. It is calculated by

$$\tau(F) = \frac{F^{-1}(0.99) - F^{-1}(0.5)}{F^{-1}(0.75) - F^{-1}(0.5)} \bigg/ \frac{\Phi^{-1}(0.99) - \Phi^{-1}(0.5)}{\Phi^{-1}(0.75) - \Phi^{-1}(0.5)}. \quad (6.1)$$

where  $F$  is the cdf of the test data and  $\Phi$  is the cdf of the normal distribution. Table 6.1 gives the values of  $\tau$  for several common distributions. The

Table 6.1.  $\tau$  for some standard distributions. [Hoaglin, et al., 1983]

Distribution	$\tau(F)$
Uniform	0.57
Triangular	0.86
Normal	1.00
CN(0.05; 3)	1.20
Double - Exponential	1.63
CN(0.05; 10)	3.42
Cauchy	9.22

distribution CN(.05; 3) represents a normal distribution with  $\mu=0$  and  $\sigma^2=1$ , contaminated by a 5% mixture of another normal distribution with  $\mu=0$  and  $\sigma^2=3$ .

Figures 6.14 through 6.18 show a plot of the test statistic applied to the cdf of the off-boresight angles for each SNR bin for the various data sets. Each figure consists of three plots. The solid line corresponds to the

test statistic applied to each SNR bin of the test data. The dot-dash line corresponds to the test statistic applied to sets of normally distributed random numbers generated in MATLAB with mean, variance, and set size equal to those of the test data bins. The dashed line corresponds to the test statistic applied to sets of uniformly distributed random numbers generated in MATLAB with mean and set size equal to those of the test data bins and with limits equal to  $\pm 1.7$  times the standard deviation of the test data bins.

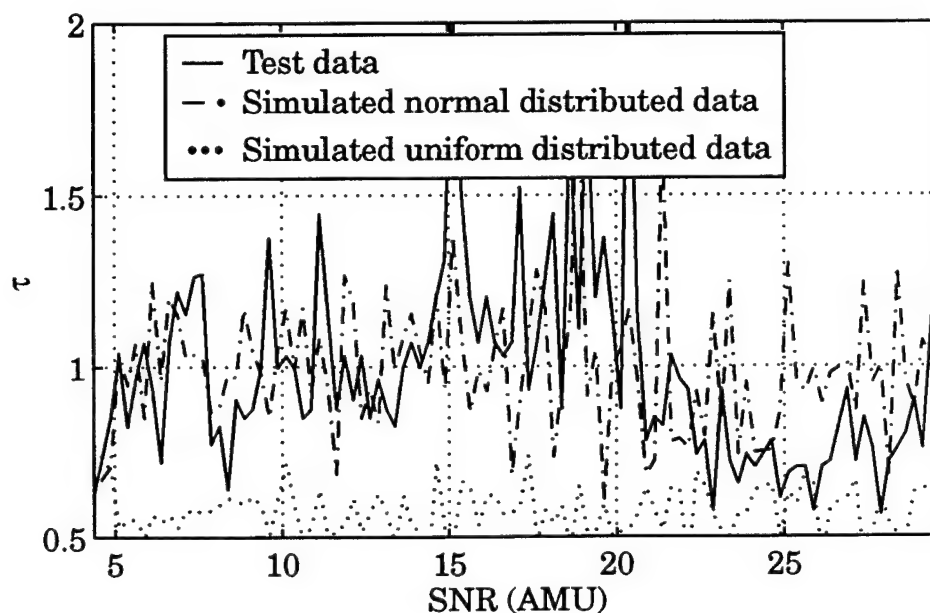


Figure 6.14. Distribution test for GANE #1.

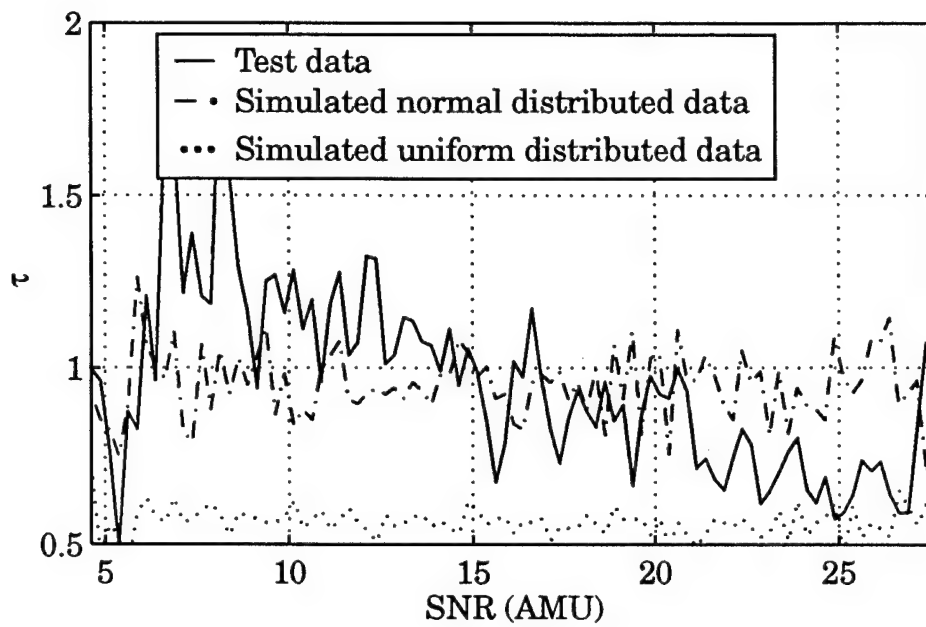


Figure 6.15. Distribution test for CRISTA-SPAS.

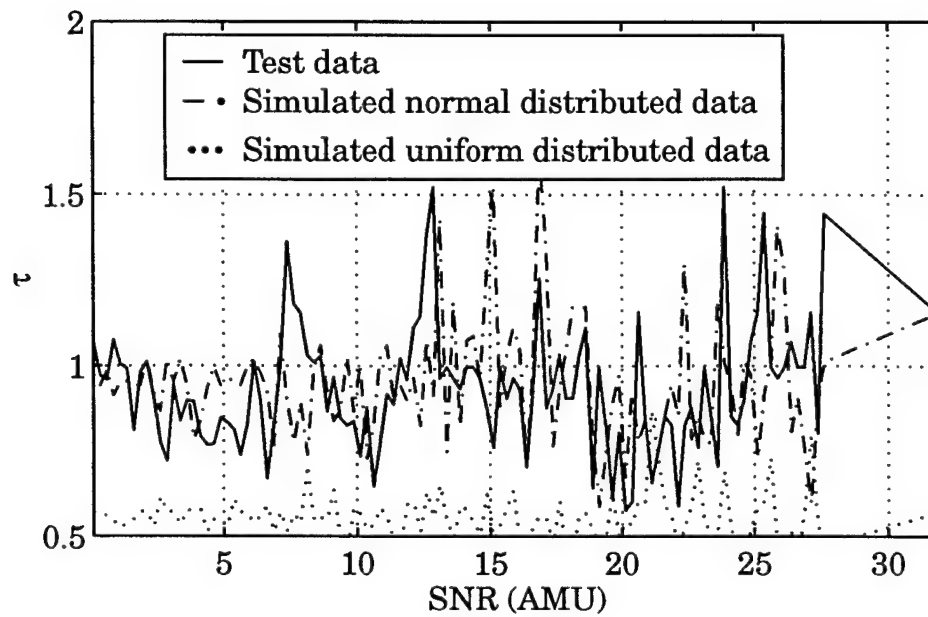


Figure 6.16. Distribution test for GPS/MET.

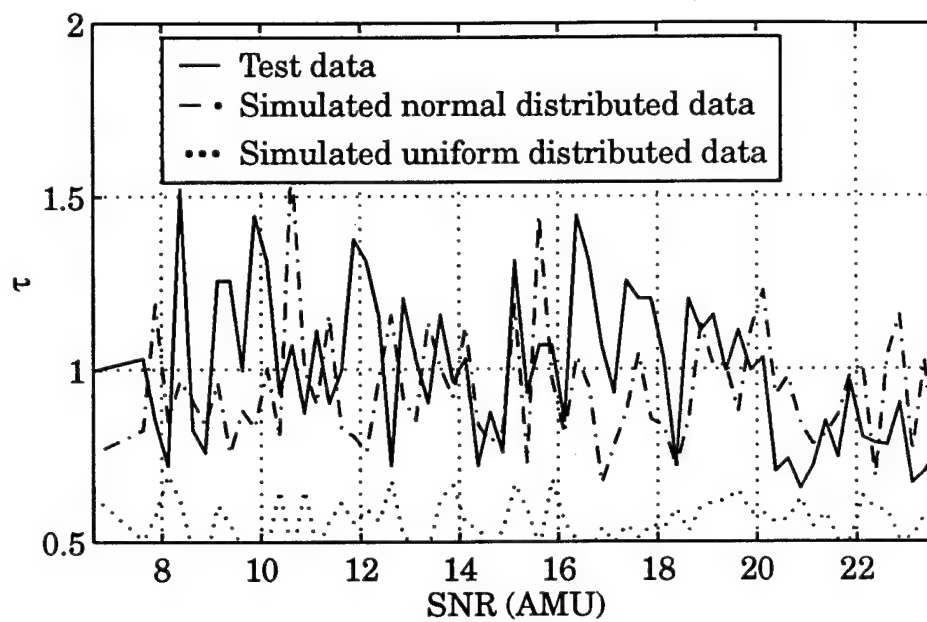


Figure 6.17. Distribution test for Ground TANS.

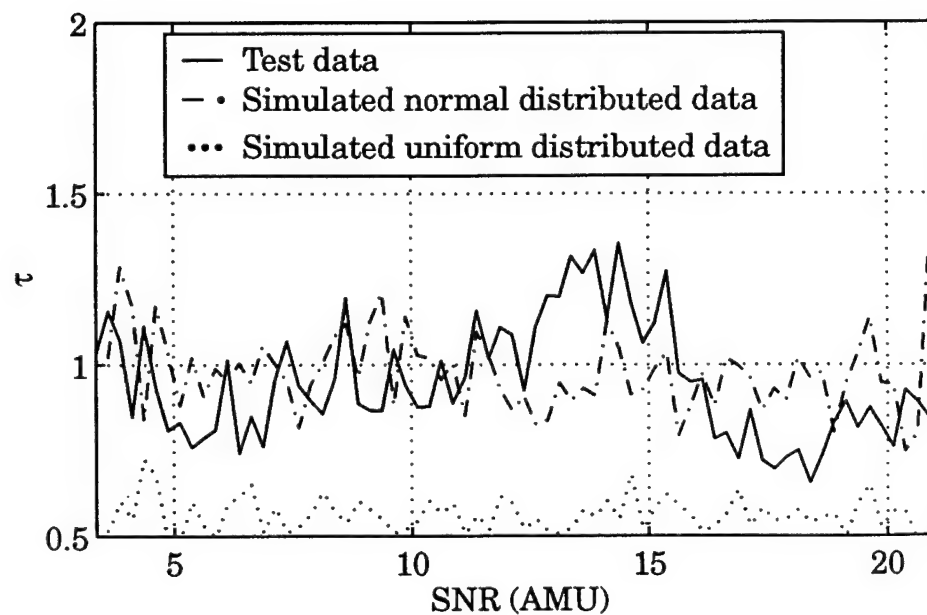


Figure 6.18. Distribution test for NovAtel #1.

While the data clearly show some contamination from a true normal distribution, the data always correspond to a distribution symmetric about some angle. As a result, methods based on finding the maximum likelihood estimate (MLE) are applicable.

## 6.11 Conclusions

The variety of data sets allows for the robustness of the estimation algorithms to be tested. The three data sets taken from orbiting satellites represent the most realistic data. Fortunately, these sets use different configurations of receivers and antenna types and are from multiple attitude orientations. Data taken on the ground allow for the testing of a wider range of receivers and antenna combinations. Furthermore, the collection of data using the TANS Vector on the ground, permits the testing of a ground calibration set in conjunction with the CRISTA-SPAS orbit data.

Analysis of the off-boresight angle versus SNR relationships is further studied in the next chapter. The value of  $\Delta p$  along with other factors is shown to be a good indicator of the estimation performance.

The test statistic,  $\tau$ , shows that the  $\alpha$  versus SNR relationship is approximately symmetrically distributed in the SNR bins of the various data sets. In the next chapter, results are given for an MLE based estimation of the antenna boresight vector involving these data sets.

## CHAPTER 7

### SNR BASED SINGLE-AXIS ESTIMATION: MLE RESULTS

#### 7.1 Introduction

In this chapter results are shown for the estimation of a single antenna boresight vector using the MLE algorithm developed in Chapter 5 applied to the data sets described in the previous chapter. The accuracies range from 3.0 to 10.5 deg (RMS) for the reference results and 4.4 to 11.1 deg (RMS) for results using various mapping function sources. These values are then analyzed according to a number of performance factors. The most important are shown to be the quality of the mapping function and the number of visible measurements per epoch. Based on the performance demonstrated from all of the data sets, this method is predicted to have a RMS error of under 7 deg for a high quality antenna and receiver with an average visibility of 5 or more satellites.

The best results are from the GANE satellite data which had a choke ring antenna. The choke ring contributes to a good mapping function. The NovAtel results benefit by the 12 channel tracking capability of the receiver and also show improvement with the use of a choke ring antenna. The worst results are from the GPS/MET satellite. Analysis of these results is hindered by a poor truth reference.

## 7.2 Reference Results

Access to known attitude data for these tests allow for the determination of the true GPS antenna boresights. First, the attitude information is used to rotate the LOS vectors,  $\hat{\mathbf{e}}^L$ , recorded in the local frame at each epoch, to the vehicle body frame,  $\hat{\mathbf{e}}^B$ . These vectors are collected together for a batch solution of the boresight alignment in the body frame,  $\hat{\mathbf{n}}^B$ , as detailed in Section 4.9. Next, the attitude data are used to rotate  $\hat{\mathbf{n}}^B$  to  $\hat{\mathbf{n}}^L$  at each epoch. Finally, the corresponding  $\alpha$  values are calculated from the angles between  $\hat{\mathbf{n}}^L$  and  $\hat{\mathbf{e}}^L$  from which a mapping function is generated. The mapping functions for each satellite and antenna combination are shown in Figures 7.1 through 7.6.

The computed alignments for each data set are shown in Table 7.1. It is expected that the estimated alignments between the space-based data sets for each receiver should be the same. The ground sets are not expected to be equal to each other because the mounting conditions are different for each antenna. The alignments for the two CRISTA-SPAS sets are within 2.3 deg of each other. The GPS/MET alignments are all within 2.6 deg. The two GANE alignments, however, are over 10 deg apart. After combining the two data sets, the computed alignment agrees to within 0.7 deg of the bore-sight estimated with just the GANE #1 set. Considering the fact that the GANE #2 set covers a larger range of angles with fewer data points than the GANE #1 set, the results suggest that there may not be sufficient data for an accurate alignment calibration from just the GANE #2 set.

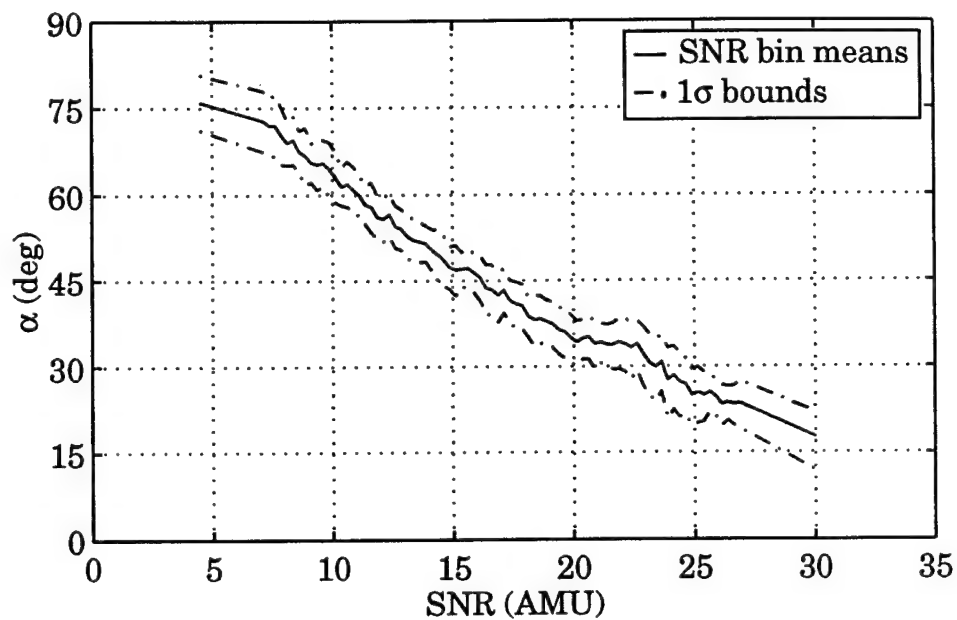


Figure 7.1 GANE mapping function.

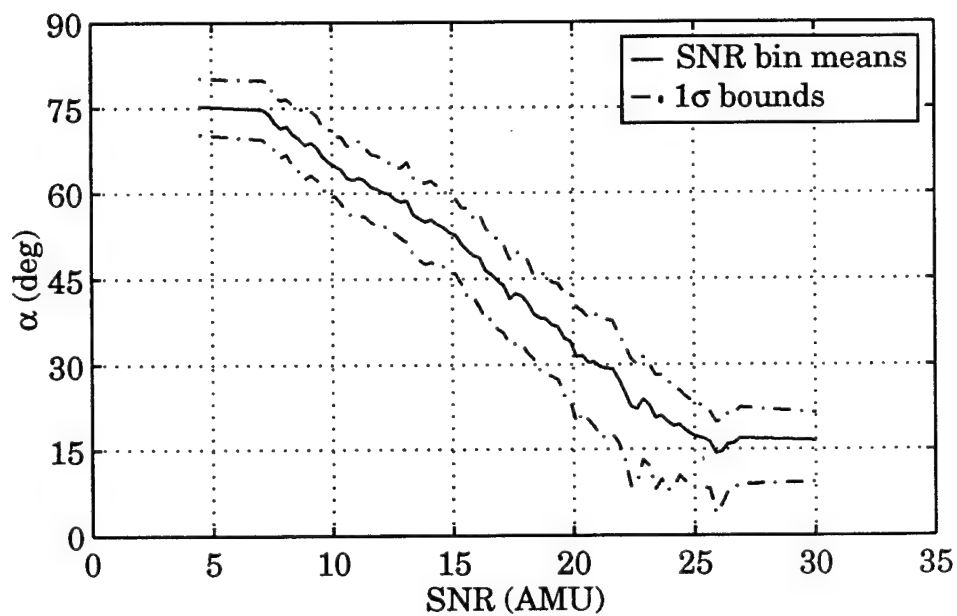


Figure 7.2 CRISTA-SPAS mapping function.



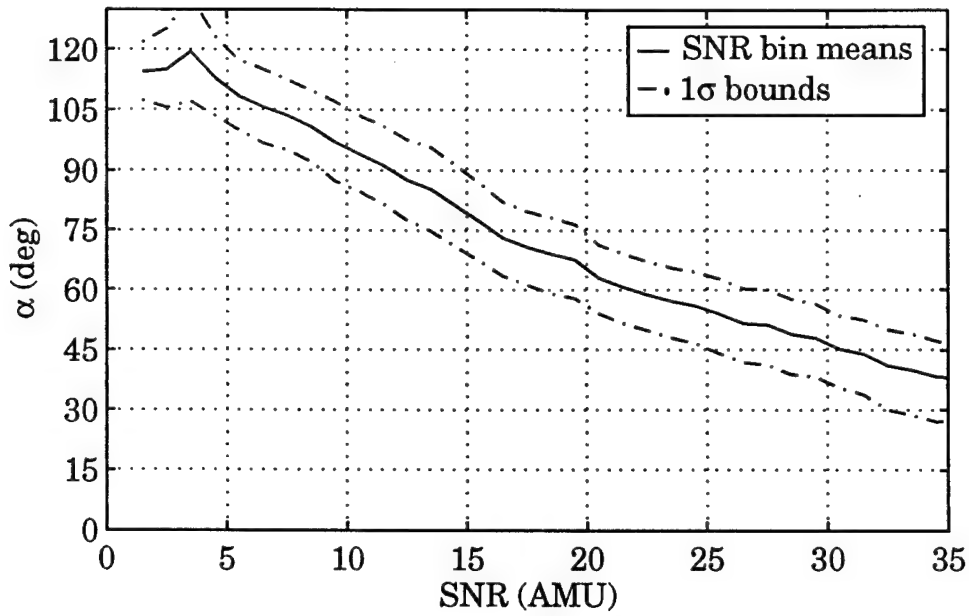


Figure 7.3 GPS/MET mapping function.

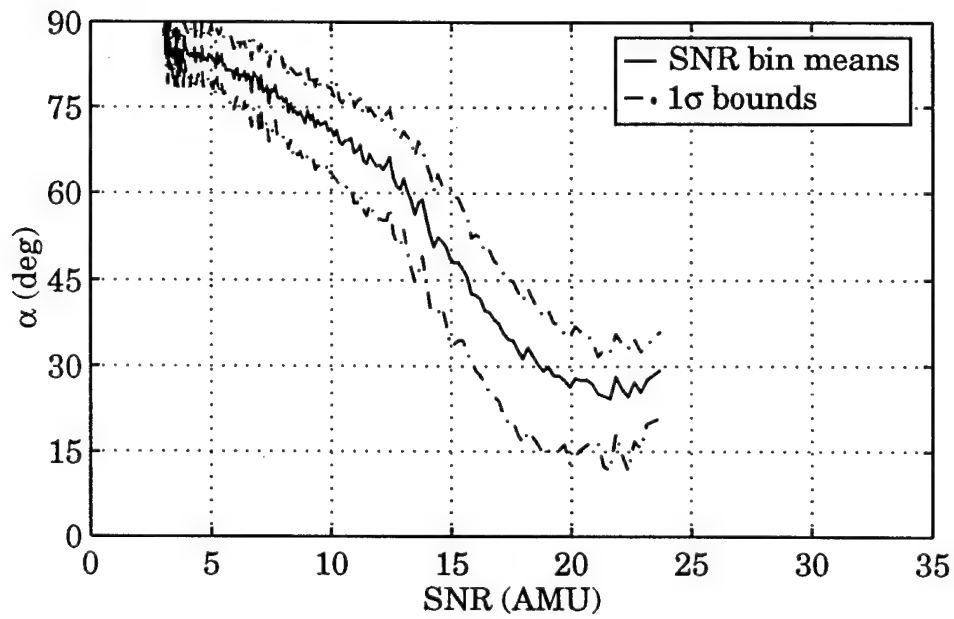


Figure 7.4 NovAtel mapping function (NovAtel antenna).

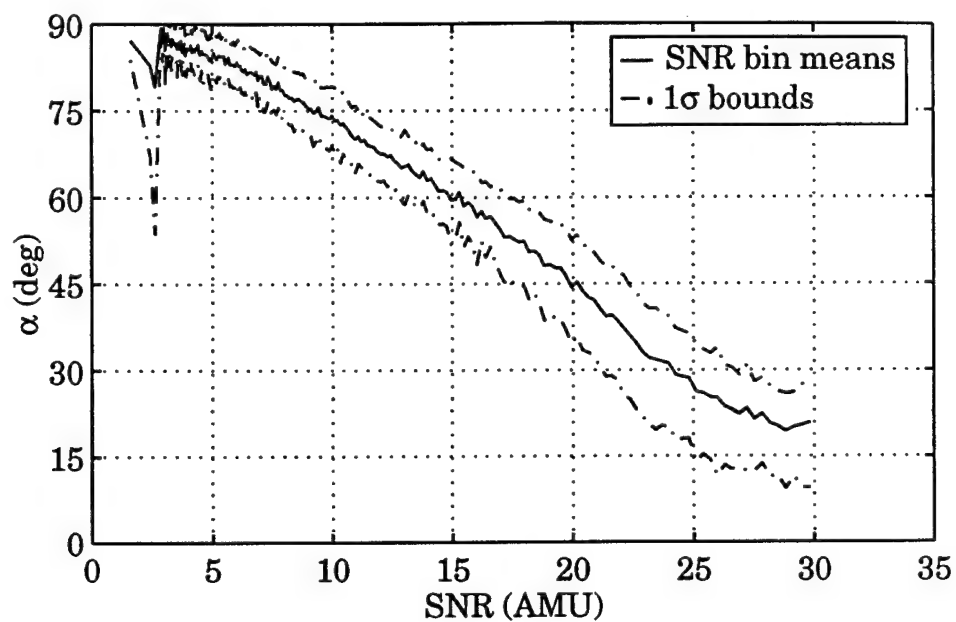


Figure 7.5 NovAtel mapping function (Ashtech antenna).

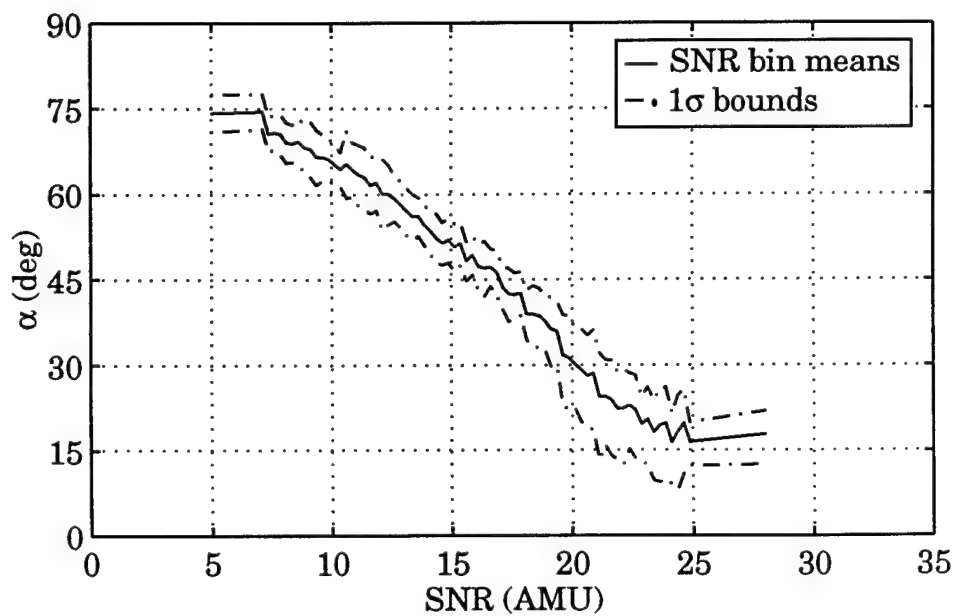


Figure 7.6 Ground TANS mapping function.

Table 7.1. Boresight Alignment.

Data Set	boresight coordinates in the body frame, $\hat{\mathbf{n}}^B$		
	x	y	z
GANE #1	0.0113	-0.0213	0.9997
GANE #2	-0.0406	0.1496	0.9879
GANE #1 and #2	0.0157	-0.0093	0.9998
CRISTA-SPAS #1	-0.9940	0.0810	-0.0731
CRISTA-SPAS #2	-0.9939	0.0505	-0.0984
GPS/MET #1	0.9964	-0.0136	-0.0842
GPS/MET #2	0.9915	-0.0277	-0.1272
GPS/MET #3	0.9949	-0.0152	-0.0996
Ground TANS	0.0282	0.0129	0.9995
NovAtel #1 (NovAtel)	-0.0062	-0.0658	0.9978
NovAtel #2 (Ashtech)	0.0051	-0.0095	0.9999
NovAtel #3 (TANS)	0.0636	-0.0166	0.9978
NovAtel #4 (NovAtel)	-0.0362	-0.0188	0.9992

The MLE solution, as described in Chapter 5, is used to estimate a new  $\hat{\mathbf{n}}$  at each measurement epoch. Table 7.2 shows the RMS error, maximum error, and the 90th percentile error for each data set described in the last chapter. For these results the same data used to create the reference calibration are used to estimate  $\hat{\mathbf{n}}$ . Figures 7.7 through 7.10 show the estimation errors as a function of time for four of the data sets, one each from GANE, CRISTA-SPAS, GPS/MET, and the NovAtel ground sets. Each solution is based upon a single measurement epoch.

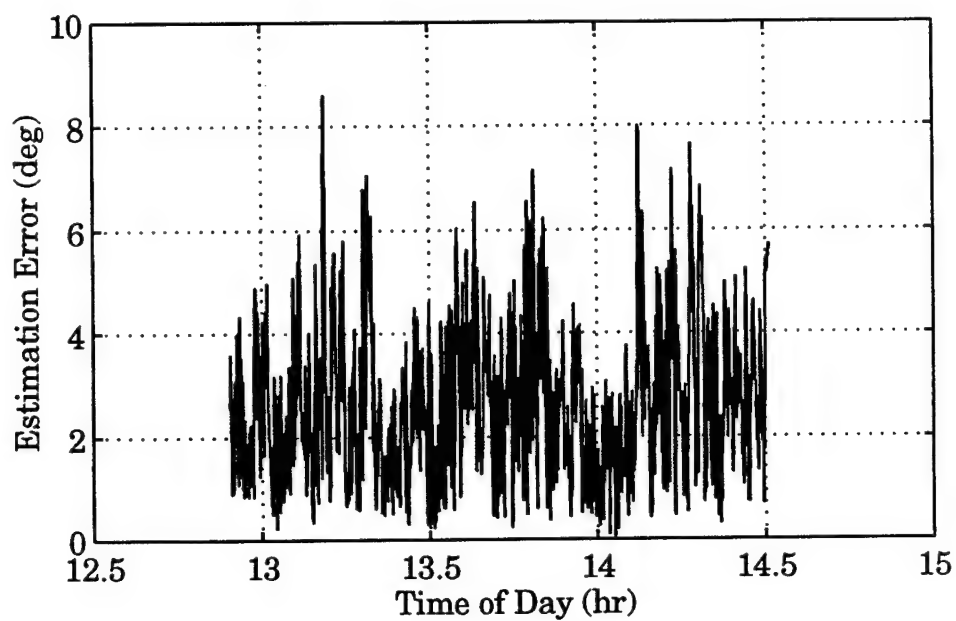


Figure 7.7 GANE #1 estimation error history.

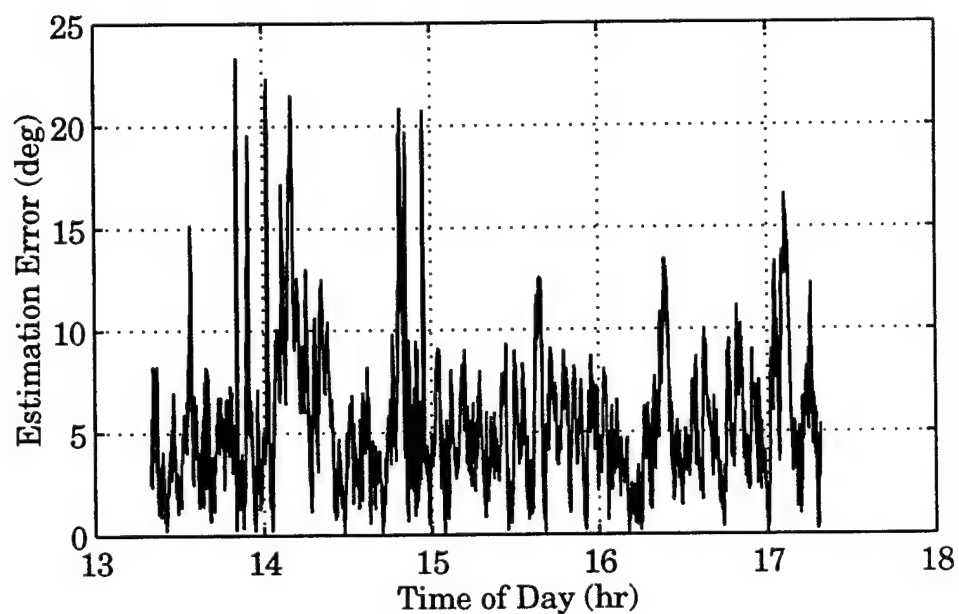


Figure 7.8 CRISTA-SPAS estimation error history.

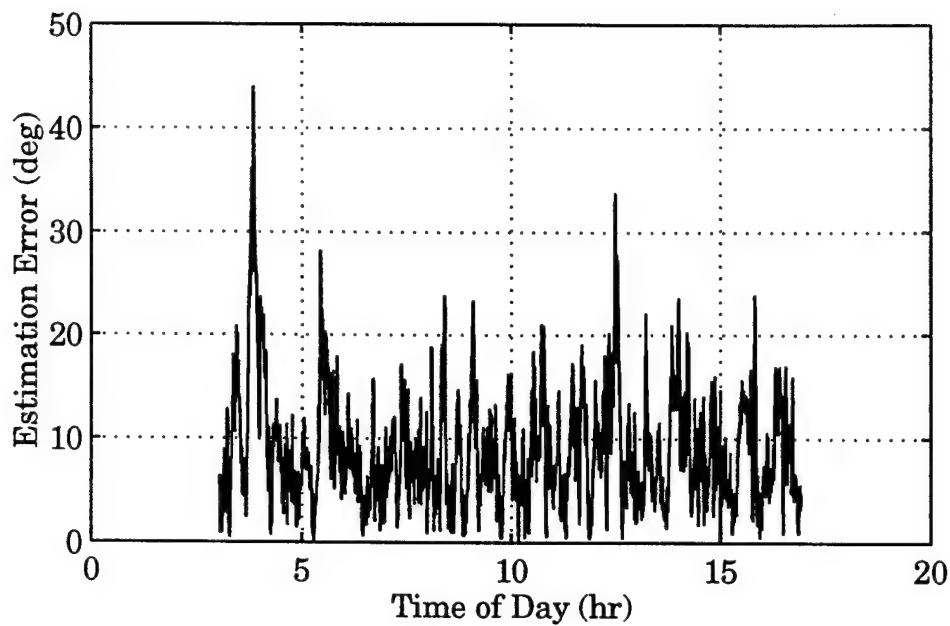


Figure 7.9 GPS/MET #1 estimation error history.

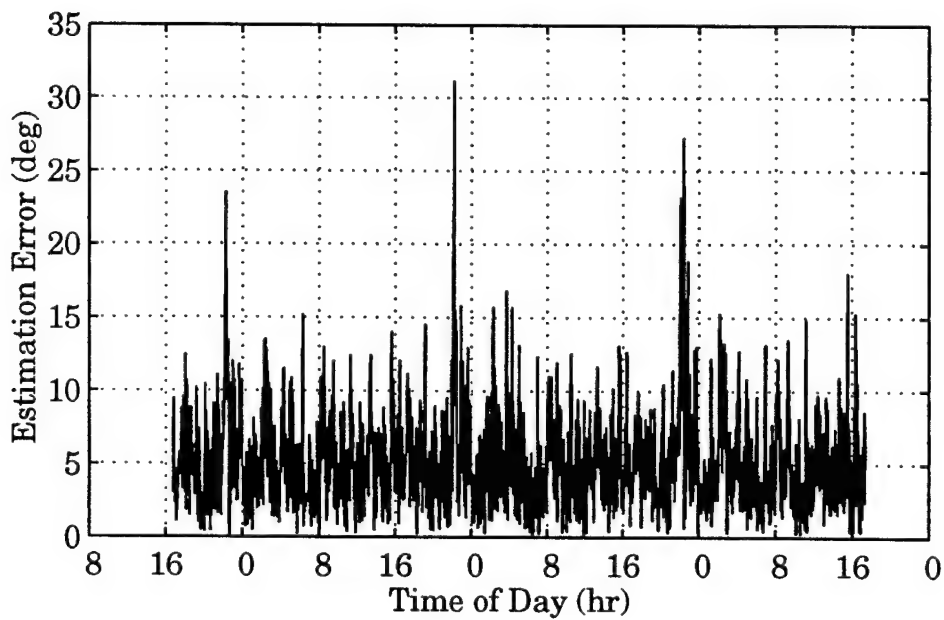


Figure 7.10 NovAtel #1 estimation error history.

Table 7.2. Estimation Results with Reference.

Data Set	RMS Error (deg)	90% Error (deg)	Max. Error (deg)
GANE #1	3.0	4.7	8.6
GANE #2	5.9	8.5	23.9
CRISTA-SPAS #1	6.4	9.5	23.1
CRISTA-SPAS #2	7.1	10.8	21.2
GPS/MET #1	10.5	15.9	43.9
GPS/MET #2	10.4	15.8	52.6
GPS/MET #3	10.0	15.4	52.6
Ground TANS	4.8	7.7	15.2
NovAtel #1	6.1	9.4	31.1
NovAtel #2	4.3	6.4	30.2
NovAtel #3	6.0	8.9	45.0
NovAtel #4	6.1	9.2	20.8

The results for GANE #1 are clearly the best. Not only is the RMS error under 4 deg but the maximum error is under 9 deg. NovAtel #2, which uses an Ashtech choke ring antenna, is the second best data set in terms of RMS error, but it has a large maximum error. The 90th percentile errors follow the same trend as the RMS errors. Recall from Chapter 5 that the NovAtel #1 and #3 sets use a NovAtel patch and Trimble patch antenna, respectively. A comparison between their results shows no significant difference between their performances. The Ground TANS set, which is taken in exactly the same environment as the NovAtel sets and uses the Trimble patch antenna, produces results that are almost as good as the NovAtel set taken with the choke ring antenna. All of the data sets, with the exception of

GANES #1, exhibit spikes in the error plots. The maximum errors occur at these spikes. The largest spikes, as evident in both the GPS/MET and NovAtel plots, are significantly larger than the general trend of the errors. Since the NovAtel data is taken on the ground and consists of several days worth of measurements, a repetition of the test conditions occurs. The spikes are shown to be repeated at the time of each day when the satellite geometry is identical. Further analysis for the causes of these bad points is given in Section 7.5 where the performance factors are discussed.

In Table 7.3 the estimate of  $\hat{n}$  is equal to the initial estimate,  $\hat{n}_0$ , of the gradient search as given by Equation (5.10). The RMS errors for most of the data sets are within 0.3 deg of the Table 7.2 results. The GANE #2 results, however, are significantly larger. The GANE #2 set has the lowest average number of satellites in view with 3.8 compared to over 5.4 for the other sets. This suggests that the gradient search is only useful when the number of measurements is small. For a large number of measurements, the normalized result of the weighted least squares solution is sufficient. The GPS/MET results, on the other hand, are up to 0.9 deg smaller. This discrepancy may be caused by the poor truth reference.

### 7.3 Results for Specific Mapping Function Sources

In Table 7.4 the data used to estimate  $\hat{n}$  are independent of the data used to generate the calibration function. The GANE data are evaluated with both a gain pattern mapping function and by using an alternate set of calibration data. The CRISTA-SPAS data are evaluated with a gain pattern function, a ground based calibration function, and an alternate space based generated function. The GPS/MET data is tested on calibration

Table 7.3. Estimation Results with Reference using  $\hat{n}_0$ .

Data Set	RMS Error (deg)	90% Error (deg)	Max. Error (deg)
GANE #1	3.2	4.7	21.4
GANE #2	8.7	8.7	71.6
CRISTA-SPAS #1	6.2	9.5	20.5
CRISTA-SPAS #2	7.1	10.8	17.0
GPS/MET #1	9.9	15.1	32.7
GPS/MET #2	9.3	14.1	52.5
GPS/MET #3	9.7	14.9	48.8
Ground TANS	5.0	7.5	22.7
NovAtel #1	6.1	9.4	25.1
NovAtel #2	4.2	6.4	21.5
NovAtel #3	5.7	8.6	33.8
NovAtel #4	6.0	9.1	18.5

functions created from alternate data. The NovAtel data is used to test the variability of the mapping functions over an extended time period. To accomplish this, the mapping function generated from NovAtel #1 data, collected over two months before NovAtel #4, is used in conjunction with this later set. Listed to the right of the error values are the differences from the results in Table 7.2.

In all of the cases, both the RMS errors and the 90th percentile errors increase over the reference results. However, the absolute increases, are not very large. They ranged from 0.1 deg to 2.0 deg for the RMS errors and 0.6 deg to 2.9 deg for the 90th percentile errors. The GANE #1 data set is the most sensitive to the change in the mapping func-



Table 7.4. Estimation Results with Various Mapping Functions.

Data Set	RMS Error ( $\Delta$ ) (deg)	90% Error ( $\Delta$ ) (deg)	Max. Error ( $\Delta$ ) (deg)
GANE #1 w/ gain pattern	4.6 (+1.6)	7.3 (+2.6)	11.7 (+3.1)
GANE #1 w/ GANE #2 data	5.0 (+2.0)	7.6 (+2.9)	17.6 (+9.0)
GANE #2 w/ gain pattern	7.4 (+1.5)	10.8 (+2.3)	25.4 (+1.5)
CRISTA-SPAS #1 w/ gain pattern	6.6 (+0.2)	9.7 (+0.2)	27.4 (+4.3)
CRISTA-SPAS #1 w/ ground data	7.2 (+0.8)	10.8 (+1.3)	24.3 (+1.2)
CRISTA-SPAS #2 w/ CRISTA- SPAS #1 data	7.7 (+0.6)	11.6 (+0.8)	22.3 (+1.1)
GPS/MET #3 w/ GPS/MET #1 data	10.7 (+0.7)	10.7 (+0.7)	63.2 (+10.6)
GPS/MET #1 w/ GPS/MET #3 data	11.1 (+0.6)	16.6 (+0.7)	42.0 (-1.9)
Ground TANS w/ CRISTA-SPAS #1 data	5.9 (+1.1)	9.5 (+1.8)	17.2 (+2.0)
NovAtel #4 w/ NovAtel #1 data	7.0 (+0.9)	10.9 (+1.4)	32.0 (12.8)
NovAtel #2 w/ gain pattern	4.4 (+0.1)	6.5 (+0.1)	22.2 (-8.0)

tion, while the GPS/MET sets are the least sensitive. This is possibly due to the GANE #1 data having the best data quality, and as a result, is more sensitive to small changes in the calibration function. GPS/MET, on the other hand, has the worst data quality and as a result, is not sensitive to small changes in the calibration function. The use of gain pattern based

mapping functions works as well as the use of alternate calibration data. The maximum errors fluctuated unpredictably from a drop of more than 15 deg to an increase of over 12 deg.

#### **7.4 CRISTA-SPAS Results using Individual Satellite Mapping Functions**

Analysis of the plots presented in Section 4.7 shows that there is no significant difference between a mapping function based on all of the GPS satellites and functions based on individual ones. Table 7.4 presents results for the CRISTA-SPAS satellite demonstrating this. The individual mapping functions are generated from the CRISTA-SPAS #1 set. When compared to the single mapping function reference results, the reference results based on individual functions are significantly better. This is expected because the individual satellites functions are based on a much smaller range of data. As a result, each SNR and  $\alpha$  pair are very closely correlated with the average used in the specific function. However, this is not the case for the values in the CRISTA-SPAS #2 set. The results when using the single mapping function from the CRISTA-SPAS #1 set are clearly superior.

#### **7.5 Performance Factors**

The results shown in the previous sections illustrate the effect of mapping function errors on the achievable accuracy. Other factors which affect the performance are the quality of SNR data as measured by its  $\Delta p$  value and the choice of SNR bin size. These factors are governed by the data processing technique. Additionally, the performance is affected by the total number of satellites tracked and the computed PDOP value which are both independent of the processing technique.

Table 7.5. Estimation Results with Individual Mapping Functions.

Data Set	RMS Error ( $\Delta$ ) (deg)	90% Error ( $\Delta$ ) (deg)	Max. Error ( $\Delta$ ) (deg)
CRISTA-SPAS #1 w/ single mapping function (reference results)	6.4	9.5	23.1
CRISTA-SPAS #1 w/ individual satellite mapping functions (reference results)	4.7	7.3	18.8
CRISTA-SPAS #2 w/ single mapping function from CRISTA- SPAS #1	7.7	11.6	22.3
CRISTA-SPAS #2 w/ individual satellite mapping functions from CRISTA-SPAS #1	11.3	16.6	73.3

Table 7.6 lists the quality statistics for each data set. A comparison of the data quality statistics and the estimation results in Tables 7.2 and 7.4 yields some interesting insights. The two GANE data sets have similar measurement error distributions as evidenced by the  $\Delta\rho$  values, but significantly different satellite visibilities (mean of 5.4 to 3.8 satellites). The resulting RMS attitude errors are 3.0 and 6.4 deg for GANE #1 and GANE #2, respectively. CRISTA-SPAS #1 has about the same mean number of satellites as GANE #1, but the measurement error factor  $\Delta\rho$  is 7.1 as compared to 3.8 for GANE #1. The resulting RMS attitude error for CRISTA-SPAS #1 is 6.4 deg. The NovAtel sets have relatively poor mapping functions. However, the ability of the receiver to track up to 12 satellites greatly enhances the satellite visibility and consequently the attitude

Table 7.6. Quality of Data

Data Set	$\Delta p$ (deg)	Mean # of Sats	Mean PDOP
GA NE #1	3.8	5.4	2.3
GA NE #2	4.3	3.8	32.0
CRISTA-SPAS #1	7.1	5.8	2.2
CRISTA-SPAS #2	7.3	5.6	2.4
GPS/MET #1	9.4	7.4	1.5
GPS/MET #2	10.4	7.3	1.8
GPS/MET #3	9.3	6.9	2.1
Ground TANS	5.8	5.8	2.2
NovAtel #1	10.0	8.2	1.2
NovAtel #2	7.7	8.2	1.2
NovAtel #3	10.0	8.2	1.3
NovAtel #4	9.9	7.9	1.3

estimation performance. The GPS/MET data have quality that is similar to the NovAtel sets. The satellite visibility, on the other hand, averages to about 1 fewer satellites per measurement epoch. As a result, the consequences of poor data quality are not mitigated as well.

Tables 7.7 through 7.10 show a break down of the estimation errors versus the number of satellites in view for the combined GANE data sets, CRISTA-SPAS #1, GPS/MET #1, and NovAtel #1, respectively. To generate the results, solutions are formed using only the specified number of satellites. The first  $m$  satellites are selected rather than choosing them based on a geometrical constraint. This is repeated over the possible range of satellite visibilities.

Table 7.7. Visibility Dependence for GANE #1 and #2

Data Statistic	Number of Satellites			
	3	4	5	6
RMS Error (deg)	7.0	3.3	3.2	2.9
90% Error (deg)	6.8	5.3	4.8	4.4
Max. Error (deg)	68.4	10.4	8.6	8.0

Table 7.8. Visibility Dependence for CRISTA-SPAS #1

Data Statistic	Number of Satellites			
	3	4	5	6
RMS Error (deg)	13.8	10.4	6.9	5.6
90% Error (deg)	20.8	13.9	10.5	8.3
Max. Error (deg)	70.4	84.4	23.8	20.6

In every data set and for each one of the computed statistics, the errors decrease as more satellites are used. The largest decrease over the span of visibility conditions occur with the data sets having the worst data quality. The largest decreases occur in the GANE and CRISTA-SPAS sets

Table 7.9. Visibility Dependence for GPS/MET #1

Data Statistic	Number of Satellites			
	5	6	7	8
RMS Error (deg)	11.9	11.2	10.3	9.6
90% Error (deg)	18.4	17.1	16.0	14.8
Max. Error (deg)	42.0	43.9	37.1	32.5

Table 7.10. Visibility Dependence for NovAtel #1

Data Statistic	Number of Satellites						
	5	6	7	8	9	10	11
RMS Error (deg)	9.0	8.4	7.5	6.5	6.2	6.0	4.5
90% Error (deg)	13.3	12.7	11.4	10.0	9.6	8.7	3.8
Max. Error (deg)	57.9	38.4	33.5	19.0	16.7	13.0	5.9

when the visibility is increased from 3 to 4 satellites. The visibility dependences clearly show the advantage of a multichannel receiver with the capability of tracking a large number of satellites, especially when the quality of the mapping function is poor.

Figures 7.11 through 7.14 are scatter plots showing the relationship between the estimation error and PDOP value. In Figure 7.11, the PDOP's that are greater than 16 are grouped together for better resolution in the graph. None of the plots demonstrate a strong correlation between these two values. The errors from the GANE data are all under 20 deg except when the PDOP is larger than 16. The CRISTA-SPAS data shows a small increase in the maximum errors when the PDOP is over 3. The largest NovAtel errors occur for PDOP's greater than 1.7. GPS/MET has the least

PDOP dependence of the analyzed data sets. In all cases, however, a large PDOP does not guarantee a large estimation error. Each data sets demonstrates instances of low errors with a much higher than average PDOP. While it might be expected that large PDOP's, indicating poor geometry, would be a major contributor to poor estimation, the data does not demonstrate this.

Figures 7.15 and 7.16 show the dependence on SNR bin resolution for the NovAtel and TANS Vector receivers, respectively. For both receivers the RMS errors show a slight but steady increase as the bin size gets larger. The maximum errors generally increase with bin size but there is some fluctuation. In both cases, an extremely small bin size is not dramatically beneficial, but does show some improvement. It was thought that SNR variations produced by multipath would indicate a larger bin size; however, experimental results do not bear this out. Since the mapping functions are generated prior to estimation, there is no reason on the basis of computational speed to use larger bin sizes.

## 7.6 Estimation Performance vs. Computed Error Bounds

In Section 5.4.3 Equations (5.21) and (5.22) are derived, giving a means by which the expected errors for the two boresight angles are determined at each epoch. These values correspond to a prediction of the actual error to a  $1\sigma$  level of certainty. In other words, it is expected that about 67% of the angle errors,  $\delta\theta$  and  $\delta\phi$ , computed for the reference results will be less than or equal to these predicted values at a given epoch.

Table 7.11 shows a comparison of the actual angle errors to the predicted errors. The predicted error bounds generally agree to within  $1\sigma$  of

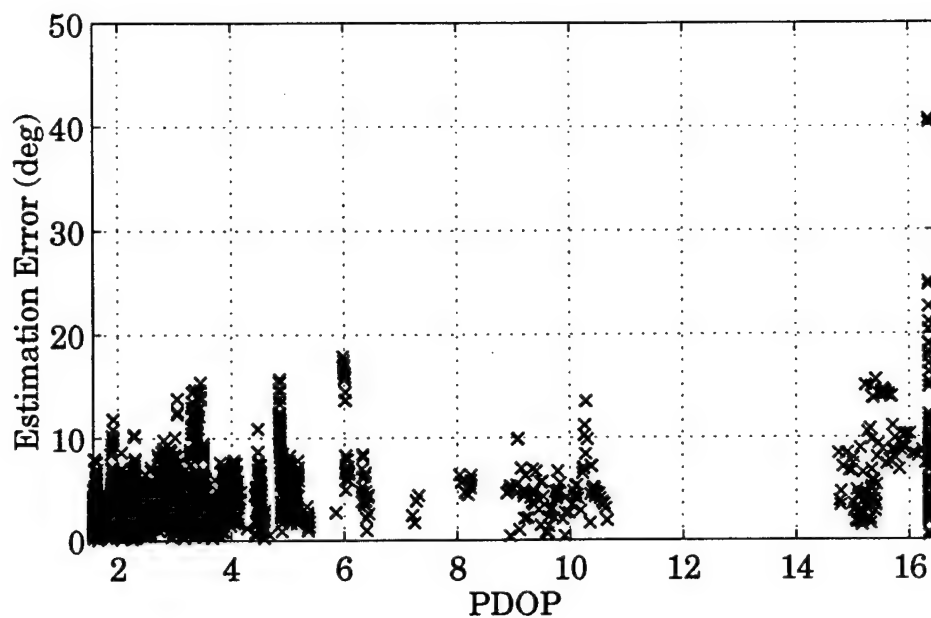


Figure 7.11 GANE #1 and #2 PDOP dependence.

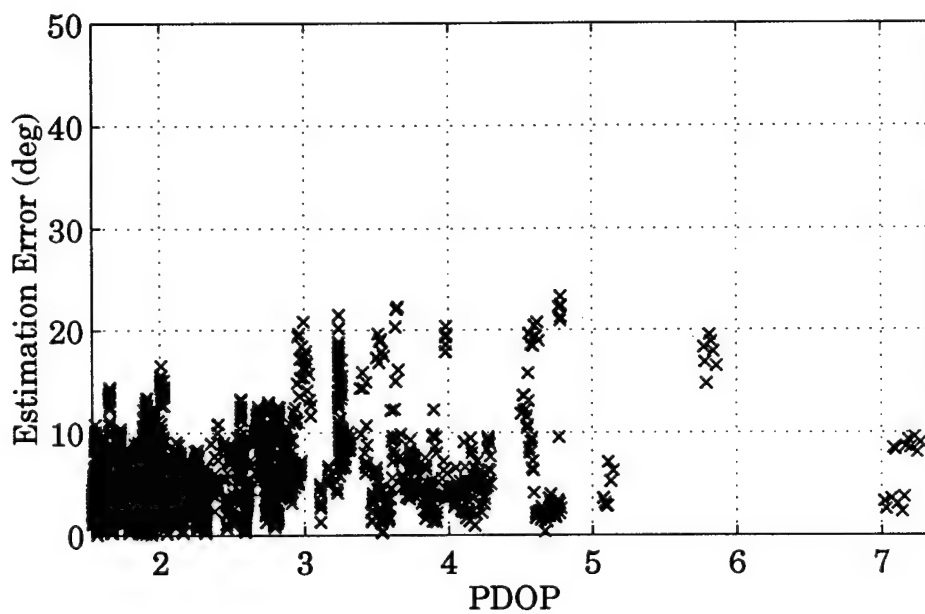


Figure 7.12 CRISTA-SPAS #1 and #2 PDOP dependence.



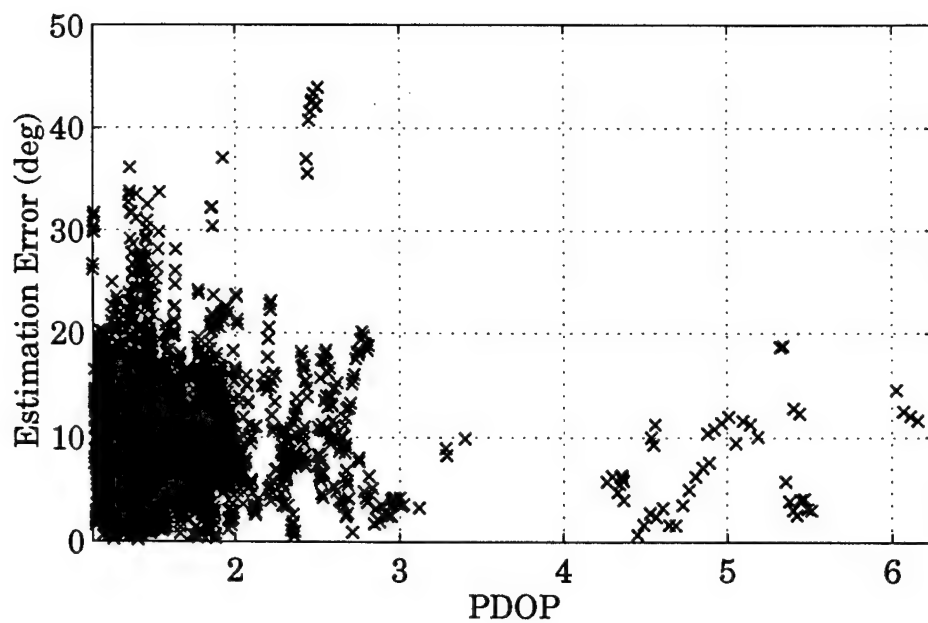


Figure 7.13 GPS/MET #1 and #3 PDOP dependence.

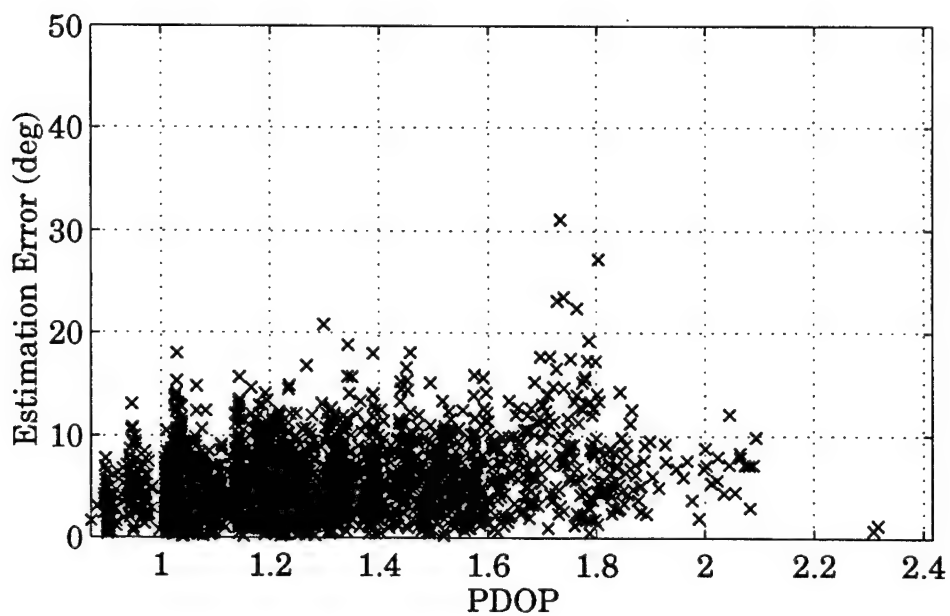


Figure 7.14 NovAtel #1 and #4 PDOP dependence.

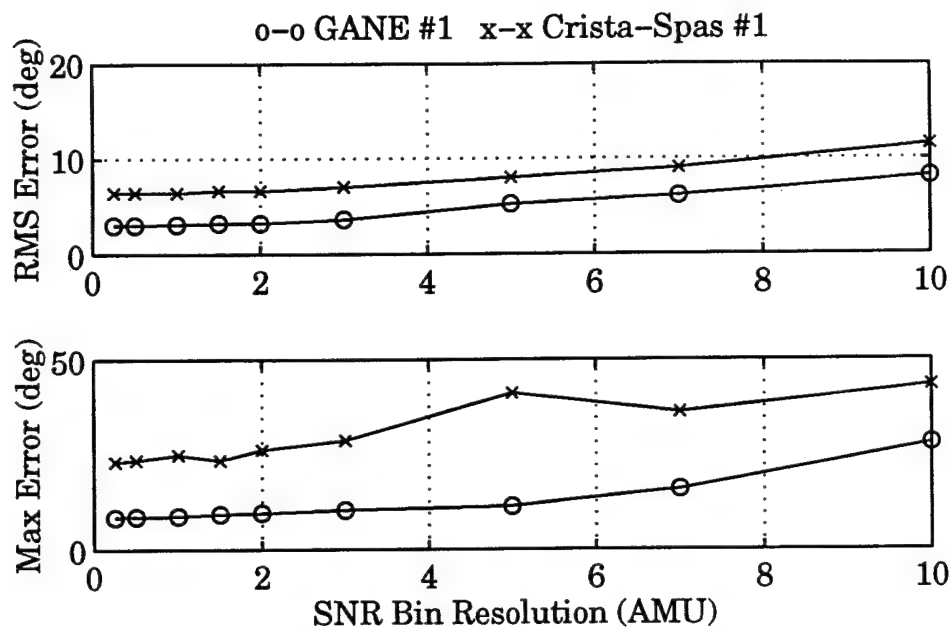


Figure 7.15 SNR bin resolution dependence for GANE and CRISTA-SPAS #1.

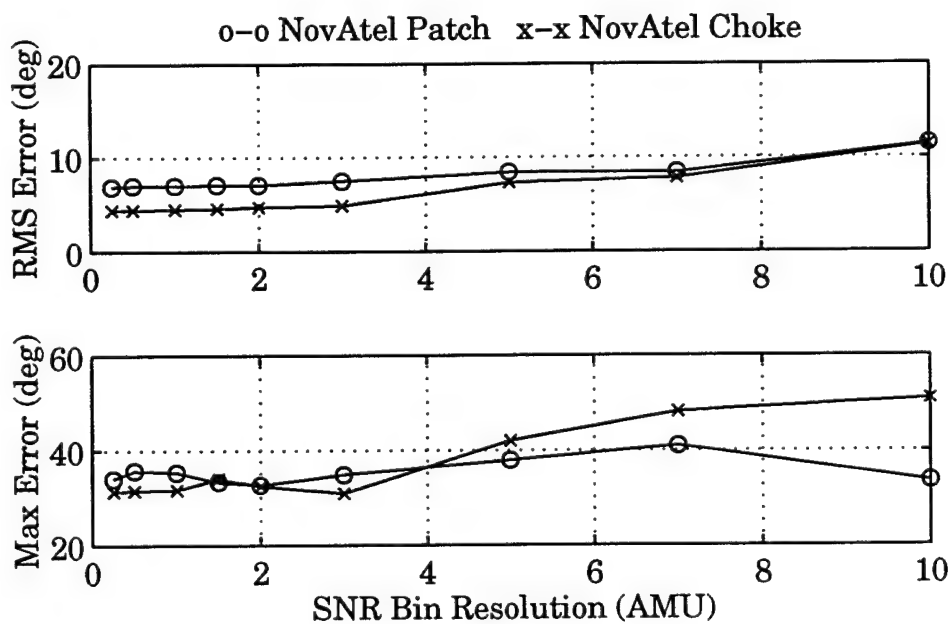


Figure 7.16 SNR bin resolution dependence for NovAtel #1 and #2.

Table 7.11. Comparison of Actual Errors to Predicted Errors

Data Set	RMS Error (deg)	% of $\delta\theta$ 's within predicted bounds	% of $\delta\phi$ 's within predicted bounds
GANE #1	3.0	67	76
GANE #2	6.4	66	63
CRISTA-SPAS #1	6.4	69	72
CRISTA-SPAS #2	7.1	60	70
GPS/MET #1	10.5	59	49
GPS/MET #2	10.4	57	58
GPS/MET #3	10.0	59	56
Ground TANS	4.8	64	63
NovAtel #1	6.1	73	63
NovAtel #2	4.3	68	73
NovAtel #3	5.9	68	73
NovAtel #4	6.1	72	71

the actual errors. The data sets with the smallest errors, GANE #1, CRISTA-SPAS #1, and NovAtel #2, show the best agreement. The biggest exception is with the GPS/MET data which shows a much smaller percentage of estimates, as low as 49%, within the bounds. One possible reason for this discrepancy is that the GPS/MET data is analyzed using a poor truth reference, implying that the mapping function errors are likely to be correlated or non-Gaussian.

## 7.7 Conclusions

This chapter has presented the results for an MLE based approach to estimate a single axis of attitude using the SNR measurements from a single GPS antenna. This method is based upon an empirical mapping of

the angle between the GPS antenna off-boresight angle and the SNR measurement of the GPS signal. The RMS of the estimation errors range from 3.0 to 10.5 deg, the 90th percentile errors range from 4.7 to 15.9 deg, and the maximum errors range between 8.6 and 52.6 deg. The best results occur when there is a good mapping function quantified by the mean residual value and when there are 6 or more satellites in view. The best results are from GANE #1 that uses an antenna and choke ring combination and is in an orientation that allows for high visibility. The second best results are from NovAtel #2 that also uses an antenna and choke ring combination. While the mean residual value of the NovAtel mapping functions are not as good as the ones for the GANE data sets, the receiver's ability to track up to 12 satellites at once allows for a significantly greater mean number of satellites in view. The worst results are from the GPS/MET satellite. The data sets have a relatively good visibility, but their mapping functions are among the worst of all the sets. Analysis of these sets is hindered by a lack of a good truth reference. Without a good reference, the calibration functions are degraded and the computed errors are not accurate.

As expected, the estimation performance is degraded when the source of calibration data is not the actual data being used. However, the largest increase in the RMS error is only 2 deg and the largest increase in the 90th percentile error is 2.9. The gain pattern based mapping functions work as well as calibration data based ones.

The analysis of the performance factors clearly show that the quality of the mapping function as given by its  $\Delta\rho$  value and the number of sat-

ellites being used are the two best indicators of performance. There is only a slight indication that PDOP has a noticeable effect.

The results demonstrated in this research show that this method has the potential for coarse single attitude estimation to a level of 5 to 10 deg with one antenna. The use of various calibration sources and the satisfactory estimation results indicate that the technique can be practically implemented. In particular it would be useful in the role of emergency backup or integer ambiguity resolution.

## CHAPTER 8

### SUMMARY

Two sets of techniques have been presented in this research that use GPS information for spacecraft attitude estimation. In particular, these methods are designed to meet the criteria of low cost satellite missions. The first set of methods, based on GPS carrier phase data, can only be applied to satellites using spin stabilization. The second set of methods, based on GPS SNR data, can be used for any type of satellite stabilization.

The carrier phase approach is based on the phase differences between two antenna mounted on one face of a spinning satellite. Because the antennas experience large changes in position in a short time span, the measurements can be differenced in time for the computation of a displacement vector observable. This calculation is not significantly affected by the carrier phase integer ambiguity. As a result, it is not computationally intensive and is not hindered by cycle slips.

Both the satellite frequency and attitude information are extracted from the displacement vectors. The frequencies are determined by the AR and FFT frequency domain methods and a time domain technique that is based on the average of the displacement vectors. The AR method is the most accurate of the three. For a batch of measurements spanning a minute, it produces estimates to within 0.03 rpm for a 5 rpm satellite. After five minutes the error is under 0.01 rpm. The orientation of the sat-

ellite angular momentum vector is estimated by a batch filter and an averaging technique using the cross products of the displacement vectors. Both the cross product and batch filter techniques produce pointing errors of under 0.25 deg. In addition, the batch filter estimates the nutation angle to within 0.2 deg and the phase angles to within 2 deg.

The SNR-based approaches estimate the antenna boresight vector by using the relationship between the SNR of a GPS measurement and the corresponding angle  $\alpha$ . The  $\alpha$ 's are between the boresight and the LOS vectors. Because of the variations in the antenna gain patterns, the SNR is highest at small  $\alpha$ 's and decreases as  $\alpha$  increases. A techniques has been presented using this relationship. It computes the boresight vector using a maximum likelihood estimation (MLE).

The MLE method requires the creation of a mapping function between SNR measurements and the corresponding  $\alpha$ 's. This is formed by either using a calibration data set from SNR's taken at known  $\alpha$ 's or by using a gain pattern measurement scaled by the receiver SNR limits. The calibration approach has the advantage of using data that is more similar to the actual estimation data, while the gain pattern approach has the advantage of requiring less initialization data. After the mapping functions are created, axis estimates at each epoch are formed using the LOS vectors, the  $\alpha$  values mapped from each of the SNR measurements, and the weights assigned to the  $\alpha$  values.

The SNR vs.  $\alpha$  relationship is affected by a number of influences. Two of these, the space loss and gain pattern of the GPS transmitting antenna, are adjusted for by knowing the satellite positions. Power fluctuations among GPS satellites do not produce a significant effect. Multipath

causes the largest fluctuations in the relationship. This effect is treated as measurement noise.

The MLE method has been applied to a variety of data, including both ground and space sources. The best result of 3.0 deg (RMS) is from the GANE satellite. The worst result of 10.5 deg (RMS) is from the GPS/MET satellite. The results show that two factors contribute most significantly to the performance of the technique. The first is the quality of the SNR data. A good quality consists of a small potential range of  $\alpha$ 's for each SNR value. Choke ring antennas have the best quality. The second is the number of satellites in view. The RMS error is lower when more satellites are tracked.

The results of this research show that GPS is applicable for attitude determination in a number of ways. The carrier phase approach allows for its use on spinning satellites when very good accuracy is required. For missions with a requirement of only coarse attitude knowledge, the SNR technique is applicable and easily applied. It can also be used for initialization of more precise instruments or as an emergency backup. Its biggest advantage is that it does not need a specialized attitude receiver. If a GPS navigation receiver is on-board, then SNR-based attitude estimation can take place.

There are some important areas where this research can be expanded in the future. The phase-based method needs to be evaluated on spacecraft data. Its performance should be evaluated in terms of the estimation and control requirements of an actual spinning satellite mission. Additional data is also needed for the SNR-based method. Measurements need to be collected for a two antenna configuration on a three-axis satel-



lite. The future SNOE satellite mission might provide the necessary data to evaluate this technique on a spinning satellite with the antenna mounted on the side of the spacecraft. Finally, the performance of the SNR-based method should be compared in more detail with the requirements of various ambiguity resolutions techniques.

## BIBLIOGRAPHY

- [ASUSAT 1] ASUSAT 1, Arizona State University, <http://www.eas.asu.edu/~nasasg/asusat/>.
- [Axelrad and Brown, 1996] Axelrad, P. and Brown, R.G., "Attitude Determination," in *Global Positioning System: Theory and Applications Vol. I*, edited by Parkinson et al., Vol. 164, Progress in Astronautics and Aeronautics, AIAA, New York, 1996, pp. 409-434.
- [Axelrad and Chesley, 1993] Axelrad, P. and Chesley, B.C. "Performance Testing of a GPS Based Attitude Determination System," Proceedings of the AIAA Guidance, Navigation, and Control Conference, Monterey, CA, AIAA, Washington, DC, 1993, pp. 809-819.
- [Axelrad et al., 1996] Axelrad, P., Comp, C.J., and MacDoran, P.F., "SNR-Based Multipath Error Correction for GPS Differential Phase," *IEEE Transactions on Aerospace and Electronic Systems*, Vol. 32, No. 2, 1996, pp. 650-660.
- [Barth et al., 1994] Barth, C.A., Solomon, S.C., Rusch, D.W., and Woods, T.N., "Student Nitric Oxide Explorer", Investigation and Technical Plan - Proposal to the Universities Space Research Association Student Explorer Demonstration Initiative, from the Laboratory for Atmospheric and Space Physics, Internal Document, University of Colorado, 1994.
- [Behre and Axelrad, 1997] Behre, C.P. and Axelrad, P., "Coarse Single-Axis Attitude Estimation Using GPS Signal-to-Noise Ratio," Proceedings of KIS'97 Conference, Banff, University of Calgary, Dept. of Geomatics Engineering, June 2-6, 1997, pp. 417-427.
- [Brock et al., 1995] Brock, J. K., Fuller, R., Kemper, B., Mleczo, D., Rodden, J., and Tadros, A., "GPS Attitude Determination and Navigation Flight Experiment," Proceedings of ION GPS-95, Palm Springs, CA, Inst. of Navigation, Alexandria, VA, September 1995, pp. 545-554.

- [Cannon, *et al.*, 1994] Cannon, M.E., Sun, H., Owen, T.E., and Meindl, M.A., "Assessment of a Non-dedicated GPS Receiver System for Precise airborne Attitude Determination," Proceedings of ION GPS-94, Salt Lake City, UT, Inst. of Navigation, Alexandria, VA, September 1994, pp. 645-654.
- [Carpenter and Hain, 1997] Carpenter, J.R. and Hain, R.M., "Precise Evaluation of Orbital GPS Attitude Determination on the STS-77 GPS Attitude and Navigation Experiment (GANE)," Proceedings of the ION National Technical Meeting, Santa Monica, January 1997, pp. 387-398.
- [CATSAT Home Page] The CATSAT Satellite Project Home Page, University of New Hampshire, <http://www.catsat.sr.unh.edu/>.
- [Chatterjee and Hadi, 1988] Chatterjee, S. and Hadi, A. S., *Sensitivity Analysis in Linear Regression*, Wiley, 1988.
- [Cohen, 1996] Cohen, C.E., "Attitude Determination," in *Global Positioning System: Theory and Applications Vol. II*, edited by Parkinson *et al.*, Vol. 164, Progress in Astronautics and Aeronautics, AIAA, New York, 1996, pp. 519-538.
- [Cohen, 1992] Cohen, C. E., *Attitude Determination Using GPS*, Ph.D. Dissertation, Department of Aeronautics and Astronautics, Stanford University, Dec. 1992.
- [Comp, 1996] Comp, C.J., *GPS Carrier Phase Multipath Characterization and a Mitigation Technique Using the Signal-to-Noise Ratio*, Ph.D. Dissertation, Department of Aerospace Engineering Sciences, University of Colorado, July 1996.
- [Czopek and Shollenberger, 1993] Czopek, F. and Shollenberger, S., "Description and Performance of the GPS Block I and II L-Band Antenna and Link Budget, Proceedings of ION GPS-93, Salt Lake City, UT, Inst. of Navigation, Alexandria, VA, 1993, pp. 37-43.
- [Devore, 1990] Devore, J. L., *Probability and Statistics for Engineering and the Sciences*, Brooks/Cole, 1990.
- [Dunn, 1997] Dunn, C., Jet Propulsion Laboratory, personal communication, August, 1997.
- [Flawn, 1996] Flawn, B.J., "Compass," United States Patent No. 5572217, 1996.

- [Fraleigh and Beauregard, 1990] Fraleigh, J.B., and Beauregard, R.A., *Linear Algebra*, Addison-Wesley Publishing Company, 1990.
- [GANE Home Page] GANE Home Page, Goddard Space Flight Center, <http://sspp.gsfc.nasa.gov/>.
- [Ghaem *et al.*, 1992] Ghaem, S., Lauro, G.L., and Harnes, M., "Electronic Direction Finder," United States Patent No. 5146231, 1992.
- [Golub and Van Loan, 1989] Golub, G.H., and Van Loan, C.F., *Matrix Computations*, Johns Hopkins University Press, 1989, pp. 70-73.
- [GPS/Met Home Page] GPS/MET Home Page, University Corporation for Atmospheric Research, <http://pocc.gpsmet.ucar.edu/>.
- [Hashida and Unwin, 1993] Hashida, Y. and Unwin, M. J., "Satellite Attitude From a Single GPS Antenna," Proceedings of ION GPS-93, Salt Lake City, UT, Inst. of Navigation, Alexandria, VA, 1993, pp. 355-363.
- [Hoaglin, *et al.*, 1983] Hoaglin, D. C., Mosteller, F., and Tukey, J. W., *Understanding Robust and Exploratory Data Analysis*, Wiley, 1983.
- [Hoffman-Wellenhof, *et al.*, 1992] Hofmann-Wellenhof, B., Lichtenegger, H., and Collins, J., *GPS Theory and Practice*, Springer-Verlag Wien, 1992.
- [JSC Digital Image Collection Home] JSC Digital Image Collection Home, Johnson Space Center, <http://images.jsc.nasa.gov/>.
- [Kay, 1988] Kay, S. M., *Modern Spectral Estimation Theory & Application*, Prentice Hall, 1988.
- [Ketchum and Tolson, 1995] Ketchum, E. A., and Tolson, R., "Onboard Star Identification Without A Priori Attitude Information," *The Journal of Guidance, Control, and Dynamics*, Vol. 18, No. 2, Mar.-Apr. 1995, pp. 242-246.
- [Krebs, 1997] Krebs, M., Orbital Sciences Corp., personal communication, August, 1997.
- [Lightsey *et al.*, 1994] Lightsey, E.G., Cohen, C.E., Fees, W.A., and Parkinson, B.W., "Analysis for Spacecraft Attitude Measurements Using Onboard GPS," AAS Guidance and Control Conference, Keystone, CO, Feb. 1994, pp. 521-532.

- [Lightsey *et al.*, 1996] Lightsey, E.G., Ketchum, E., Flatley, T.W., Crassidis, J.L., Fresland, D., Reiss, K., and Young, D., "Flight Test Results of GPS Based Attitude Control on the REXII Spacecraft," Proceedings of ION GPS-96, Kansas City, MO, Inst. of Navigation, Alexandria, VA, 1996.
- [Lu, *et al.*, 1993] Lu, Gang, Cannon, M.E., Lachapelle, G., and Kielland, P., "Attitude Determination in a Survey Launch Using Multi-Antenna GPS Technologies," Proceedings of ION National Technical Meeting, San Francisco, CA, Inst. of Navigation, Alexandria, VA, 1993, pp. 251-260.
- [Martin-Niera and Lucas, 1992] Martin-Niera, M. and Lucas, R., "GPS Attitude Determination of Spin Stabilized Satellites," Proceedings of ION GPS-92, Albuquerque, New Mexico, Inst. of Navigation, Alexandria, VA, 1992, pp. 757-765.
- [Markley, 1993] Markley, F.L., "Attitude Determination Using Vector Observations: A Fast Optimal Matrix Algorithm", The Journal of the Astronautical Sciences, Vol. 41, No. 2, 1993, pp. 261-280.
- [Maybeck, 1994] Maybeck, P.S., *Stochastic Models, Estimation, and Control, Vol. 1*, Navtech Book and Software Store, 1994.
- [NovAtel, 1993] *GPSCard OEM Performance Series 2100 Series User Manual*, NovAtel Communications Limited, 1993.
- [Press, *et al.*, 1992] Press, W.H., Teukolsky, S. A., Vetterling, W.T., and Flannery, B.P., *Numerical Recipes in C*, Cambridge University Press, 1992.
- [Serrano, *et al.*, 1995] Serrano, J. B., Potti, J., Bernedo, P., and Pierluigi, S., "A New Spacecraft Attitude Determination Scheme based on the Use of GPS Line-Of-Sight Vectors," Proceedings of ION GPS-95, Palm Springs, CA, Inst. of Navigation, Alexandria, VA, 1995, pp. 1797-1806.
- [Shuster and Oh, 1981] Shuster, M.D., and Oh, S.D., "Three-Axis Attitude Determination from Vector Observations", The Journal of Guidance, Control, and Dynamics, Vol. 36, No. 3, 1981, pp. 70-77.
- [Shuster, 1983] Shuster, M.D., "Efficient Algorithms for Spin Axis Estimation", The Journal of the Astronautical Sciences, Vol. 31, No. 2, 1983, pp. 237-254.

- [Shuster, 1989] Shuster, M.D., "Maximum Likelihood Estimation of Spacecraft Attitude", *The Journal of the Astronautical Sciences*, Vol. 37, No. 1, 1989, pp. 79-88.
- [Shuster, 1994] Shuster, M.D., "Spacecraft Attitude Determination and Control," in *Fundamentals of Space Systems*, Pisacane, V.L. and Moore, R.C., ed., Oxford University Press, 1994.
- [Trimble, 1993] *TANS Vector Specification and User's Manual*, Trimble Navigation Limited, June 1993.
- [Wahba, 1965] Wahba, G., "A Least-Squares Estimate of Satellite Attitude," Problem 65-1, *SIAM Review*, Vol. 7, No. 3, 1965, p. 409.
- [Ward and Axelrad, 1995] Ward, L.M. and Axelrad, P., "Spacecraft Attitude Estimation Using GPS: Methodology and Results for RADCAL," *Proceedings of the ION National Technical Meeting*, Anaheim, CA, Inst. of Navigation, Alexandria, VA, 1995, pp. 813-825.
- [Ward, 1996] Ward, L.M., *Spacecraft Attitude Estimation Using GPS: Methodology and Results*, Ph.D. Dissertation, Department of Aerospace Engineering Sciences, University of Colorado, Aug. 1996.
- [Ward, P., 1996] Ward, P., "GPS Satellite Signal Characteristics," in *Understanding GPS Principles and Applications*, edited by Kaplan, E.D., Artech House, 1996, pp. 83-116.
- [Ware et al., 1996] Ware et al, 1996, GPS Sounding of the Atmosphere from Low Earth Orbit: Preliminary Results. *Bulletin of the American Meteorological Society*. Volume 77, pp. 19-40.
- [Wertz, 1978] Wertz, J. R., ed., *Spacecraft Attitude Determination and Control*, D. Reidel Publishing Company Library in Astrophysics and Space Science, 1978.
- [Wertz and Larson, 1991] Wertz, J. R., and Larson, W. J., eds., *Space Mission Analysis and Design*, Kluwer Academic Publishers, 1991.
- [Zumberge and Bertiger, 1996] Zumberge, J.F., and Bertiger, W.I., "Ephemeris and Clock Navigation Message Accuracy," in *Global Positioning System: Theory and Applications Vol. I*, B. W. Parkinson and J.J. Spilker, Jr., Eds., Vol. 163, *Progress in Astronautics and Aeronautics*, AIAA, New York, 1996, pp. 585-599.



# REPORT DOCUMENTATION PAGE

Form Approved  
OMB No. 0704-0188

Public reporting burden for this collection of information is estimated to average 1 hour per response, including the time for reviewing instructions, searching existing data sources, gathering and maintaining the data needed, and completing and reviewing the collection of information. Send comments regarding this burden estimate or any other aspect of this collection of information, including suggestions for reducing this burden, to Washington Headquarters Services, Directorate for Information Operations and Reports, 1215 Jefferson Davis Highway, Suite 1204, Arlington, VA 22202-4302, and to the Office of Management and Budget, Paperwork Reduction Project (0704-0188), Washington, DC 20503.

1. AGENCY USE ONLY (Leave Blank)	2. REPORT DATE 10 Dec 1997	3. REPORT TYPE AND DATES COVERED Final Report 1 Sep 1994 through 30 Jun 1997
----------------------------------	-------------------------------	---

4. TITLE AND SUBTITLE GPS Based Attitude Determination for Spinning Satellites	5. FUNDING NUMBERS AASERT GRANT NO: N00014-94-1-1158
6. AUTHORS Penina Axelrad Charles P. Behre	

7. PERFORMING ORGANIZATION NAME(S) AND ADDRESS(ES) University of Colorado, CB 431 Colorado Center for Astrodynamics Research Boulder, CO 80309	8. PERFORMING ORGANIZATION REPORT NUMBER PA-97-060
---	---

9. SPONSORING / MONITORING AGENCY NAME(S) AND ADDRESS(ES) Office of Naval Research, Code 251:EF Ballston Tower One 800 North Quincy Street Arlington, VA 22217-5660	10. SPONSORING / MONITORING AGENCY REPORT NUMBER
---	--

11. SUPPLEMENTARY NOTES

12a. DISTRIBUTION / AVAILABILITY STATEMENT	12b. DISTRIBUTION CODE
--	------------------------

13. ABSTRACT (Maximum 200 words)

This report describes the research performed by the Colorado Center for Astrodynamics Research (CCAR) under an AASERT Grant to study Global Positioning System (GPS) based attitude determination for spinning satellites. Two key contributions are discussed - phase-based methods for estimation of the spin axis of a spinning satellite, and signal-to-noise ratio (SNR) based methods for estimation of one or more spacecraft axes. The latter method, which is very robust and widely applicable, is demonstrated on actual flight data from three NASA missions. It provides instantaneous pointing knowledge at the 3-10 degree level with a single GPS antenna and is useful for attitude initialization, verification, GPS phase ambiguity resolution, and a reliable backup attitude determination sensor.

14. SUBJECT TERMS GPS, Signal-to-Noise Ratio, Attitude Determination, Satellite	15. NUMBER OF PAGES 148
	16. PRICE CODE

17. SECURITY CLASSIFICATION OF REPORT UNCLASSIFIED	18. SECURITY CLASSIFICATION OF THIS PAGE UNCLASSIFIED	19. SECURITY CLASSIFICATION OF ABSTRACT UNCLASSIFIED	20. LIMITATION OF ABSTRACT UL
---	--	---	----------------------------------